98

CEA/SACLAY
DSM

SERVICE TECHNIQUE DE CRYOGÉNIE ET DE MAGNÉTISME

FERMILAB
MAR 23 1999
LIBRARY

DAPNIA-STCM-99-01

Fermilab Library
0 1160 0062348 2

DAPNIA/STCM 99-01 February 1999

REVIEW OF SELECTED COIL AND COLLARED-COIL ASSEMBLY DATA FROM 10-M-LONG, 50-MM-TWIN-APERTURE LHC DIPOLE MAGNET PROTOTYPES

Arnaud Devred

DAPNIA

Département d'Astrophysique, de Physique des Particules, de Physique Nucléaire et de l'Instrumentation Associée
CEA/Saclay F-91191 Gif-sur-Yvette Cédex

Couverture : Sylvie Cabrit et Marc Sauvage

REVIEW OF SELECTED COIL AND COLLARED-COIL ASSEMBLY DATA FROM 10-M-LONG, 50-MM-TWIN-APERTURE LHC DIPOLE MAGNET PROTOTYPES

Arnaud Devred

Commissariat à l'Energie Atomique/Saclay
DSM/DAPNIA/STCM
F–91191 Gif-sur-Yvette Cedex, France

and

LHC/MMS
CERN, Laboratoire Européen
pour la Physique des Particules
CH–1211 Genève 23, Suisse

ABSTRACT

In 1991, the Laboratoire Européen pour la Physique des Particules (CERN) has launched the fabrication in industry of seven 10-m-long, 50-mm-twin-aperture dipole magnet prototypes for the Large Hadron Collider (LHC). The design and specific features of these magnets have been described elsewhere [1]. In this paper, we review some of the coil and collared-coil assembly data and we analyze the influence of tooling imperfections on magnet assembly.

CONTENTS

1	**DESIGN AND FABRICATION OVERVIEW**	**1**
2	**NOTATIONS**	**2**
3	**REVIEW OF COIL SIZE DATA**	**3**
3.1	INTRODUCTION	3
3.2	COIL STRESS-STRAIN CURVE	4
3.3	COIL SIZE MEASUREMENTS ON LHC PROTOTYPES	5
3.4	REVIEW OF AZIMUTHAL SIZE DATA	5
3.4.1	Ansaldo Prototypes	5
3.4.2	Noell Prototypes	6
3.5	REVIEW OF YOUNG'S MODULUS DATA	7
3.6	CONCLUSION	8
4	**REVIEW OF COLLARING DATA**	**9**
4.1	INTRODUCTION	9
4.1.1	Prestress Requirements	9
4.1.2	Collaring Procedure	10
4.1.3	Estimating Azimuthal Pre-Compression	10
4.1.4	Adjusting Azimuthal Pre-Compression	11
4.2	REVIEW OF COLLARING SHIMS	11
4.3	ESTIMATING PEAK STRESSES FOR ONE-STEP COLLARING	13
4.3.1	Basic Formula	13
4.3.2	Shim Thicknesses and Coil Size Data	13
4.3.3	Collar Cavity Reduction	14
4.3.4	Spring Rate Data	15
4.3.5	Average Peak Stress Data	16
4.3.6	Peak Stress Data As a Function of Axial Position	17
4.4	ESTIMATING COIL RESIDUAL STRESSES AFTER COLLARING	18
4.4.1	Basic Formula	18
4.4.2	Residual Pre-Compression Data	18
4.5	ESTIMATING COLLAR SPRING-BACK	20
4.6	RESIDUAL AZIMUTHAL PRE-COMPRESSIONS AS A FUNCTION OF AXIAL POSITION	21
4.7	CONCLUSION	21

5 REVIEW OF COLLAR DEFLECTION DATA 22
5.1 INTRODUCTION 22
5.2 ESTIMATING COLLAR DEFLECTIONS DUE TO ELASTIC ELONGATIONS OF COLLAR ARMS 23
5.3 REVIEW OF DEFLECTION DATA FROM ANSALDO PROTOTYPES 23
5.3.1 Data Presentation and First Cross-Magnet Comparison 23
5.3.2 Elastic Elongations Versus Elastico-Plastic Deformations 24
5.3.3 Comparison of Average Values 25
5.3.4 Origin of Elastico-Plastic Deformations 26
5.3.5 Influence of Collared-Coil Assembly Deformations on Main Dipole Field 26
5.3.6 Influence of a Thermal Cycle to 77 K 27
5.4 REVIEW OF DEFLECTION DATA FROM NOELL PROTOTYPES 27
5.5 REVIEW OF DEFLECTION DATA FROM ALSTOM/JEUMONT PROTOTYPE 29
5.6 REVIEW OF DEFLECTION DATA FROM ELIN/HOLEC PROTOTYPE 31
5.6 CONCLUSION 32
6 BRIEF SUMMARY 32
ACKNOWLEDGMENTS 34
REFERENCES 35
TABLES 37
FIGURES 59

1 DESIGN AND FABRICATION OVERVIEW

The seven 10-m-long, 50-mm-twin-aperture LHC dipole magnet prototypes discussed in this paper were designed to produce a field of the order of 10 T at 15000 A. Three of these prototypes were built in Italy, in collaboration with the Instituto Nazionale di Fisica Nucleare (INFN), by Ansaldo Energia S.p.A., two were built in Germany by Noell GmbH, one was built in France by a consortium made up of Jeumont Industrie and GEC Alsthom, and the last one was built by a consortium made up of Elin in Austria and Holec in the Netherlands.

The coil assemblies of the seven prototypes have an inner diameter of 50 mm and rely on the same geometry. They consist of two symmetrical half coil assemblies referred to as *poles*. The poles themselves are made up of two saddle shape coils, referred to as *inner* and *outer* coils. The coils of a given pole are wound from different cables and are joined by an internal splice.

Inner and outer coils are wound from flat, two-layer, slightly keystoned Rutherford-type cables. The inner coil cable has 26 strands, with a nominal strand diameter of 1.286 mm. Its nominal radial width is 17 mm and its nominal mid-thickness is 2.26 mm. The outer coil cable has 40 strands, with a nominal strand diameter of 0.838 mm. Its nominal radial width is also 17 mm but its nominal mid-thickness is 1.475 mm. For both cable types, the insulation consists of two layers of polyimide films completed by a fiber tape impregnated with B-stage epoxy. The innermost polyimide layer is 25-μm thick and is wrapped helically with a 50% overlap. The second polyimide layer is 12.5-μm thick and is wrapped with a 50% overlap. The nominal thickness of the impregnated fiber tape is 120 μm and the resin content is of the order of 20% in weight. The tape is wrapped helically on top of the polyimide layers with a 2-mm gap. It is made from glass fibers, except for the cables wound in the inner coils of the Elin/Holec prototype, where it is made of Kevlar fibers in the longitudinal direction and glass fibers in the transverse direction [1].

The coil assemblies are mechanically constrained, both radially and axially. The radial support is provided by means of laminated collars which are designed also to pre-compress the coils azimuthally. The axial support is provided by means of thick end-plates. The collared-coil assembly is surrounded by a yoke made of laminated low-carbon steel. The cold mass is completed by an austenitic steel outer shell, also called the *shrinking cylinder*, which is welded around the yoke. The outer shell and the end-plates delimit the containment vessel for the 2 K, 100 kPa superfluid helium bath. The cold mass has an overall length of the order of 10 m.

The Ansaldo and Noell prototypes use similar aluminum alloy collars, which are common to both coil assemblies and which are surrounded by a two-piece, vertically-split yoke. The Ansaldo prototypes include also aluminum spacers which are designed to control the closure of the yoke midplane gap. The Alsthom/Jeumont prototype uses separate, aluminum alloy collars with a two-piece, vertically-split yoke. The Elin/Holec prototype uses separate, stainless steel collars with a three-piece, vertically split yoke. Figures 1(a) through 1(d) present cross-sectional views of the various cold mass designs, while Table 1 summarizes salient features of the prototypes

In the case of the Ansaldo and Noell prototypes, two laminated, low carbon steel inserts are added at the top and bottom of the collars' central part to improve the yoke symmetry around each aperture. The yoke inner radius is 100.5 mm and the distance between the two beam axes is 180 mm. In the case of the Alsthom/Jeumont prototype, the yoke halves are slid around the two collared-coil assemblies which are separated by a non-magnetic stainless-steel spacer. The yoke inner radius is 111.0 mm and the inter-beam distance is 219 mm. For the Elin/Holec prototype, the spacing between the collared-coil assemblies is given by the central part of the three-piece yoke. The yoke inner radius is 93.0 mm and the inter-beam distance is 200 mm.

Within the Alsthom/Jeumont consortium, Jeumont Industrie had the responsibility of winding and curing the coils and of assembling the poles up to the internal splice between the two layers. The four poles were then delivered to GEC Alsthom for final coil assembly and all subsequent operations. A similar division of work was followed by the Elin/Holec consortium, with Elin taking the responsibility of pole fabrication and Holec doing the rest of the work.

2 NOTATIONS

The three Ansaldo prototypes are referred to as MTP1A1, MTP1A2 and MTP1A3. The two Noell prototypes are referred to as MTP1N1 and MTP1N2. The Alsthom/Jeumont prototype is referred to as MTP1AJ and the Elin/Holec prototype is referred to as MTP1EH.

The two apertures of a given prototype are identified by facing the magnet from the *connection end.* (The connection end is the magnet end where the current leads feed the coils). Aperture 1 is the aperture on the left-hand side, while Aperture 2 is the aperture on the right-hand side.

For a given aperture, a rectangular coordinate system (O,x,y,z) is defined by facing the magnet from the connection end so that O is at the aperture center, the x-axis is horizontal and points towards the right, the y-axis is vertical and points upwards, and the

z-axis is parallel to the magnet axis and is oriented from the *non-connection end* to the connection end. (The non-connection end is the magnet end opposite to the connection end).

Within a given aperture, and far from the magnet ends, the field can be considered as two-dimensional and is conveniently represented by a power series expansion

$$B_y(x,y) + iB_x(x,y) = B_1\, 10^{-4} \sum_{n=1}^{+\infty} (b_n + i\, a_n) \left(\frac{x+iy}{R_{ref}}\right)^{n-1} \qquad (1)$$

where B_x and B_y are the x- and y-components of the field, B_1 is the dipole field, b_n and a_n are the normal and skew $2n$-pole coefficients, and R_{ref} is the reference radius. (For LHC magnets of this generation, R_{ref} = 10 mm.)

The coil assemblies are connected electrically so that the dipole field is positive in Aperture 1 and negative in Aperture 2.

3 REVIEW OF COIL SIZE DATA

3.1 INTRODUCTION

The first operations of magnet assembly are coil winding and curing [2]. The objective of curing is three-fold: (1) to polymerize the epoxy of the cable insulation in order to make the coil rigid and easier to assemble, (2) to form the coil into the correct shape and the correct dimensions, and (3) to make the coil as uniform as possible along its length. Correctness of coil dimensions is important for field quality. Uniformity of the coil is also required to achieve uniform pre-compression after collaring.

The first set of mechanical measurements taken during magnet assembly are measurements of the azimuthal sizes of the cured coils. Once curing is completed, the coil is separated from its winding mandrel and is placed on a stable fixture which mocks up a half collar cavity (see Fig. 2). A pressure is then applied to the coil faces, which, in the coil assembly, define the parting planes, and the coil sizes are measured by means of dial indicators. Prior to the measurements, the zeros of the dial indicators are reset using a steel block, called the *master*, which is machined to the nominal coil dimension under the desired azimuthal pre-compression. There are of course two masters, one for the inner coils and one for the outer coils, which are representative of the design azimuthal sizes. Hence, the measured coil sizes correspond to deviations with respect to the masters.

The coil sizes are usually measured at various axial positions along the coil length and at various pressure levels for loading and unloading cycles. In the case of the seven 10-m-long, 50-mm-twin-aperture LHC dipole magnet prototypes, they were used to control the azimuthal dimensions and to determine the thicknesses of the collaring shims (see section 4). They can also be used to interpret some of the field quality data. For instance, in the case of the 15-m-long, 50-mm-single-aperture dipole magnet prototypes for the Superconducting Super Collider (SSC), clear correlations were found between azimuthal coil size mismatches and skew quadrupole and skew sextupole components [3].

3.2 COIL STRESS-STRAIN CURVE

The coils of accelerator magnets constitute a highly composite medium and their stress-strain curves are known to present a large hysteresis between the loading branch and the unloading branch [2,4]. The amplitude of the hysteresis depends on the maximum pressure reached during the loading cycle. The loading branch is usually more or less linear while the unloading branch can be approximated by a second order polynomial.

As an illustration, Fig. 3 shows examples of stress-strain curves measured on one side of an inner coil assembly package manufactured by Jeumont Industrie (the coil assembly package includes the coil assembly and the ground insulation). The various curves correspond to measurements at various positions along the coil length for loading-unloading cycles up to 100 MPa.

From the plot, the effective spring rate of the coil assembly package can be estimated to be of the order of 3710 MN/(m*m) for the loading branch while it appears to be stiffer for the unloading branch. The effective unloading spring rate can be estimated to be of the order of 7050 MN/(m*m) at 80 MPa. It decreases to 5150 MN/(m*m) at 65 MPa and to 4435 MN/(m*m) at 50 MPa.

This illustration shows that the effective spring rate can vary by a factor of 2 between loading and unloading, as well as when moving down along the unloading branch. Hence, to fully characterize the coil mechanical properties, as is necessary to compute collaring stresses (see section 4), it is very crucial to perform measurements for complete loading-unloading cycles. Furthermore, the stress-strain curve corresponding to the first loading-unloading cycle on a virgin coil is usually somewhat different from that of subsequent cycles, but, after a few cycles, the curves become more or less reproducible. Finally, it should be noted that the hysteresis observed at 4.2 K is smaller than the one observed at room temperature [4].

3.3 COIL SIZE MEASUREMENTS ON LHC PROTOTYPES

Systematic azimuthal size measurements were performed on all the coils manufactured for the seven 10-m-long, 50-mm-twin-aperture LHC dipole magnet prototypes. The measurement procedures were somewhat different at the different manufacturers. The measurement equipment used at Ansaldo and Noell allows one to apply a pressure on both sides of the coil at the same time (see Fig. 2), but there is no control of the alignment of the hydraulic cylinders and the applied pressure can be asymmetrical. The effects of this asymmetry can be eliminated by taking averages over the two coil sides. The equipment used at Jeumont Industrie allows one distinguish the two coil sides. The coil size data from Elin have been discussed elsewhere [5].

It should be noted that to perform in-depth analyses of the influence of azimuthal coil sizes on field quality, it is preferable to be able to distinguish between the two coil sides. For instance, it has been shown that systematic left/right asymmetries in the azimuthal sizes of the two coil sides could lead to rotations of the coil assembly midplane resulting in a systematic skew sextupole component [3].

In the following, we discuss azimuthal size data from selected Ansaldo and Noell prototypes and we review Young's modulus data for all seven prototypes.

3.4 REVIEW OF AZIMUTHAL SIZE DATA

3.4.1 ANSALDO PROTOTYPES

Figure 4(a) presents a summary plot of the azimuthal sizes measured on the 8 inner coils used in Ansaldo prototypes MTP1A2 and MTP1A3. As explained above, the data reported here are deviations with respect to a master having the nominal coil dimension under the desired azimuthal pre-compression. They correspond to a pressure of 80 MPa while unloading. They are presented as a function of axial position along the coil length and, for each axial position, are averaged over the two coil sides. The 8 coils were wound from cables coming from the same manufacturer (Europa Metalli S.p.A.). They were fabricated using the same contact tooling and the same curing press.

The plot of Fig. 4(a) presents three characteristic features: (1) all the curves are offset with respect to the x-axis, (2) all the curves present large variations as a function of axial position and (3) the variation profiles are very similar for all the coils. In particular, there appears to be two peaks: one near position 3 and one near position 6.

The existence of an offset simply means that the coils are oversized. The oversizing can have three origins: (1) the fact that the cable is thicker than expected, (2) the fact that the conductor insulation is thicker than expected or (3) the fact that the curing mold cavity may not have been dimensioned properly. The existence of large and reproducible variations along the coil length is a strong indicator of tooling imperfections.

Figure 4(b) presents a similar plot for the outer coils used in MTP1A2 and MTP1A3. The measured coil size deviations correspond here to a pressure of 55 MPa while unloading. The curves present the same characteristics as the ones in Fig. 4(a). Furthermore, the variation profiles appear to be nearly identical to those observed on the inner coils, with pronounced peaks near positions 3 and 6.

The fact that the variations observed along the length of the outer coils are similar to the variations observed along the length of the inner coils is a further indication of tooling imperfections. It also shows that the main source of imperfections is a piece of tooling that is common to the manufacturing of both inner and outer coils. This excludes contact tooling, such as winding mandrels, curing molds, and sizing bars which are specific to a type of coil, but points towards the curing press which was used for all the coils.

It turns out that the frame of the Ansaldo press, shown in Fig. 5, is made of several beams pieced together. It is likely that this multi-part assembly does not have a uniform stiffness and that there are weaker areas with larger deflections upon loading. These deflections then result in deformations of the curing mold which lead to azimuthal coil size variations.

3.4.2 NOELL PROTOTYPES

Figure 6(a) presents a summary plot of the azimuthal size deviations measured as a function of axial position along the inner coils used in Noell prototype MTP1N1, while Fig. 6(b) presents a similar plot for the inner coils used in Noell prototype MTP1N2. As for the Ansaldo prototypes, the sizes were measured at a pressure of 80 MPa while unloading (note that only the unloading branches of the stress-strain curves were recorded). For each axial position, the measurements are averaged over the two coil sides. The inner coils of magnet MTP1N1 were wound from cables manufactured by GEC Alsthom, whereas those of magnet MTP1N2 were wound from cables manufactured by New England Electric Wire with Otokumpu strands.

In comparison to Fig. 4(a), the curves are more or less centered about the x-axis and there appears to be much less variations as a function of axial position. (Note that the plots of Figs. 4(a), 4(b), 6(a) and 6(b) use the same y-range.) Comparing now the

curves in Figs. 6(a) and 6(b), it appears that, although the observed variations are more limited than for the Ansaldo coils, the profiles still appear to be fairly reproducible from coil to coil, independently of cable manufacturer.

Figures 7(a) and 7(b) present the azimuthal size deviations measured at 50 MPa while unloading on the outer coils of magnets MTP1N1 and MTP1N2. The outer coils of magnet MTP1N1 were wound from cables manufactured by Vacuumschmelze GmbH whereas those of magnet MTP1N2 were wound from cables manufactured by GEC Alsthom.

This time, the curves present a negative offset with respect to the x-axis (which means that the coils are slightly undersized). The amplitude of the variations as a function of axial position is of the same order as the one observed for the inner coils, and, once again, there appears to be a characteristic profile. This profile, however is somewhat different from the inner coil profile.

This brief analysis shows that the curing press used at Noell is of a better design than the one used at Ansaldo and that it yields more uniform coils. It can be argued also that, since the Noell data are more or less cleared from the effects of imperfections in the press itself, it is now possible to see the effects of imperfections in the tooling directly in contact with the coils. Hence, one explanation for the differences observed in the inner and outer coil profiles could be the fact that these two sets of coils were cured in two different molds.

3.5 REVIEW OF YOUNG'S MODULUS DATA

Table 2 presents a summary of the Young's moduli estimated from the azimuthal size measurements performed on the various coils used in the seven prototypes. The values correspond to an average over the straight sections of the four inner and four outer coils used in each magnet. They were estimated from the slopes of the unloading branches of the stress-strain curves at a pressure of 80 MPa for the inner coils and 55 MPa for the outer coils (except for the outer coils of the Noell and Elin/Holec prototypes where it is 50 MPa).

The Young's moduli of the inner coils of the Ansaldo and Noell prototypes are all around 30 GPa, whereas those of the inner coils of magnet MTP1EH are slightly above (35 GPa) and those of the inner coils of magnet MTP1AJ are significantly lower (20 GPa). The stiffer Young's modulus obtained for the inner coils of MTP1EH may be due to the mixed Kevlar/glass fiber tape used as outer wrap in the cable insulation. The cavity dimensions of the molds used to cure the coils of MTP1AJ were deliberately adjusted to achieve a lower Young's modulus.

The Young's moduli of the outer coils of the Ansaldo prototypes appear to be around 25 GPa, whereas those of the outer coils of the Noell prototypes are slightly lower (around 20 GPa). These lower values may be due to the fact that, for the Noell coils, the Young's modulus is estimated at 50 MPa while, for the Ansaldo coils, it is estimated at 55 MPa. The same is true for the outer coils of MTP1EH, although it may not entirely explain the measured value of 15 GPa. In the case of MTP1AJ, and as for the inner coils, the curing of the outer coils was carried out with a deliberate intention to achieve a low Young's modulus (although 10 GPa may be somewhat lower than originally intended).

The rationale behind using stiff coils is as follows. The stiffer the coil, the smaller the displacement upon given loading conditions. Hence, during magnet excitation, stiff coils are less likely to be deformed under the azimuthal components of the Lorentz forces, thereby limiting the risks of conductor motions and reducing the potentials for field quality distortions. However, there are at least two disadvantages associated with large Young's moduli. First, and as explained in section 4, stiffer coils require larger collaring forces and loose more pre-compression as a result spring-back or relaxation upon release of the collaring force. Second, when using a high modulus coil, small variations in the dimensions of the collar cavities can result in large variations in the coil azimuthal pre-compression. Hence, a stiff coil has less ability than a softer one to adapt itself to manufacturing tolerances. These two considerations concur to indicate that lower Young's modulus coils, such as the ones used for the inner layers of magnet MTP1AJ, are easier to assemble.

3.6 CONCLUSION

The curing operation is instrumental in forming the coil into the correct shape and the correct dimensions and in making the coil as uniform as possible along its length. The correct dimensions to be achieved are that determined by electromagnetic computations. One of the aims of curing is therefore to produce coils, which assume the desired size under the target azimuthal pre-compression. The size of a cured coil depends on the dimensions of its components (cable and insulation thickness) but also on the dimension of the molding cavity. The latter is usually adjustable. At present, there is no good theoretical model that can be used to predict with some accuracy the size of a cured coil and it is necessary to proceed empirically. Simple experimental procedures, such as the one developed at CEA/Saclay for the HERA and LHC quadrupole magnet coils, can nevertheless be followed to determine the optimum dimension of the molding cavity [6].

Measuring coil sizes is a painstaking operation requiring a specific tooling and a great care. However, it provides meaningful informations at an early stage of magnet

assembly. The RHIC experience has shown that a careful monitoring of coil sizes can be used to detect trends during mass-production, which allows implementation of corrective actions before the evolutions become damageable [7]. To be the most useful, the size data should be taken for complete loading-unloading cycles, on both sides of the coils and at small intervals (every 10 or 20 cm) along the coil length, particularly during the prototype phase.

Peak to peak variations of the order of two tenths of a millimeter, like the ones observed on the coils manufactured at Ansaldo, are not acceptable. The experience on SSC magnets at FNAL has shown that by carefully working on the tooling it was possible to achieve tolerances of +/- 2 mils (51 μm) over 15-m-long coils [8]. Similar tolerances were achieved on average coil sizes during the mass-production of RHIC dipole coils [7]. Note, however, that the RHIC coil production was small enough to rely on a single cable manufacturer and on similar batches of cable insulation. In the case of LHC, more than one cable manufacturer are needed and it is likely that there will be small thickness variations on the cable insulation. As a result, the aforementioned tolerances on coil sizes may still be achievable, but the Young's moduli of the coils will not be uniform over the entire production. This may lead to production batches having slightly different mechanical properties.

4 REVIEW OF COLLARING DATA

4.1 INTRODUCTION

4.1.1 PRESTRESS REQUIREMENTS

The next steps of magnet fabrication are coil assembly and collaring. The collars are designed to restrain the coils radially. They are also designed to pre-compress the coils azimuthally. The azimuthal pre-compression is needed to avoid parting of the coils from the collar poles under the effects of the azimuthal components of the Lorentz forces. The azimuthal components of the Lorentz force are directed from the poles to the midplane. They tend to compress both inner and outer coils and to unload the collar poles [2].

The room temperature pre-compression must compensate for at least three effects: (1) stress relaxation after collaring because of creep in the polyimide insulation and related effects (note that this relaxation is of different nature and has nothing to do with the relaxation of the collared-coil assembly upon release of the collaring press discussed in the next section), (2) pre-stress loss during cooldown due to possible thermal

shrinkage differentials between collars and coils, and (3) stress redistribution due to the azimuthal components of the Lorentz forces. The desired level of pre-compression is achieved by squeezing the coils into cavities which are smaller than their sizes at rest. The cavities are defined by the inner boundaries of the collars which are assembled and locked around the coils. For all LHC dipole magnet prototypes, but the Elin/Holec one, the collar interlocking is ensured by means of full-length tie rods located at, or right above and right below, the collared-coil assembly midplane. Magnet MTP1EH relies on short length keys inserted on both sides of the collared-coil assembly. The goal for these magnets was to achieve a pre-compression of 80 MPa in the inner coils and 50 MPa in the outer coils. Note that the yield point of Kapton® (used for the conductor and ground plane insulation) is 69 MPa at room temperature and 3% elongation [9] and that plastic deformations in the polyimide wraps and foils are unavoidable.

4.1.2 COLLARING PROCEDURE

The collaring operation starts by mounting the laminated collars around the coil assembly. To facilitate this operation, the collars are grouped into pairs (magnet MTP1A1) or packs (all other magnets). Then, the loosely collared coil assembly is placed onto a press bed and vertical forces are applied on flats purposely cutout on top and bottom of the collar laminations. The vertical forces are transmitted to the coils which are loaded azimuthally. They are increased until proper clearances are obtained to insert the tie rods or the keys into their dedicated housing holes or keyways. Once the tie rods or the keys are inserted, the forces are released and the locked collars start reacting against the loaded coils. The structure is then left to relax and to find its own mechanical equilibrium. This equilibrium depends on the respective stiffness of the collars and the coils, and since the collars are not infinitely rigid, the achieved residual stresses in the coils may be significantly lower than the maximum loads applied by the press. Several techniques can be used to limit coil overpressure during collaring [2,10].

4.1.3 ESTIMATING AZIMUTHAL PRE-COMPRESSION

According to the above description, the loading conditions experienced by the coils during collaring can be divided into two phases: (1) a loading phase, corresponding to the application of vertical forces by the press and (2) an unloading phase, corresponding to the vertical deformation of the collared-coil assembly under the forces exerted by the coils against the collar poles upon press release (this phenomenon is sometimes referred to as collared-coil assembly *relaxation*). The level of azimuthal pre-

compression depends on the parameters of these two phases. The maximum load provided by the press during the collaring operation can be estimated from the minimum arc length to which the coils are compressed along the loading branches of their stress-strain curves. The amount of stress relaxation within the collared-coil assembly is determined by the effective spring rate of the collars along the vertical diameter and by the effective unloading spring rate of the coil assembly package. Hence, and as mentioned in section 3, accurate computations of collaring stresses require a detailed knowledge of the coil stress-strain curves.

4.1.4 ADJUSTING AZIMUTHAL PRE-COMPRESSION

We have seen in section 3 that the azimuthal sizes measured on most of the coils used in the 10-m-long, 50-mm-twin-aperture LHC dipole magnet prototypes were out of tolerance. In order to correct for these discrepancies, the coil assembly of these magnets include two sets of shims of adjustable thicknesses: (1) *pole shims*, mounted at the collar poles and (2) *midplane shims*, placed at the coil assembly midplane [1]. The shim thicknesses were determined on the basis of the measured azimuthal coil sizes so as to ensure suitable level of pre-compressions on average over the magnets' straight sections. It should be noted, however, that the pole shims displace the coil pole faces and that the midplane shims displace the coil assembly midplane, and that such displacements can result in undesirable field distortions. Hence, the use of shims is only conceivable in the course of a magnet R&D program and should be avoided during magnet production.

4.2 REVIEW OF COLLARING SHIMS

Tables 3(a) through 3(g) present summaries of the average azimuthal coil size deviations, of the average Young's moduli (or the average effective spring rates), and of the thicknesses of the pole and midplane shims implemented in the straight sections of the seven 10-m-long, 50-mm-twin-aperture LHC dipole magnet prototypes. For all prototypes, except the Alsthom/Jeumont one, the coil size deviations are referenced with respect to a nominal arc length which include the coil midplane insulation. Since the coil sizes were measured before the midplane insulation was put on, the quoted deviations present a positive offset equal to the thickness of this insulation. In the case of the Alsthom/Jeumont prototype, the azimuthal size measurements were performed on the insulated half-coil assemblies and there is no such offset.

In addition, Tables 3(a) through 3(g) give the nominal values of the pole shim thicknesses. These nominal values were determined by evaluating the differences between: (1) the average distances between the collar pole faces and the coil pole faces, assuming that the collars are undeflected and that the coils have the right geometries and occupy their design positions, and (2) the overall thicknesses of the different layers of insulation and of the various components (other than the pole shims) which are placed on top to cover or encapsulate the coil pole faces. The inner layer data used for these computations are summarized in Table 4(a) while the outer layer data are summarized in Table 4(b). In practice, however, and as explained in section 4.1.2, the collaring operation is accompanied by a relaxation of the collared-coil assembly, which produces collar deflections and results in elongations of the arc lengths of the collar cavities. These elongations must, of course, be taken into account when computing the shim thicknesses required to achieve the target pre-compressions.

In the case of the Ansaldo prototypes, there are no midplane shims. The pole shims are left/right symmetrical but are usually different for the upper and lower halves. In most cases, the largely oversized coils are compensated by reducing in proportion the pole shim thicknesses.

In the case of the Noell prototypes, the data given for the inner-layer pole shims include the 500-μm-thick pole sliding sheets. The lumped thicknesses of the pole shims assume nominal values, except for the inner layer of the upper half coil assembly in Aperture 2 of magnet MTP1N1, where it is 975 μm instead of 1000 μm. In addition, midplane shims were implemented in all outer layers. The midplane shims are always left/right symmetrical but, in most cases, are different for the upper and lower halves.

In the case of magnet MTP1AJ, there are no midplane shims. The pole shims are the same in all four quadrants of Aperture 1. They are left/right asymmetrical in Aperture 2, but are identical in diametrically opposite quadrants. This was done to compensate for the left/right asymmetries in the azimuthal sizes of the coil assembly packages in order to achieve a more uniform pre-compression distribution.

Finally, in the case of magnet MTP1EH, the inner coils count three types of shims: (1) midplane Kapton® shims and (2) pole Kapton® shims, glued by Elin directly on the coils, and (3) regular, impregnated glass fiber pole shims implemented by Holec. The outer layers do not have midplane shims, but the pole shims are also divided into two: (1) Kapton® shims, glued by Elin, and (2) impregnated glass fiber shims implemented by Holec. The Kapton® shims are the same in all quadrants of both apertures. The impregnated glass fiber shims are left/right symmetrical but are different for the upper and lower halves.

4.3 ESTIMATING PEAK STRESSES FOR ONE-STEP COLLARING

4.3.1 BASIC FORMULA

In order to estimate the coil pre-compressions, one first needs to compute the maximum load transmitted to the coils during a one-step collaring [11]. This is done by assuming that the coil packages are surrounded by an infinitely stiff medium and are compressed to the desired arc lengths minus a certain quantity designated as ($2\Delta l_{\mathrm{collar}}$). The quantity ($2\Delta l_{\mathrm{collar}}$) corresponds to the reduction in collar cavity that must be produced in order to obtain the proper clearances needed for tie rods or keys insertion. In practice, and as explained elsewhere, the collaring operation is performed in several steps and take advantage of the fact that the collar arms can be elastically elongated [10]. This concurs to reduce the forces needed to carry out the collaring operation as well as the peak stresses seen by the coils.

The maximum load, σ_t, transmitted to a given coil layer during a one-step collaring can be estimated from

$$2\,\sigma_t\, w_{\mathrm{coil}} \approx k_{\mathrm{pack,up}}\Big[s_m^{\mathrm{top}} + s_{\mathrm{offset}}^{\mathrm{top}} + s_m^{\mathrm{bot}} + s_{\mathrm{offset}}^{\mathrm{bot}} + (s_{\mathrm{pole}}^{\mathrm{top}} + s_{\mathrm{pole}}^{\mathrm{bot}} - 2s_{\mathrm{pole}}^{\mathrm{n}}) + s_{\mathrm{mid}}^{\mathrm{top}} + s_{\mathrm{mid}}^{\mathrm{bot}} + 2t_{\mathrm{mid}} + 2\Delta l_{\mathrm{collar}}\Big] \qquad (2)$$

where w_{coil} is the coil radial width, $k_{\mathrm{pack,up}}$ is the effective spring of one side of the inner or outer coil assembly package, $s_{\mathrm{pole}}^{\mathrm{top}}$ and $s_{\mathrm{pole}}^{\mathrm{bot}}$ are the thicknesses at rest of the upper and lower pole shims, $s_{\mathrm{pole}}^{\mathrm{n}}$ is the nominal pole shim thickness at rest, $s_{\mathrm{mid}}^{\mathrm{top}}$ and $s_{\mathrm{mid}}^{\mathrm{bot}}$ are the thicknesses at rest of the upper and lower midplane shims, t_{mid} is the thickness at rest of the midplane insulation, s_m^{top} and s_m^{bot} are the measured azimuthal size deviations under given conditions, and $s_{\mathrm{offset}}^{\mathrm{top}}$ and $s_{\mathrm{offset}}^{\mathrm{bot}}$ are correction factors taking into account the conditions under which the azimuthal sizes were measured.

4.3.2 SHIM THICKNESSES AND COIL SIZE DATA

Table 5(a) presents a summary of the size data needed for collaring stress computations.

In the case of magnet MTP1AJ, the azimuthal size measurements were performed directly on a coil assembly package that included both ground and midplane insulations, and the data were taken for both loading and unloading. The correction factors, $s_{\mathrm{offset}}^{\mathrm{top}}$ and $s_{\mathrm{offset}}^{\mathrm{bot}}$, can be estimated using Eq. (3) of Ref. [11]. The size values quoted in

Table 5(a) correspond to measurements at a pressure, $\sigma_{m,up}$ [see Table 5(c)], during the loading phase, and are averaged over the coil straight sections.

In the case of the Ansaldo, Noell and Elin/Holec prototypes, the azimuthal size measurements did not include the ground and midplane insulation and data were only taken for unloading. Then, it is necessary to reconstruct the loading data, and the correction factors are estimated using Eq. (8) of Ref. [11]. The size values quoted in Table 5(a) correspond to measurements at a pressure, $\sigma_{m,dwn}$, while unloading, after a loading cycle up to a maximum pressure, $\sigma_{m,p}$, where $\sigma_{m,p}$ and $\sigma_{m,dwn}$ are given in Table 5(c). As for magnet MTP1AJ, they are averaged over the coil straight sections.

Note that in the case of the inner layers of magnet MTP1EH, the 300-μm-thick pole sliding sheets are lumped into the overall thickness at rest of the pole caps, t_{pole}.

4.3.3 COLLAR CAVITY REDUCTION

An important parameter in Eq. (2) is the value of Δl_{collar}. For the Ansaldo, Noell and Alsthom/Jeumont prototypes, this value is determined by the tie rod diameters and by the shape and locations of the tie rod housing holes in the top and bottom collars. From drawing dimensions, the nominal value of Δl_{collar} is

$$\Delta l_{collar} = 50 \ \mu m \quad . \tag{3}$$

In the case of the Ansaldo prototypes, there are three tie rods: one at the center of the collared-coil assembly, with a nominal diameter of 22 mm, and one on each side, with a nominal diameter of 14 mm. However, the collaring press used at Ansaldo delivered a maximum force of 9 MN/m and was not powerful enough to allow insertion of the nominal diameter rods [1]. Some progresses were nevertheless realized as the program went along. For magnet MTP1A1, the central rod diameter is 21.90 mm and the side rods' diameter is 13.95 mm. The vertical clearance needed to insert the rods was therefore reduced by an average value of 75 μm on the diameter, which translated into a reduction of 37.5 μm on the value of Δl_{collar}. For this magnet, Δl_{collar} is taken equal to 12.5 μm. For magnet MTP1A2, the central rod diameter is 21.95 mm and the side rods' diameter is 13.95 mm. This corresponds to an average reduction of 50 μm on the required vertical clearance and Δl_{collar} is taken equal to 25 μm. For magnet MTP1A3, the central rod diameter is 22 mm, the side rods' diameter is 13.95 mm, and Δl_{collar} is taken equal to 37.5 μm for the outer coils. In addition, for the inner coils of magnet MTP1A3, 40–to-50 μm thick Kapton® reinforcements were added at the midplane. These

reinforcements resulted in a further reduction of the collar cavity estimated to be 40 μm, and the value of Δl_{collar} is taken equal to 77.5 μm.

In the case of Noell, the press could deliver a maximum force of 14 MN/m which was large enough to allow insertion of nominal diameter rods. Note, however, that the tie rods of magnet MTP1N1 were hammered into place, while those of magnet MTP1N2 were plunged, beforehand, into liquid nitrogen. The value of Δl_{collar} is taken to be the nominal value of 50 μm for the outer coils, but is taken to be 90 μm for the inner coils, which, similarly to the inner coils of magnet MTP1A3, include 40–to-50 μm thick Kapton® midplane reinforcements.

The collared-coil assemblies of magnet MTP1AJ include four tie rods (two on each side of each collared-coil assembly: one right above and one right below the collared-coil assembly midplane). The four rods have a nominal diameter of 16 mm. The assemblies were collared with the nominal diameter rods and Δl_{collar} is taken equal to 50 μm.

In the case of magnet MTP1EH, the collared-coil assemblies are locked by means of four keys (two on each side, with one right above and one right below the collared-coil assembly midplane). To facilitate insertion, keys and keyways are slightly tapered with a taper angle of 2.5°. When presenting the keys in front of the keyways, the tapered sides of the keys are parallel to the tapered sides of the keyways, and when the keys are inserted at their nominal positions, there remains a vertical clearance of 0.22 mm. However, the top keyway midplane is at located at a distance of 15.10 mm with respect to the collared-coil assembly midplane whereas the bottom keyway midplane is at 14.90 mm. Thus, when alternating top and bottom collars, the vertical clearance between key and keyway is reduced to 20 μm, but, thanks to the taper, it is still possible to fully insert the keys. It follows that, to perform a nominal one-step collaring, there is no need to push further onto the top and bottom collars and Δl_{collar} is taken equal to 0.

4.3.4 SPRING RATE DATA

Table 5(b) presents a summary of the spring rate data needed for the present computations. The effective spring rates are estimated by taking into account that a coil assembly package is constituted of several springs mounted in series, including the pole and midplane shims, the ground and midplane insulation and the coil itself, as given by Eq. (15) of Ref. [11].

In the case of magnet MTP1AJ, the values quoted for the coils, $k_{coil,up}$ and $k_{coil,dwn}$, correspond to actual measurements and already include ground and midplane

insulations. Hence, the only springs to be added in series to determine $k_{pack,up}$ and $k_{pack,dwn}$ are those corresponding to the shims.

For the Ansaldo, Noell and Elin/Holec prototypes, the values of $k_{coil,dwn}$ are estimated from the measured Young's moduli while unloading, E_m, using

$$k_{coil,dwn} = \frac{E_m \, w_{coil}}{l^n_{coil}} \quad , \tag{4}$$

where, l^n_{coil} is the nominal arc length of the coil, estimated at the average coil radius (l^n_{coil} = 43.284 mm for the inner coils and l^n_{coil} = 43.406 mm for the outer coils). The values of $k_{coil,up}$ are reconstructed using

$$k_{coil,up} \approx \eta \, k_{coil,dwn} \quad , \tag{5}$$

where η is taken equal to 17/24 (which corresponds to the average between 2/3 and 3/4). Furthermore, for these prototypes, $k_{coil,up}$ and $k_{coil,dwn}$ only include the coils and all the springs mentioned above should be added in series to determine $k_{pack,up}$ and $k_{pack,dwn}$.

Whenever needed, the Young's modulus of the pole shims, E_{pole}, is taken equal to that of impregnated glass fibers (25 GPa), whereas the Young's moduli of the midplane shims and of the ground and midplane insulations, E_{mid} and E_i, are taken equal to that of Kapton® (3 GPa). The unloading spring rate values quoted in Table 5(b) are estimated at the pressure, $\sigma_{m,dwn}$, where $\sigma_{m,dwn}$ is given in Table 5(c).

4.3.5 AVERAGE PEAK STRESS DATA

Using Eq. (2) and the data in Tables 5(a) and 5(b), it is now possible to compute the average one-step collaring peak stresses, σ_t, over the straight sections of the various coils used in the 10-m-long, 50-mm-twin-aperture LHC dipole magnet prototypes. The computation results are presented in Table 5(c).

The average inner coil peak stresses of MTP1A2, MTP1A3, MTP1N1 and MTP1N2 appear to be in excess of 150 MPa, while those of MTP1A1 and MTP1AJ are in the range 125–135 MPa, and those of MTP1EH are of the order of 115 MPa. The average outer coil peak stresses appear to be in excess of 100 MPa, except for magnet MTP1AJ, where they are between 90 and 100 MPa, and for magnet MTP1EH, where they are between 70 and 80 MPa. Let us remind that, in practice, the collaring operation is performed in several steps so that the actual pressures seen by the coils are lower than these upper limits.

The data of Table 5(c) show that, for the Ansaldo prototypes, the computed peak stresses are more or less in progression from magnet to magnet. This progression is consistent with the increase in tie rods diameters. It appears also that, in spite of the larger azimuthal sizes measured on the coils of magnet MTP1AJ, the computed peak stresses for this prototype are lower than for the Ansaldo and Noell prototypes. This is due to the fact that the larger coil sizes are more or less compensated by the lower effective spring rates of the coil assembly packages. Finally, the magnet with the lower peak stresses is clearly magnet MTP1EH, where Δl_{collar} was assumed to be nil. This, of course, is a direct benefit stemming from using tapered keys instead of tie rods.

It should be noted that, in the case of magnet MTP1EH, four additional, 60–μm-thick, polyimide adhesive tapes were glued on the outer radius of the outer coils (one per quadrant). These tapes were positioned at the azimuths of the outer coil copper wedges and extend over two neighboring conductors on each side. When computing the collaring shim thicknesses, the Elin/Holec staff considered that these tapes caused localized overthicknesses and increased the radial pressure exerted on the coil. The resulting effect on the coil azimuthal pre-compression was estimated to be equivalent to the addition of one 30-μm-thick shim per outer coil quadrant. It is unclear if this effect is real or not. For completeness, we have indicated between parentheses in Table 5(c) the average peak stress values computed with the assumption that each outer coil quadrant included one additional 30-μm-thick shim. The addition of these virtual shims appear to increase the outer coil peak stresses by about 10%.

4.3.6 Peak Stress Data As a Function of Axial Position

We have seen that the azimuthal sizes measured on the coils assembled in the Ansaldo prototypes exhibited large variations as a function of axial position. We can expect these non-uniformities to directly affect σ_t.

As an illustration, Fig. 8 presents a summary plot of the one-step collaring peak stresses computed as a function of axial position along the straight sections of the inner and outer coils of the two apertures of magnet MTP1A2. The peak stresses were derived using Eq. (2) and the relevant coil size data from Figs. 4(a) and 4(b). To simplify the computations, the effective loading spring rates of the coil assembly packages were assumed to be uniform, equal to the average values given in Table 5(b). The curves of Fig. 8 exhibit peak-to-peak variations of the order of 50 MPa.

4.4 ESTIMATING COIL RESIDUAL STRESSES AFTER COLLARING

4.4.1 BASIC FORMULA

Having computed the maximum loads, σ_t^{in} and σ_t^{out}, transmitted to the inner and outer coils during a one-step collaring, it is now possible to estimate the stress reductions, $\Delta\sigma_{s.b.}^{in}$ and $\Delta\sigma_{s.b.}^{out}$, resulting from the spring-back of the collared-coil assembly upon press release. The values of $\Delta\sigma_{s.b.}^{in}$ and $\Delta\sigma_{s.b.}^{out}$ are given by [11]

$$\Delta\sigma_{s.b.}^{in} = \frac{2\, a_{in}\, k_{pack,dwn}^{in}}{k_{collar}^{v} + 2\, a_{in}\, k_{pack,dwn}^{in} + 2\, a_{out}\, k_{pack,dwn}^{out}} \left(\sigma_t^{in} + \sigma_t^{out}\right) , \tag{6a}$$

and

$$\Delta\sigma_{s.b.}^{out} = \frac{2\, a_{out}\, k_{pack,dwn}^{out}}{k_{collar}^{v} + 2\, a_{in}\, k_{pack,dwn}^{in} + 2\, a_{out}\, k_{pack,dwn}^{out}} \left(\sigma_t^{in} + \sigma_t^{out}\right) , \tag{6b}$$

where k_{collar}^{v} is the effective spring rate of the collars along the vertical diameter, a_{in} and a_{out} are two coefficients related to collar geometry, and $k_{pack,dwn}^{in}$ and $k_{pack,dwn}^{out}$ are self-explanatory notations. The values of k_{collar}^{v}, a_{in} and a_{out} for the collars used in the 10-m-long, 50-mm-twin-aperture LHC dipole magnet prototypes can be found in Table 2 of Ref. [11].

The residual stresses after collaring, σ_r^{in} and σ_r^{out}, can then be deduced using

$$\sigma_r^{in} = \sigma_t^{in} - \Delta\sigma_{s.b.}^{in} , \tag{7a}$$

and

$$\sigma_r^{out} = \sigma_t^{out} - \Delta\sigma_{s.b.}^{out} . \tag{7b}$$

4.4.2 RESIDUAL PRE-COMPRESSION DATA

The values of σ_r^{in} and σ_r^{out} computed using Eqs. (7a) and (7b) and the effective unloading spring rates given in Table 5(b) are shown in the "σ_r" column of Table 5(c). (For magnet MTP1EH, the values between brackets are referring, once again, to a computation assuming the presence of additional 30-μm-thick-shims in the coil outer layer.) The values for the outer coils appear to be more or less at the pressure level at

which the coil spring rates were determined (55 MPa while unloading for all prototypes, except magnets MTP1N1, MTP1N2 and MTP1EH, where it is 50 MPa). However, in the case of the inner coils, and especially for the Ansaldo and Noell prototypes, the computed pre-compressions are always far below the level of 80 MPa used for the spring rate estimations. We have seen in section 3.2 that, for the unloading branch of the coil stress-strain curve, the Young's modulus, and therefore the spring rate, were strong functions of pressure level. Hence, the spring-back computations must be redone using values of effective spring rates corresponding to the achieved levels of residual pre-compressions.

In the case of the Ansalso, Noell and Elin/Holec prototypes, the Young's moduli were only measured at one pressure, and one can only guess what the value might be at a lower pressure. In Ref. [10], we estimated that the unloading Young's modulus in the vicinity of 50 MPa was about 70% of the unloading Young's modulus in the vicinity of 80 MPa. The column "σ_r^* " of Table 5(c) presents the residual pre-compressions re-computed with the assumption that, for the Ansaldo and Noell prototypes, the effective unloading inner coil spring rates were reduced by 30% with respect to the values given in Table 5(b). In the case of magnet MTP1AJ, the re-computation was carried out using the measured spring rates at 55 MPa, whereas in the case of magnet MTP1EH, it was done assuming that the effective unloading inner coil spring rates were reduced by 20%.

For most inner coils, but those of magnet MTP1EH, it appears that the re-computed pre-compressions are above the levels at which the coil spring rates were estimated. This means that the values of 50 or 55 MPa are too low and that the spring-back computations should be iterated one more time, using estimates of the coil spring rates at an intermediate pressure between σ_r and σ_r^* . In the following, we shall assume that the iteration converges for $[(\sigma_r + \sigma_r^*)/2]$ and that that this pressure corresponds to the actual level of residual pre-compression. In the case of the inner coils of magnet MTP1EH, the σ_r^* values seem to make sense and we shall consider them as correct. For this last magnet, it remains to determine if the effects of the 30-μm-thick-shims are real or not. In the absence of a clear answer, we shall take the average of the values computed with and without virtual shims.

Table 6 presents a summary of the estimated residual pre-compressions after collaring completion over the straight sections of the various prototypes discussed in this paper. It appears that, for the inner coils, the values are all below the 80 MPa target. It appears also, that, for the Ansaldo magnets, the values increase progressively from magnet to magnet. As for the peak stresses, this is consistent with the increase in tie rod diameters. Finally, it appears that, for magnets MTP1AJ and MTP1EH, and in spite of the fact that the peak stresses for a one-step collaring given in Table 5(c) were somewhat

lower than for the other magnets, the residual azimuthal pre-compressions are among the largest ones. As detailed in the next section, this can be explained in terms of collar spring-back.

4.5 ESTIMATING COLLAR SPRING-BACK

As described above, when the forces exerted by the collaring press are removed, the collared-coil assembly is left to relax and to find its own mechanical equilibrium. If the collars were infinitely rigid, all the load transmitted by the press to the coils would be preserved. However, since the collars are not infinitely rigid, part of this load is lost in spring-back or relaxation and the residual stresses in the coils can be significantly lower. This spring-back or relaxation of the collared-coil assembly is shared between the collars and the coils on the basis of their respective stiffnesses. The share of the spring-back taken by the collars, q, can be estimated as [10]

$$q \approx \frac{k^{\mathrm{v}}_{\mathrm{collar}}}{k^{\mathrm{v}}_{\mathrm{collar}} + 2\, a_{\mathrm{in}}\, k^{\mathrm{in}}_{\mathrm{pack,dwn}} + 2\, a_{\mathrm{out}}\, k^{\mathrm{out}}_{\mathrm{pack,dwn}}} \quad . \tag{8}$$

Equation (8) shows that, for a given value of $k^{\mathrm{v}}_{\mathrm{collar}}$, the lower the effective spring rates of the inner and outer coil assembly packages, the larger the spring-back ratio. Conversely, for given values of $k^{\mathrm{in}}_{\mathrm{pack,dwn}}$ and $k^{\mathrm{out}}_{\mathrm{pack,dwn}}$, the larger the effective collar spring rate along the vertical diameter, the larger also the q-value. It follows that, the softer the coils and the stiffer the collars, the larger the share of the spring-back taken by the collars, and thereby, the lower the stress reduction in the coils.

Let us first discuss the case of the aluminum-collar magnets. The collars used in the Ansaldo and Noell prototypes, on one side, and the ones used in the Alsthom/Jeumont prototype, on the other side, have similar effective spring rates along the vertical diameter (see Table 2 of Ref. [11]). However, and as we have already mentioned, the effective spring rates of the coil assembly packages of magnet MTP1AJ are somewhat lower. As a result, the collar spring back ratios of the Ansaldo and Noell prototypes are in the range 30 to 40% while that of magnet MTP1AJ is in excess of 50%.

One consequence of the higher q-value of magnet MTP1AJ is that the azimuthal coil stress reductions due to spring-back or relaxation are lower than in other magnets. This explains the relatively high values of residual pre-compressions observed in Table 6 in spite of the lower peak stresses computed in Table 5(c). The fact that pre-compression levels similar to that obtained for magnets MTP1A3 and MTP1N2 can be achieved with considerably smaller peak stresses is one of the of advantages of using softer coils.

Let us now consider the case of magnet MTP1EH. The effective spring rate along the vertical diameter of the stainless steel collars used in this magnet is about 2 times the spring rates of the aluminum collars used in the other magnets. As a result, and in spite of the fact that the effective spring rates of the coil assembly packages of magnet MTP1EH are similar to those of the Ansaldo and Noell prototypes, the computed spring back ratio is of the order of 55% and is comparable to that of magnet MTP1AJ. As for magnet MTP1AJ, the larger spring-back ratio results in lower coil stress reductions, and the residual inner coil pre-compressions of magnet MTP1EH turn out to be the largest ones, while the computed peak stresses were the smallest ones.

For the sake of the argument, let us now place the soft coil assembly packages of magnet MTP1AJ into the stiff collars of magnet MTP1EH. The collar spring-back ratio would then be of the order of 70%. Such high value would of course be very favorable when trying to minimize the risks of collaring overpressure.

4.6 RESIDUAL AZIMUTHAL PRE-COMPRESSIONS AS A FUNCTION OF AXIAL POSITION

To conclude this review of collaring data, Fig. 9 presents a summary plot of the estimated residual pre-compressions in the inner and outer coils of the two apertures of magnet MTP1A2 as a function of axial position. As could be expected from the measured azimuthal coil sizes and from the computed peak stresses, there appears to be very large variations along the magnet length and the variation profiles are similar to the ones observed in Figs. 4(a), 4(b), and (8) (note, for instance, the pronounced peaks near positions 3 and 6). These pre-compression variations are a direct consequence of the coil size variations. Furthermore, since the coil size variations are more or less the same from coil to coil, the defects get combined when the upper and lower half coils are assembled together, which further degrade the pre-compression profiles. Peak-to-peak variations of 30 MPa are of course not desirable in a magnet assembly.

Figure 10 presents a similar plot of the estimated residual compressions for Aperture 1 of magnet MTP1AJ. Note that the *y*-scale is the same as in Fig. 9. Here, the pre-compressions appear much more uniform and the peak-to-peak variations do not exceed 10 MPa.

4.7 CONCLUSION

As we have seen, the objective of collaring is to provide a suitable level of azimuthal pre-compression to the coil assembly. Furthermore, the collaring must be

carried out so as to limit the maximum pressure applied to the coil assembly during the operation and the residual pre-compression profile must be as uniform as possible along the coil assembly length. The peak pressure can be limited by performing the collaring operation in several steps and by optimizing the load distribution for each of the steps. In addition, it is preferable to use collars with a large effective spring rate along the vertical diameter compared to the effective spring rates of the inner and outer coil assembly packages. The uniformity of the pre-compression profile is mainly determined by the uniformity of the azimuthal coil sizes. Discrepancies in the azimuthal coil sizes may be corrected by the use of shims, but the shims can degrade field quality and they complicate the assembly process.

5 REVIEW OF COLLAR DEFLECTION DATA

5.1 INTRODUCTION

As explained in section 4, in the final phase of collaring, the collared-coil assembly is left to relax and to find its own mechanical equilibrium. In this system, the pre-compressed coils exert forces against the top and bottom collars which are locked together by means of keys or tie rods. The forces are mainly directed against the collar poles. They are counteracted by the keys or the tie rods and put the collar arms into tension. As the collar arms are not infinitely stiff, they elongate elastically. Furthermore, the high stresses in the vicinity of the keyways or tie rod housing holes also produce elastic deformations, which, if the yield stress of the collar material is locally exceeded, can enter the plastic range. The elastic elongations and the elastico-plastic deformations get combined and result in deflections along various axes of the collared-coil assembly.

The deformations of the collared-coil assemblies are usually measured upon collaring completion at regular intervals along the collared-coil assembly and are compared to nominal, undeflected values. In the case of the 10-m-long, 50-mm-twin-aperture LHC dipole magnet prototypes, the measurements were taken manually by means of micrometers between well identified and easily accessible reference surfaces. The measured quantities varied from manufacturer to manufacturer, depending on collar design. It should be noted that the measurement reproducibility can be enhanced by using a semi-automatic machine such as the one shown in Fig. 11, which was developed at Fermi National Accelerator Laboratory (FNAL) for the LHC Interaction Region quadrupole magnets [12].

5.2 ESTIMATING COLLAR DEFLECTIONS DUE TO ELASTIC ELONGATIONS OF COLLAR ARMS

We have seen that part of the deflections of the collared-coil assembly is due to the elastic elongations of the collar arms under forces exerted by the pre-compressed coils. An estimate of the resulting increase in the vertical diameter of the collared-coil assembly, ΔD_{v}, is given by Eq. (28) of Ref. [11]

$$\Delta D_{\mathrm{v}} = \frac{\Delta y\left(R^{\mathrm{o}}_{\mathrm{collar}}\right)}{\Delta y\left(R^{\mathrm{n.a.}}_{\mathrm{collar}}\right)} \frac{4\,(\sigma^{\mathrm{in}}_{\mathrm{t}} + \sigma^{\mathrm{out}}_{\mathrm{t}})\, w_{\mathrm{coil}}}{k^{\mathrm{v}}_{\mathrm{collar}} + 2\, a_{\mathrm{in}}\, k^{\mathrm{in}}_{\mathrm{pack,dwn}} + 2\, a_{\mathrm{out}}\, k^{\mathrm{out}}_{\mathrm{pack,dwn}}} \tag{9}$$

where the values of the ratio $\left[\Delta y\left(R^{\mathrm{o}}_{\mathrm{collar}}\right)/\Delta y\left(R^{\mathrm{n.a.}}_{\mathrm{collar}}\right)\right]$ can be found in Table 2 of Ref. [11].

5.3 REVIEW OF DEFLECTION DATA FROM ANSALDO PROTOTYPES

5.3.1 DATA PRESENTATION AND FIRST CROSS-MAGNET COMPARISON

Figure 12 shows the reference surfaces used for collar deflection measurements along the lengths of the LHC/Ansaldo and LHC/Noell prototypes. For the Ansaldo magnets, the most relevant data are those corresponding to the dimensions (B_1B_1') and (B_2B_2'), which are taken parallely to the pole axes between flats located on top and bottom and on each side of the collared-coil assembly. The nominal, undeflected values of (B_1B_1') and (B_2B_2') are 176 mm.

Figure 13 presents a summary plot of measured (B_1B_1') and (B_2B_2') as a function of axial position for magnet MTP1A1, while Figs. 14(a) and 14(b) present similar plots for magnet MTP1A2. Note that the three plots use the same x–scale and the same y-range, but that the origin of the ordinates is shifted by –50 μm between Fig. 13, on one hand, and Figs. 14(a) and 14(b), on the other hand.

Let us first compare Fig. 13 and Fig. 14(a). As for the measured azimuthal coil sizes, the measured deflections of the collared-coil assemblies appear to exhibit large variations as a function of axial position, with a succession of three pronounced peaks (one around 3100 mm, one around 4500 mm and one around 6200 mm). The variation profiles are nearly identical on both sides of each collared-coil assembly and, with the

applied shift of −50 μm, the profiles of magnet MTP1A2 can be superimposed to the profiles of magnet MTP1A1. The fact that data from different magnets show the same characteristic features is once again a strong indication of systematic imperfections in either the assembly procedure or the tooling (or both).

5.3.2 ELASTIC ELONGATIONS VERSUS ELASTICO-PLASTIC DEFORMATIONS

We have seen in section 4.6 that the non-uniformities in the azimuthal sizes of the coils used in the Ansaldo prototypes resulted in large variations as a function of axial position of the estimated residual pre-compressions after collaring. One can expect these pre-compression variations to directly affect the elastic elongations of the collar arms.

Figure 15 presents a summary plot of the elastic elongations computed as a function of axial position along the two pole axes of the collared-coil assembly of magnet MTP1A2. The elastic elongations are derived using Eq. (9) and the peak stress data shown in Fig. (8). To simplify the computations, the effective unloading spring rates of the inner coil assembly packages, $k^{in}_{pack,dwn}$, are assumed to be uniform, equal to 85% of the average values given in Table 5(c). (The 0.85 correction factor was introduced to take into account the fact that the coil Young's moduli were measured at higher pressures than the ones finally achieved in the collared-coil assemblies). Furthermore, a constant offset is added to the computed elongations to take into account the fact that the tie rods implemented in this collared-coil assembly are not of nominal diameters. This offset is estimated to be +50 μm for magnet MTP1A2

The computed elongation profiles shown in Fig. 15 do bear some resemblance with the measured deflection profiles of Fig. 14 (a), but they are not really similar. In particular, one can relate the computed peaks near positions 3 and 6 to the collar deflection peaks near positions 3100 mm and 6200 mm, but there is no evidence in the computed profiles of the middle peak observed in the measured profiles near position 4500 mm. One can argue, however, that the peaks are relatively narrow and that the coil size measurements were taken at relatively large intervals. Hence, it might be that the middle peak was missed in the profiles of Fig. 15 because of a lack of coil size data between positions 4 and 5.

Let us now compare the amplitudes of the variations. The measured profiles of Fig. 14(a) show peak-to-peak variations in excess of 0.3 mm, while the peak-to-peak variations of the computed profiles of Fig. 15 are less than 0.13 mm. Hence, there is a factor of at least 2 between the observed and computed peak-to-peak variations. This indicates that elastic elongations of the collar arms cannot account for all the observed

deflections and leads us to think that elastico-plastic deformations near the collar housing holes must also be playing an important role.

5.3.3 COMPARISON OF AVERAGE VALUES

A confirmation of the role played by elastico-plastic deformations can be obtained by comparing average values of computed elastic elongations with actual average values of measured deflections of the collared-coil assemblies. The computed elongations are derived by means of Eq. (9), using the average peak stress data of Table 5(c). As we did for the computed profiles of Fig. 15, the spring rates of the inner coil assembly packages are assumed to be 15% lower than the average values given in Table 5(b). Offsets are also added to the computed elongations to take into account the fact that the tie rods are not of nominal diameters. These offsets are estimated to be +75 μm for magnet MTP1A1, +50 μm for magnet MTP1A2 et +25 μm for magnet MTP1A3. The computation results are presented in the columns "Est." of Table 7 while the average vertical deflections measured on the collared-coil assemblies are reported in the columns "Meas.".

According to the computations, the vertical elongations of the collared-coil assembly of magnet MTP1A2 are expected to be somewhat larger than the vertical elongations of the collared-coil assembly of magnet MTP1A1. This may be surprising if one considers that the central rod used in magnet MTP1A2 is larger than the one used in magnet MTP1A1. However, and as shown in Table 6, the azimuthal pre-compressions achieved in magnet MTP1A2 are larger than the ones achieved in magnet MTP1A1. These larger pre-compressions result in larger elastic elongations of the collar arms which compensate the difference in central rod diameter.

In spite of the larger residual pre-compressions, Table 7 shows that the measured deflections on magnet MTP1A2 are quite a bit smaller than the ones measured on magnet MTP1A2, while the profiles of Fig. 14(a) are shifted by about –50 μm with respect to the profiles of Fig. 14(a). This profile shift is all the more intriguing, given that the measured dimensions (B_1B_1') and (B_2B_2') are not very far from the side rods, which are the same in both magnets.

A possible explanation for the unexpected trend observed between the measured deflections of the collared-coil assemblies of magnets MTP1A1 and MTP1A2 could be a reduction in the elastico-plastic deformations induced by the collaring operation in the vicinity of the tie rod housing holes. As we have seen, a number of difficulties were encountered during the collaring of these magnets and it was not possible to insert tie rods of nominal diameters. However, and as we already pointed out, the collaring procedure was gradually improved from magnet to magnet (allowing, in particular, the insertion of

larger diameter rods). It is conceivable that these improvements also led to reductions of the elastico-plastic deformations induced near the tie rod housing holes and of the ensuing vertical deflections of the collared-coil assembly. In the case of magnet MTP1A2, the deflection decrease due to the reduction in elastico-plastic deformations might have overcome the deflection increase due to the larger elastic elongations.

5.3.4 ORIGIN OF ELASTICO-PLASTIC DEFORMATIONS

The above discussions indicate that a significant fraction of the measured deflections on the collared-coil assemblies of the Ansaldo prototypes result from elastico-plastic deformations. We saw also that the induced elastico-plastic deformations are, in average, smaller for the second prototype, probably as a result of improvements in the collaring procedure. Nevertheless, it remains that the measured deflections exhibit large variations as a function of axial position which cannot be explained in terms of pre-compression variations and which are very similar for both collared-coil assemblies. The similarities between the two magnets and the fact that the observed variations are far in excess from what can be expected from azimuthal coil size variations seem to indicate that, atop of the average effects described above, the structures have been subjected to non-uniform loads which have permanently deformed them.

It turns out that the press used for the collaring of magnets MTP1A1 through MTP1A3 was the same as the press used for the curing of the coils assembled in these magnets. As explained in section 3.4.1, the frame of this press, shown in Fig. 5, is made up of several beams pieced together. The stiffness of this multi-part is likely to be non-uniform, resulting in non-uniform deflections upon loading. Furthermore, to perform the collaring operation, the press has to be pushed up to its limits, and the non-uniformities engendered during this operation are likely to be far greater than the ones engendered during the curing operation. These large non-uniformities then result in deformations of the collared-coil assemblies which are much more pronounced than the distortions previously imprinted to the coils. This, once again, shows how damageable tooling imperfections can be and how important it is to work out all the details of magnet assembly.

5.3.5 INFLUENCE OF COLLARED-COIL ASSEMBLY DEFORMATIONS ON MAIN DIPOLE FIELD

As we have seen, we believe that the variations in the vertical deflections measured along the lengths of the collared-coil assemblies of the Ansaldo prototypes are

due to permanent deformations imprinted by imperfections in the collaring press. These deformations, which are observed on the outside of the collared-coil assemblies, also translate into deformations of the collar inner cavities and of the coil geometry which, in turn, can degrade field quality.

As an illustration, Fig. 16 presents summary plots of measured dipole field as a function of axial position in the two apertures of the three Ansaldo prototypes. As for the coil sizes and the collared-coil assembly deflections, the measured dipole field appears to exhibit significant variations as a function of axial position and the variation profiles are very reproducible from aperture to aperture and from magnet to magnet. Furthermore, the variation profiles present three pronounced valleys along the magnets' straight sections which are reminiscent of the three pronounced peaks seen on the deflection plots. (Note, however, that the axial positions of the valleys cannot be directly compared to the axial positions of the peaks, because the magnetic measurement data correspond to average values over a certain length while the deflection data are very localized.) Hence, it seems likely that these dipole field variations are caused by the observed deformations of the collared-coil assemblies.

5.3.6 INFLUENCE OF A THERMAL CYCLE TO 77 K

To conclude this review of the Ansaldo collar deflections data, let us compare the data of Fig. 14(a) to those of Fig. 14(b). The data of Fig. 14(a) were taken right after collaring completion while those of Fig. 14(b) were taken after having thermally cycled the collared-coil assembly of magnet MTP1A2 to 77 K by cooling it to liquid nitrogen temperature. The measured deflections appear nearly identical and the thermal cycling does not seem to have had any significant effect.

5.4 REVIEW OF DEFLECTION DATA FROM NOELL PROTOTYPES

The reference surfaces used for collar deflection measurements on the LHC/Noell prototypes are the same as the ones used for the LHC/Ansaldo prototypes (see Fig. 12). For the Noell prototypes, the most relevant data are those corresponding to the dimensions (B_1B_1'), (B_2B_2'), (C_1C_1') and (C_2C_2') measured on both sides and in the central part of the collared-coil assembly. The nominal, undeflected values of (B_1B_1'), (B_2B_2'), (C_1C_1') and (C_2C_2') are 176 mm.

Figure 17(a) presents a summary plot of measured (B_1B_1'), (B_2B_2'), (C_1C_1') and (C_2C_2') as a function of axial position for magnet MTP1N1, while Fig. 17(b) presents a

similar plot for magnet MTP1N2. Note that the two plots use the same x- and y-scales and that the y-range is the same as for the plots of Figs. 13 and 14.

In comparison to the Ansaldo data it appears that: (1) the measured deflections vary as a function of axial position, but the amplitudes of the variations are much smaller and do not exceed 0.1 mm, (2) the measured deflections are left/right symmetrical, but are larger in the central part of the collared-coil assemblies than on the sides, and (3) the variation profiles exhibit trends which are common to the central parts and the sides of each collared-coil assembly and which are common to both collared-coil assemblies. In particular, there appears to be a valley centered around position 2000 mm followed by a gradual increase up to position 4000 mm.

The similarities observed on the various profiles are once again indications of tooling imperfections, but the fact that the variation amplitudes are smaller than on magnets MTP1A1 and MTP1A2 tells us that the collaring press used at Noell is of a better design and is more rigid than the Ansaldo press. This conclusion is similar to the one we drew from analyzing the azimuthal sizes of the cured coils, which is not surprising, given that, as for the Ansaldo magnets, the curing and collaring operations of the Noell magnets were carried out with the same press.

The differences observed between the deflections measured in the central parts and on the sides of the collared-coil assemblies can be explained by considering that the central rod is subjected to a larger load than the side rods. This larger load is likely to produce larger stresses and larger elastico-plastic deformations in the vicinity of the rod housing hole, thereby resulting in larger deflections in the central part. It can be noted, however, that the difference, which is of the order of 0.1 mm for the first prototype, where the tie rods were hammered into place, is reduced to less than 50 μm for the second prototype, where the side rods were inserted after having been plunged into liquid nitrogen. The procedure followed for the second prototype seems therefore to be more adequate.

Finally, and as for the Ansaldo prototypes, Table 7 shows a comparison between the computed deflections due to elastic elongations of the collar arms and the measured deflections in average over the collared-coil assemblies' straight sections. The computations were carried out using Eq. (9), the peak stress data given in Table 5(c) and the spring rate data given in Table 5(b), corrected by a factor 0.85 for the inner coil assembly packages. The measured data correspond to average values of the dimensions (B_1B_1') and (B_2B_2') on the collared-coil assembly sides (as taken upon collaring completion). There appears to be a difference of the order of +50 μm between measured and computed values. This difference is comparable to what was observed on magnet

MTP1A2 and can be attributed to elastico-plastic deformations in the vicinity of the tie rod housing holes

5.5 REVIEW OF DEFLECTION DATA FROM ALSTOM/JEUMONT PROTOTYPE

Figure 18 shows the reference surfaces used for deflection measurements along the collared-coil assemblies of the Alsthom/Jeumont prototype. For our analyses, the most relevant data are those corresponding to the dimensions (C_3) and (C_4), which are taken parallely to the pole axes between flats located on top and bottom and on both sides of each collared-coil assembly. The nominal, undeflected values of (C_3) and (C_4) are 186 mm.

The two collared-coil assemblies of magnet MTP1AJ were collared twice due to electrical shorts detected at the end of the first collaring operation [13]. The second collaring operation was carried out using the same repaired coils, the same insulation thicknesses and the same shim thicknesses. Figure 19(a) presents a summary plot of measured (C_3) and (C_4) as a function of axial position after the first collaring, while Fig. 19(b) presents a similar summary plot after the second collaring. Note that both plots use the same *y*–range as the deflection plots of the Ansaldo and Noell prototypes.

The plots of Figs. 19(a) and 19(b) exhibit three main features: (1) the peak-to-peak variations after both collaring are of the order to 0.1 mm and are similar to the ones observed on the Noell magnets, (2) the variation profiles after both collaring are more or less the same for each side of the two collared-coil assemblies but are somewhat different from collared-coil assembly to collared-coil assembly, and (3) the deflections measured after the second collaring are smaller than the ones measured after the first collaring, but the average decrease is of the order 80 μm for Aperture 2 while it is only of the order of 30 μm for Aperture 1.

The fact that the peak-to-peak variations are rather limited and that there are no systematic trends of variations between the two collared-coil assemblies indicate that the collaring press used at GEC Alsthom was properly designed and provided an uniform load. A possible explanation for the larger decrease observed on the measured deflections of the Aperture-2 collared-coil assembly after the second collaring is provided in Ref. [13]. It turns out that the collared-coil assembly corresponding to Aperture 1 was disassembled right after completion of the first collaring operation, while the one corresponding to Aperture 2 was stored "as is" in the workshop for almost 4 months, and experienced temperatures varying from 27 to 35 °C during at least two of the months. These uncontrolled storage temperatures are likely to have accelerated creep in the coil

insulation, resulting in a decrease of azimuthal pre-compression and of the ensuing elastic elongations of the collar arms. Hence, according to this explanation, the additional 50–μm decrease observed on the measured deflections of Aperture 2 would be due to changes in the mechanical properties of the coils having taken place while the structure was still assembled consequently to the first collaring.

The reductions in inner and outer coil azimuthal pre-compressions, $\Delta\sigma_r^{in}$ and $\Delta\sigma_r^{out}$, corresponding to a reduction of the elastic elongation of the collared coil assembly along the vertical diameter, ΔD_e, of the order of 50 μm can be estimated as [10]

$$\Delta\sigma_r^{in} = \frac{\Delta y\left(R_{collar}^{n.a.}\right)}{\Delta y\left(R_{collar}^{o}\right)} \frac{a_{in}\, k_{pack,dwn}^{in}\, \Delta D_e}{2\, w_{coil}} \tag{10a}$$

and

$$\Delta\sigma_r^{out} = \frac{\Delta y\left(R_{collar}^{n.a.}\right)}{\Delta y\left(R_{collar}^{o}\right)} \frac{a_{out}\, k_{pack,dwn}^{out}\, \Delta D_e}{2\, w_{coil}} \tag{10b}$$

Using Eqs. (10a) and (10b) and the spring rate data of Table 5(b), we get: $\Delta\sigma_r^{in} \approx$ 7.5 MPa and $\Delta\sigma_r^{out} \approx$ 4.8 MPa, which corresponds to about 10% of the residual pre-compression values given in Table 6 for the Alstom/Jeumont prototype. Such numbers are consistent with what can be expected from the effects of creep in Kapton® insulation [9] and support the explanation given in Ref. [13] for the larger change observed on the measured deflections of Aperture 2 after the second collaring.

Finally, and as for the Ansaldo and Noell prototypes, we can compare the average values of the computed elastic elongations with the average values of the measured deflections of the collared-coil assemblies after the first collaring. The computed elongations are derived by means of Eq. (9), using the average peak stress data of Table 5(c) [and taking for the spring rates of the inner coil assembly packages, $k_{pack,dwn}^{in}$, 85% of the values given in Table 5(b)]. The measured values of Aperture 2 appear to be about 40 μm larger than the computed ones, while it is the opposite for Aperture 1. The difference between the measured and computed valued observed on Aperture 2 is similar to what was observed on magnet MTP1A2 and on the Noell prototypes and can be attributed to elastico-plastic deformations in the vicinity of the tie rod housing holes. There is no explanation for the fact that, on Aperture 1, the measured deflections turn out to be smaller than the computed elongations.

5.6 REVIEW OF DEFLECTION DATA FROM ELIN/HOLEC PROTOTYPE

Figure 20 shows the reference surfaces used for deflection measurements along the collared-coil assemblies of the Elin/Holec prototype. Similarly to the case of the Alsthom/Jeumont prototype, the most relevant data for this magnet are those corresponding to the dimensions (H_3) and (H_4), which are taken parallely to the pole axes between flats located on top and bottom and on both sides of each collared-coil assembly. The nominal, undeflected values of (H_3) and (H_4) are 175 mm.

Figure 21 presents a summary plot of measured (H_3) and (H_4) as a function of axial position for the two collared-coil assemblies of magnet MTP1EH. Note that the *y*–range is the same as for all the other deflection plots. Similarly to what was observed for the collared-coil assemblies of the Alsthom/Jeumont prototype, the peak-to-peak variations are of the order of 0.1 mm and the variation profiles on both sides of a given collared-coil assembly are more or less similar. Comparing the profiles for the two collared-coil assemblies, they all show a valley around position 4350 mm, which could indicate a weak spot in the frame of the collaring press. The upper beam of the collaring press used by Holec is made up of four sections of equal length and the position of this weak spot could correspond to the junction between the two middle sections.

As for the other prototypes, Table 7 shows a comparison between the computed deflections due to elastic elongations of the collar arms and the measured deflections in average over the collared-coil assemblies' straight sections [for these computations, the effective unloading spring rates of the inner coil assembly packages were assumed to be 80% of those given in Table 5(b)]. Once again, there appears to be a difference of the order of +50 μm between measured and computed values. This difference is similar to the one observed on aluminum collar magnets and can also be attributed to elastico-plastic deformations in the keys or in the vicinity of the keyways.

Let us now compare the average deflections measured on magnet MTP1EH with those measured on magnet MTP1AJ. The values for the stainless steel collar assemblies appear to be about 0.15 mm smaller than for the aluminum collar assembly, while, as shown in Table 6, the residual pre-compressions achieved on these two magnets were about the same. Of course, the lower deflections of magnet MTP1EH are a direct benefit stemming from the use of stiffer collars. It is worth mentioning that the level of deflections measured on this magnet and the level of residual pre-compressions given in Table 6 are consistent with deflection measurements performed on a collar pack assembly mock-up during the fabrication of a 1-m-long, 50-mm-twin aperture dipole magnet model

(referred to as MTA-CERN), which uses separate stainless steel collars of the same design [14].

5.7 CONCLUSION

Collar deflection measurements provide a useful way of checking the distortions produced by the collaring operation. The measured deflections have two main causes: (1) elastic elongations of the collar arms as a result of the forces exerted by the pre-compressed coils, and (2) elastico-plastic deformations in the vicinity of the keyways or the tie rod housing holes. The elastic elongations of the collar arms can be estimated from the known values of coil pre-compressions, and the differences between these estimations and the measured deflections give an idea of the amplitude of the elastico-plastic deformations. When the collaring operation is carried out properly, the elastico-plastic deformations appear to be of the order of +50 μm along the vertical diameter of the collared-coil assembly and are about the same for aluminum and stainless steel collar assemblies. However, non-uniformities in the collaring press or missteps in the collaring procedure can lead to large and non-uniform distortions of the collared-coil assembly, which, among other, degrade field quality.

6 BRIEF SUMMARY

We reviewed the azimuthal size measurements performed on the cured coils assembled in the seven 10-m-long, 50-mm-twin aperture LHC dipole magnet prototypes. We used the coil size data and the known thicknesses of the shims implemented in the various structures to determine the residual azimuthal pre-compressions in the coils upon collaring completion. Furthermore, we estimated the elastic elongations produced by the pre-compressed coils along the vertical diameters of the collared-coil assemblies and we compared these estimations with actual deflection measurements.

With the exception of the coils produced for the Ansaldo magnets, the size data appear to be fairly uniform as a function of axial position, with peak-to-peak variations of the order of 0.1 mm. The size data of the Ansaldo coils exhibit large and reproducible variations as a function of axial position which can be attributed to flaws in the design of the curing press (which also served as collaring press).

Most of the coils produced by the various manufacturers appear to be either undersized or oversized and required correction shims. In spite of this variability, the computed residual stresses after collaring are similar for 5 of the prototypes, with values between 55 to 65 MPa for the inner coils and between 45 and 55 MPa for the outer coils.

The two outliers are magnets MTP1A1 and MTP1A2 where difficulties were encountered during the collaring operation due to a limitation in the force delivered by the press (which was the same as the curing press).

For the magnets were the collaring procedure was carried out normally, the measured deflections of the collared-coil assemblies are consistent with what can be expected from elastic elongations produced by the coil pre-compressed coils. Note, however, but there appears to be an offset of the order of +50 μm along the vertical diameter which can be attributed to elastico-plastic deformations in the vicinity of the keyways or tie rod housing holes. The design flaws of the press used at Ansaldo were exacerbated when the press was pushed to the limit to perform the collaring operation and resulted in large and permanent deformations of the collared-coil assemblies. These deformations are fairly reproducible from collared-coil assembly to collared-coil assembly and are likely to be the cause of observed variations on the main dipole field. Finally, it is worth mentioning that exposure of a collared-coil assembly for long period of time in an uncontrolled environment may lead to significant creep in the Kapton® insulation.

The set of analyses presented in this paper shows that carefully taken mechanical data provide a solid base to reconstruct the history of stresses and deformations during magnet assembly and can be used to proof tooling. It also shows that rigidity and uniformity are two key considerations to be integrated in tooling design.

ACKNOWLEDGMENTS

This work was originally started in 1996 as part of an informal agreement between Jean Pierre Gourber, Head of CERN/LHC Division, and Jacques Haïssinski, then Head of CEA/DSM/DAPNIA. The author wishes to thank Carlo Wyss, Head of LHC/MMS, and Marcel Jacquemet, Head of DAPNIA/STCM, for letting him complete and document his analyses.

The author is very grateful to Daniel Leroy for helping him out with the Elin/Holec data and to Luca Bottura for providing him cold magnetic measurement data. The author also wishes to express his warm thanks to Giancarlo Spigo for many discussions and insightful comments.

REFERENCES

[1] A. Devred, "Features of 10-m-long, 50-mm-twin aperture LHC dipole magnet prototypes," LHC–MMS Internal Note 98–08, Geneva (1998) and Preprint DAPNIA/STCM 98–02, Gif-sur-Yvette (1998).

[2] A. Devred, T. Bush, *et al.*, "About the mechanics of SSC dipole magnet prototypes," AIP Conference Proceedings, Vol. 249(2), pp. 1310–1374 (1992).

[3] T. Ogitsu and A. Devred, "Influence of azimuthal coil size variations on magnetic field harmonics of superconducting particle accelerator magnets," *Rev. Sci. Instrum.*, Vol. 65 No. 6, pp. 1998–2005 (1994).

[4] A.I. Andreev, S.S. Kozub, V.V. Sytnik, A.T. Veshchikov and A.V. Zlobin, "Mechanical properties of the coil for the UNK SC magnets," IHEP Preprint 93–61, Protvino (1993).

[5] F. Zerobin, M. Painer, *et al.*, "Size and stiffness measurements on 9.5 m long LHC dipole magnet coils," *IEEE Trans. Magn.*, Vol. 30 No. 4, pp. 2328–2331 (1994).

[6] P. Védrine, J.M. Rifflet, *et al.*, "Mechanical tests on the prototype LHC lattice quadrupole," *IEEE Trans. Magn.*, Vol. 30 No. 4, pp. 2475–2478 (1994).

[7] M.D. Aneralla, D.H. Fisher, *et al.*, "Industrial production of RHIC magnets", *IEEE Trans. Magn.*, Vol. 32 No. 4, pp. 2059–2064 (1996).

[8] R.E. Sims, "Tooling and process parameter improvements leading to improved dimensional control of the cured SSC dipole coils," *Supercollider 3*, J. Nonte, ed., pp. 57–74 (1991).

[9] "Kapton® Polyimide Film: Summary of Properties," Technical Documentation published by Du Pont.

[10] A. Devred and G. Spigo, "Analysis of the collaring data from the first 50-mm-aperture, 10-m-long LHC/Noell dipole magnet prototype," LHC–MMS Internal Note 96–02, Geneva (1996).

[11] A. Devred and G. Spigo, "Formula glossary for collaring of LHC-type dipole magnets," LHC–MMS Internal Note 96–09 (1996).

[12] D.V. Mitchell, T. Heger, *et al.*, "Mechanical studies of the Fermilab low beta quadrupole collared coils," *IEEE Trans. Appl. Supercond.*, Vol. 7 No. 2, pp. 586–589 (1997).

[13] G. Spigo, "Facts, observation and measured data gathered during the construction of the Jeumont/GEC-Alsthom superconducting prototype dipole magnet," AT-MA Internal Note 95–115, Geneva (1995).

[14] G. Spigo, private communication (1992).

TABLE CAPTIONS

Table 1. Salient features of 10-m-long, 50-mm-twin-aperture, LHC dipole magnet prototypes.

Table 2. Summary of Young's moduli estimated from azimuthal size measurements performed on the coils used in 10-m-long, 50-mm-twin-aperture, LHC dipole magnet prototypes. The data are in GPa and correspond to averages over the straight sections of the four inner and four outer coils of each magnet. They are estimated from the slopes of the unloading branches of the strain-stress curves at the pressures specified in brackets.

Table 3. Summary of coil azimuthal sizes and of collaring shim thicknesses in the straight section of 10-m-long, 50-mm-twin-aperture LHC dipole magnet prototypes: (a) LHC/Ansaldo dipole magnet prototype MTP1A1, (b) LHC/Ansaldo dipole magnet prototype MTP1A2, (c) LHC/Ansaldo dipole magnet prototype MTP1A3, (d) LHC/Noell dipole magnet prototype MTP1N1, (e) LHC/Noell dipole magnet prototype MTP1N2, (f) LHC/Alsthom-Jeumont dipole magnet prototype MTP1AJ, and (g) LHC/Elin-Holec dipole magnet prototype MTP1EH.

Table 4. Estimating the nominal thicknesses of the pole shims for the 10-m-long, 50-mm-twin-aperture, LHC dipole magnet prototypes: (a) inner layers and (b) outer layers.

Table 5. Spread sheets used for the computations of collaring stresses: (a) size data (in μm), (b) spring rate data [in MN/(m*m)] and (c) stress data (in MPa).

Table 6. Estimated azimuthal pre-compressions after collaring completion on average over the straight sections of the coils of the 10-m-long, 50-mm-twin-aperture, LHC dipole magnet prototypes (in MPa).

Table 7. Comparison between estimated and measured vertical deflections on average over the the straight sections of the collared-coil assemblies of the 10-m-long, 50-mm-twin-aperture, LHC dipole magnet prototypes (in mm).

Table 1. Salient features of 10-m-long, 50-mm-twin-aperture, LHC dipole magnet prototypes.

	Ansaldo	Noell	Alsthom/Jeumont	Elin/Holec
Distance Between Axes	180 mm	180 mm	219 mm	200 mm
Cable Insulation	Kapton® + impregnated fiberglass	Kapton® + impregnated fiberglass	Kapton® + impregnated fiberglass	Kapton® + impregnated Kevlar®/glass (inner coils) Kapton® + impregnated fiberglass (outer coils)
Coil Cooling	canals on inner side of pole shims	canal at periphery of inner coil top wedge	canal at periphery of inner coil top wedge	
Coil End Spacers	machined from G11 tubes	machined from G11 tubes	machined from G11 tubes	casted bronze with Al_2O_3 coating
Collars	common, aluminium alloy, stacked into 169-mm-long packs, rod tied	common, aluminium alloy, stacked into 86-mm-long packs, rod tied	separate, aluminium alloy, riveted by pairs, rod tied	separate, stainless steel, stacked into 79.04-mm-long packs, with keys
Collar/Yoke Shims	n/a	n/a	n/a	0.45-mm CuSn6 shims at 45°
Yoke	two-piece, vertically split; stacked into 10-m-long assembly; with aluminium control gap spacers	two-piece, vertically split; stacked into 800-mm-long modules; clamped before shell welding	two-piece, vertically split; stacked into 298-mm-long modules; slid around collared coil assembly and welded	three-piece, vertically split; stacked into 500-mm-long modules
Yoke Midplane Gap	open at room temperature, closed cold	open at room temperature, closed cold	open at room temperature, closed cold	closed at room temperature
Yoke Alignment	anti-torsion key on bottom of one half-shell (MTP1A3 only)	anti-torsion keys on bottom of both half-shells	stainless steel strips on both sides of yoke assembly midplane	anti-torsion bars on sides of yoke assembly to which the half-shells are welded
Yoke/Shell Sliding Sheet	n/a	n/a	n/a	2x0.5-mm-thick phosphor-bronze sliding sheets
Shrinking Cylinder	stainless steel, TIG welded	stainless steel, TIG welded	stainless steel, TIG welded	stainless steel, TIG and MIG welded on anti-torsion bars

Table 2. Summary of Young's modulii estimated from azimuthal size measurements performed on the coils used in 10-m-long, 50-mm-twin-aperture, LHC dipole magnet prototypes. The data are in GPa and correspond to averages over the straight sections of the four inner and four outer coils of each magnet. They are estimated from the slopes of the unloading branches of the strain-stress curves at the pressures specified in brackets.

Magnet	Inner Coils	Outer Coils
MTP1A1	31 (@ 80 MPa)	25 (@ 55 MPa)
MTP1A2	33 (@ 80 MPa)	26 (@ 55 MPa)
MTP1A3	32 (@ 80 MPa)	25 (@ 55 MPa)
MTP1N1	30 (@ 80 MPa)	22 (@ 50 MPa)
MTP1N2	31 (@ 80 MPa)	18 (@ 50 MPa
MTP1AJ	21 (@ 80 MPa)	9 (@ 55 MPa)
MTP1EH	36 (@ 80 MPa)	15 (@ 50 MPa)

Table 3(a). Summary of coil azimuthal sizes and of collaring shim thicknesses in the straight section of 10-m-long, 50-mm-twin-aperture LHC/Ansaldo dipole magnet prototype MTP1A1.

	Aperture 1		Aperture 2	
	Left	Right	Left	Right
Inner Layer				
Upper Inner Coil ID	1I		3I	
Upper Pole Shim Thickness (μm; nominal value is 875)	650	650	600	600
Left/Right Average of Upper Coil Size Deviation (μm)[a]	+240		+265	
Left/Right Average of Upper Coil Young's Modulus (GPa)[b]	30.6		30.2	
Upper Midplane Shim Thickness (μm)	none	none	none	none
Lower Midplane Shim Thickness (μm)	none	none	none	none
Left/Right Average of Lower Coil Size Deviation (μm)[a]	+378		+270	
Left/Right Average of Lower Coil Young's Modulus (GPa)[b]	32.5		32.2	
Lower Pole Shim Thickness (μm; nominal value is 875)	500	500	600	600
Lower Inner Coil ID	5I		2I	
Outer Layer				
Upper Outer Coil ID	4E		3E	
Upper Pole Shim Thickness (μm; nominal value is 1000)	450	450	500	500
Left/Right Average of Upper Coil Size Deviation (μm)[c]	+601		+532	
Left/Right Average of Upper Coil Young's Modulus (GPa)[d]	25.6		22.7	
Upper Midplane Shim Thickness (μm)	none	none	none	none
Lower Mipdlane Shim Thickness (μm)	none	none	none	none
Left/Right Average of Lower Coil Size Deviation (μm)[c]	+626		+766	
Left/Right Average of Lower Coil Young's Modulus (GPa)[d]	22.9		28.2	
Lower Pole Shim Thickness (μm; nominal value is 1000)	400	400	300	300
Lower Outer Coil ID	5E		1E	

[a] with respect to calibrated master; at 80 MPa while unloading
[b] from coil sizes between 90 MPa and 70 MPa while unloading
[c] with respect to calibrated master; at 55 MPa while unloading
[d] from coil sizes between 65 MPa and 45 MPa while unloading

Table 3(b). Summary of coil azimuthal sizes and of collaring shim thicknesses in the straight section of 10-m-long, 50-mm-twin-Aperture LHC/Ansaldo dipole magnet prototype MTP1A2.

	Aperture 1		Aperture 2	
	Left	Right	Left	Right
Inner Layer				
Upper Inner Coil ID	12I		11I	
Upper Pole Shim Thickness (μm; nominal value is 875)	600	600	650	650
Upper Coil Size Deviation (μm)[a]	+314		+254	
Upper Coil Young's Modulus (GPa)[b]	33.0		33.2	
Upper Midplane Shim Thickness (μm)	none	none	none	none
Lower Midplane Shim Thickness (μm)	none	none	none	none
Lower Coil Size Deviation (μm)[a]	+330		+273	
Lower Coil Young's Modulus (GPa)[b]	32.6		32.1	
Lower Pole Shim Thickness (μm; nominal value is 875)	600	600	650	650
Lower Inner Coil ID	14I		13I	
Outer Layer				
Upper Outer Coil ID	12E		11E	
Upper Pole Shim Thickness (μm; nominal value is 1000)	1050	1050	900	900
Upper Coil Size Deviation (μm)[c]	+48.8		+180	
Upper Coil Young's Modulus (GPa)[d]	27.3		25.9	
Upper Midplane Shim Thickness (μm)	none	none	none	none
Lower Mipdlane Shim Thickness (μm)	none	none	none	none
Lower Coil Size Deviation (μm)[c]	+168		+102	
Lower Coil Young's Modulus (GPa)[d]	23.5		24.8	
Lower Pole Shim Thickness (μm; nominal value is 1000)	950	950	1000	1000
Lower Outer Coil ID	10E		13E	

[a] with respect to calibrated master; at 80 MPa while unloading
[b] from coil sizes between 90 MPa and 70 MPa while unloading
[c] with respect to calibrated master; at 55 MPa while unloading
[d] from coil sizes between 65 MPa and 45 MPa while unloading

Table 3(c). Summary of coil azimuthal sizes and of collaring shim thicknesses in the straight section of 10-m-long, 50-mm-twin-aperture LHC/Ansaldo Dipole Magnet Prototype MTP1A3.

	Aperture 1		Aperture 2	
	Left	Right	Left	Right
Inner Layer				
Upper Inner Coil ID	6I		8I	
Upper Pole Shim Thickness (μm; nominal value is 875)	600	600	550	550
Upper Coil Size Deviation (μm)[a]	+323		+368	
Upper Coil Young's Modulus (GPa)[b]	30.5		33.0	
Upper Midplane Shim Thickness (μm)	none[c]	none[c]	none[c]	none[c]
Lower Midplane Shim Thickness (μm)	none[c]	none[c]	none[c]	none[c]
Lower Coil Size Deviation (μm)[a]	+333		+306.5	
Lower Coil Young's Modulus (GPa)[b]	33.9		30.8	
Lower Pole Shim Thickness (μm; nominal value is 875)	550	550	600	600
Lower Inner Coil ID	7I		10I	
Outer Layer				
Upper Inner Coil ID	6E		8E	
Upper Pole Shim Thickness (μm; nominal value is 1000)	850	850	1000	1000
Upper Coil Size Deviation (μm)[d]	+217		+79.65	
Upper Coil Young's Modulus (GPa)[e]	24.7		24.1	
Upper Midplane Shim Thickness (μm)	none	none	none	none
Lower Mipdlane Shim Thickness (μm)	none	none	none	none
Lower Coil Size Deviation (μm)[d]	+208		+169.5	
Lower Coil Young's Modulus (GPa)[e]	24.8		24.6	
Lower Pole Shim Thickness (μm; nominal value is 1000)	900	900	900	900
Lower Inner Coil ID	7E		9E	

[a] with respect to calibrated master; at 80 MPa while unloading
[b] from coil sizes between 90 MPa and 70 MPa while unloading
[c] L-shaped, 40-to-50-μm-thick Kapton® reinforcements at outer corners of inner coil midplane faces
[d] with respect to calibrated master; at 55 MPa while unloading
[e] from coil sizes between 65 MPa and 45 MPa while unloading

Table 3(d). Summary of coil azimuthal sizes and of collaring shim thicknesses in the straight section of 10-m-long, 50-mm-twin-aperture LHC/Noell dipole magnet prototype MTP1N1.

	Aperture 1		Aperture 2	
	Left	Right	Left	Right
Inner Layer				
Upper Inner Coil ID	I1		I2	
Upper Pole Shim Thickness (μm; nominal value is 1000)	1000	1000	975	975
Upper Coil Size Deviation (μm)[a]	–43.5		–20.0	
Upper Coil Young's Modulus (GPa)[b]	29.4		30.6	
Upper Midplane Shim Thickness (μm)	none[c]	none[c]	none[c]	none[c]
Lower Midplane Shim Thickness (μm)	none[c]	none[c]	none[c]	none[c]
Lower Coil Size Deviation (μm)[a]	–4.0		–24.5	
Lower Coil Young's Modulus (GPa)[b]	31.5		28.7	
Lower Pole Shim Thickness (μm; nominal value is 1000)	1000	1000	1000	1000
Lower Inner Coil ID	I3		I4	
Outer Layer				
Upper Outer Coil ID	A1		A2	
Upper Pole Shim Thickness (μm; nominal value is 875)	875	875	875	875
Upper Coil Size Deviation (μm)[d]	–168.5		–145.5	
Upper Coil Young's Modulus (GPa)[e]	19.0		23.4	
Upper Midplane Shim Thickness (μm)	200	200	200	200
Lower Mipdlane Shim Thickness (μm)	175	175	175	175
Lower Coil Size Deviation (μm)[d]	–109.0		–120.0	
Lower Coil Young's Modulus (GPa)[e]	23.7		20.5	
Lower Pole Shim Thickness (μm; nominal value is 875)	875	875	875	875
Lower Outer Coil ID	A4		A3	

[a] with respect to calibrated master; at 80 MPa while unloading
[b] from coil sizes at 100 MPa and 60 MPa while unloading
[c] L-shaped, 40-to-50-μm-thick Kapton® reinforcements at outer corners of inner coil midplane faces
[c] with respect to calibrated master; at 50 MPa while unloading
[d] from coil sizes at 65 MPa and 35 MPa while unloading

Table 3(e). Summary of coil azimuthal sizes and of collaring shim thicknesses in the straight section of 10-m-long, 50-mm-twin-aperture LHC/Noell dipole magnet prototype MTP1N2.

	Aperture 1		Aperture 2	
	Left	Right	Left	Right
Inner Layer				
Upper Inner Coil ID	I5		I7	
Upper Pole Shim Thickness (μm; nominal value is 1000)	1000	1000	1000	1000
Upper Coil Size Deviation (μm)[a]	–22.3		–37.4	
Upper Coil Young's Modulus (GPa)[b]	30.1		31.4	
Upper Midplane Shim Thickness (μm)[c]	none	none	none	none
Lower Midplane Shim Thickness (μm)[c]	none	none	none	none
Lower Coil Size Deviation (μm)[a]	+8.2		–44.3	
Lower Coil Young's Modulus (GPa)[b]	30.1		30.7	
Lower Pole Shim Thickness (μm; nominal value is 1000)	1000	1000	1000	1000
Lower Inner Coil ID	I6		I8	
Outer Layer				
Upper Outer Coil ID	A5		A6	
Upper Pole Shim Thickness (μm; nominal value is 875)	875	875	875	875
Upper Coil Size Deviation (μm)[d]	–84.4		–134	
Upper Coil Young's Modulus (GPa)[e]	16.6		17.8	
Upper Midplane Shim Thickness (μm)	100	100	150	150
Lower Mipdlane Shim Thickness (μm)	150	150	150	150
Lower Coil Size Deviation (μm)[d]	–126		–154	
Lower Coil Young's Modulus (GPa)[e]	18.4		18.1	
Lower Pole Shim Thickness (μm; nominal value is 875)	875	875	875	875
Lower Outer Coil ID	A7		A8	

a) with respect to calibrated master; at 80 MPa while unloading
b) from coil sizes at 100 MPa and 60 MPa while unloading
c) L-shaped, 40-to-50-μm-thick Kapton® reinforcements at outer corners of inner coil midplane faces
d) with respect to calibrated master; at 50 MPa while unloading
e) from coil sizes at 65 MPa and 35 MPa while unloading

Table 3(f). Summary of coil azimuthal sizes and of collaring shim thicknesses in the straight section of 10-m-long, 50-mm-twin-aperture LHC/Alshtom-Jeumont dipole magnet prototype MTP1AJ.

	Aperture 1		Aperture 2	
	Left	Right	Left	Right
Inner Layer				
Upper Inner Coil ID	4		1	
Upper Pole Shim Thickness (μm; nominal value is 1000)	1000	1000	1070	1010
Upper Coil Size Deviation (μm)[a]	+142	+136	+100	+129
Upper Coil Loading/Unloading Spring Rates (MN/(m*m))[b]	3635/5141	3739/6086	3632/5269	3672/5919
Upper Midplane Shim Thickness (μm)	none	none	none	none
Lower Midplane Shim Thickness (μm)	none	none	none	none
Lower Coil Size Deviation (μm)[a]	+251	+166	+157	+133
Lower Coil Loading/Unloading Spring Rates (MN/(m*m))[b]	3709/5183	3627/4570	3520/5717	3522/5140
Lower Pole Shim Thickness (μm; nominal value is 1000)	1000	1000	1010	1070
Lower Inner Coil ID	2		3	
Outer Layer				
Upper Outer Coil ID	4		1	
Upper Pole Shim Thickness (μm; nominal value is 830+500)	600+500	600+500	700+500	830+500
Upper Coil Size Deviation (μm)[c]	+354	+370	+222	+143
Upper Coil Loading/Unloading Spring Rates (MN/(m*m))[d]	3131/3150	3089/3423	3110/3228	2989/3284
Upper Midplane Shim Thickness (μm)	none	none	none	none
Lower Mipdlane Shim Thickness (μm)	none	none	none	none
Lower Coil Size Deviation (μm)[c]	+355	+309	+196	+218
Upper Coil Loading/Unloading Spring Rates (MN/(m*m))[d]	3110/3351	2977/3058	3191/3512	3027/3123
Lower Pole Shim Thickness (μm; nominal value is 830+500)	600+500	600+500	830+500	700+500
Lower Outer Coil ID	2		3	

[a] includes ground insulation and Kapton® reinforcements; with respect to calibrated master; at 80 MPa while loading
[b] from slopes of loading /unloading branches of coil stress-strain curve; at 65 MPa while unloading
[c] includes ground insulation and Kapton® reinforcements, with respect to calibrated master; at 65 MPa while loading
[d] from slopes of loading /unloading branches of coil stress-strain curve; at 55 MPa while unloading

Table 3(g). Summary of coil azimuthal sizes and of collaring shim thicknesses in the straight section of 10-m-long, 50-mm-twin-aperture LHC/Elin-Holec dipole magnet prototype MTP1EH.

	Aperture 1		Aperture 2	
	Left	Right	Left	Right
Inner Layer				
Upper Inner Coil ID	NI27		NI29	
Upper Pole Shim Thickness (μm; nominal value is 450)	180[a)]+525[b)]	180[a)]+525[b)]	180[a)]+545[b)]	180[a)]+545[b)]
Upper Coil Size Deviation (μm)[c)]	–326		–346	
Upper Coil Young's Modulus (GPa)[d)]	36.1		35.8	
Upper Midplane Shim Thickness (μm)	60	60	60	60
Lower Midplane Shim Thickness (μm)	60	60	60	60
Lower Coil Size Deviation (μm)[c)]	–318		–360	
Lower Coil Young's Modulus (GPa)[d)]	35.5		37.0	
Lower Pole Shim Thickness (μm; nominal value is 450)	180[a)]+515[b)]	180[a)]+515[b)]	180+560[b)]	180+560[b)]
Lower Inner Coil ID	NI26		NI28	
Outer Layer				
Upper Outer Coil ID	NA27		NA29	
Upper Pole Shim Thickness (μm; nominal value is 1340)	60[a)]+1145[b)]	60[a)]+1145[b)]	60[a)]+1225[b)]	60[a)]+1225[b)]
Upper Coil Size Deviation (μm)[e)]	+85		+4	
Upper Coil Young's Modulus (GPa)[f)]	15.4		14.2	
Upper Midplane Shim Thickness (μm)	none	none	none	none
Lower Mipdlane Shim Thickness (μm)	none	none	none	none
Lower Coil Size Deviation (μm)[e)]	+69		+59	
Lower Coil Young's Modulus (GPa)[f)]	15.4		14.5	
Lower Pole Shim Thickness (μm; nominal value is 1340)	60[a)]+1160[b)]	60+1160[b)]	60[a)]+1171[b)]	60[a)]+1170[b)]
Lower Outer Coil ID	NA26		NA28	

a) Kapton
b) Impregnated glass fibers
c) with respect to midplane; at 80 MPa while unloading
d) at 80 MPa while unloading
e) with respect to midplane; at 50 MPa while unloading
f) at 50 MPa while unloading

Table 4(a). Estimating the nominal thicknesses of the pole shims for the inner layers of 10-m-long, 50-mm-twin-aperture, LHC dipole magnet prototypes.

	MTP1Ax	MTP1Nx	MTP1AJ	MTP1EH
Distance Collar/Coil	1.75 mm	1.75 mm	1.75 mm	1.75 mm
Sliding Sheet (A)	n/a	0.50 mm	n/a	0.20+0.10 mm
Pole Caps (B)	7x0.125 mm	6x0.125 mm	6x0.125 mm	8x0.125 mm
Total (A+B)	0.875 mm	1.25 mm	0.75	1.30 mm
Nominal Shim Thickness	0.875 mm	0.50 mm	1.00 mm	0.45 mm

Table 4(b). Estimating the nominal thicknesses of the pole shims for the outer layers of 10-m-long, 50-mm-twin-aperture, LHC dipole magnet prototypes.

	MTP1Ax	MTP1Nx	MTP1AJ	MTP1EH
Distance Collar/Coil	2.25 mm	2.25 mm	2.75 mm	2.75 mm
Ground Insulation (A)	4x0.125 mm	4x0.125 mm	3x0.125 mm	4x0.125 mm
Quench Heater (B)	n/a	0.125	0.295	0.160
Pole Caps (C)	6x0.125 mm	6x0.125 mm	6x0.125 mm	6x0.125 mm
Total (A+B+C)	1.25 mm	1.375 mm	1.42	1.41 mm
Nominal Shim Thickness	1.00 mm	0.875 mm	1.33 mm	1.34 mm

Table 5(a). Spread sheet with size and thickness data needed for the computation of peak stresses for one-step collaring (in μm).

Name	Aperture	Layer	t_{pole}	t_{mid}	top s_{pole}	bot s_{pole}	n s_{pole}	top s_{mid}	bot s_{mid}	top s_m	bot s_m	top s_{offset}	bot s_{offset}	Δl_{collar}
MTP1A1	1	Inner	875	125	650	500	875	0	0	+240	+378	+171.4	+161.4	+12.5
	1	Outer	1250	125	450	400	1000	0	0	+601	+626	+149.1	+166.7	+12.5
	2	Inner	875	125	600	600	875	0	0	+265	+270	+173.7	+162.9	+12.5
	2	Outer	1250	125	500	300	1000	0	0	+532	+766	+168.2	+135.3	+12.5
MTP1A2	1	Inner	875	125	600	600	875	0	0	+314	+330	+159	+161	+25
	1	Outer	1250	125	1050	950	1000	0	0	+49	+168	+148	+162	+25
	2	Inner	875	125	650	650	875	0	0	+254	+273	+158	+163	+25
	2	Outer	1250	125	900	1000	1000	0	0	+180	+102	+147	+154	+25
MTP1A3	1	Inner	875	125	600	550	875	0	0	+323	+333	+172.2	+154.7	+77.5
	1	Outer	1250	125	850	900	1000	0	0	+217	+208	+154.3	+153.9	+37.5
	2	Inner	875	125	550	600	875	0	0	+368	+306.5	+159.1	+170.5	+77.5
	2	Outer	1250	125	1000	900	1000	0	0	+79.7	+169.5	+158.4	+155.2	+37.5
MTP1N1	1	Inner	750	125	1000	1000	1000	0	0	–43.5	–4	+193.8	+180.6	+90
	1	Outer	1375	125	875	875	875	200	175	–168.5	–109	+231.8	+185.9	+50
	2	Inner	750	125	975	1000	1000	0	0	–20	–24.5	+185.9	+198.6	+90
	2	Outer	1375	125	875	875	875	200	175	–145.5	–120	+188.0	+214.8	+50
MTP1N2	1	Inner	750	125	1000	1000	1000	0	0	–22.3	+8.2	+189.3	+189.0	+90
	1	Outer	1375	125	875	875	875	100	150	–84.4	–126.3	+265.3	+239.4	+50
	2	Inner	750	125	1000	1000	1000	0	0	–37.4	–44.3	+181.3	+185.1	+90
	2	Outer	1375	125	875	875	875	150	150	–134.1	–154.3	+246.7	+242.7	+50

Table 5(a) (Cont.).

Name	Aperture	Layer	t_{pole}	t_{mid}	top s_{pole}	bot s_{pole}	n s_{pole}	top s_{mid}	bot s_{mid}	top s_m	bot s_m	top s_{offset}	bot s_{offset}	Δl_{collar}
MTP1AJ	1	Inner/Left	n/a	n/a	1000	1000	1000	0	0	+142.2	+251.2	+374.1	+366.7	+50
	1	Inner/Right	n/a	n/a	1000	1000	1000	0	0	+135.9	+166.4	+363.7	+375.0	+50
	1	Outer/Left	n/a	n/a	600+500	600+500	830+500	0	0	+354	+355	+352.9	+355.3	+50
	1	Outer/Right	n/a	n/a	600+500	600+500	830+500	0	0	+370	+309	+357.7	+371.2	+50
	2	Inner/Left	n/a	n/a	1070	1010	1000	0	0	+100.1	+156.5	+374.4	+386.4	+50
	2	Inner/Right	n/a	n/a	1010	1070	1000	0	0	+129.3	+132.8	+370.4	+386.1	+50
	2	Outer/Left	n/a	n/a	700+500	830+500	830+500	0	0	+222	+196	+355.3	+369.1	+50
	2	Outer/Right	n/a	n/a	830+500	700+500	830+500	0	0	+143	+218	+369.7	+365.0	+50
MTP1EH	1	Inner	1000+300	120	705	695	450	60	60	−326	−318	+145.3	+147.7	0
	1	Outer	1410	120	1205	1220	1340	0	0	+85	+69	+257.0	+257.0	0
	2	Inner	1000+300	120	725	740	450	60	60	−346	−360	+146.5	+141.8	0
	2	Outer	1410	120	1285	1231	1340	0	0	+4	+59	+278.7	+272.9	0

Table 5(b). Spread Sheet with spring rate data needed for the computation of collaring stresses (in MN/(m*m)).

Name	Aperture	Layer	k_{eff}^{top}	k_{eff}^{bot}	$k_{coil,dwn}^{top}$	$k_{coil,up}^{top}$	$k_{coil,dwn}^{bot}$	$k_{coil,up}^{bot}$	$k_{pack,dwn}$	$k_{pack,up}$
MTP1A1	1	Inner	47310	48113	12018	8513	12765	9042	9830	7408
	1	Outer	35689	35840	10026	7102	8969	6353	7486	5648
	2	Inner	47575	47575	11861	8402	12647	8958	9736	7334
	2	Outer	35540	36145	8890	6297	11045	7825	7727	5841
MTP1A2	1	Inner	47575	47575	12963	9182	12792	9061	10134	7654
	1	Outer	33977	34251	10701	7580	9210	6524	7673	5817
	2	Inner	47310	47310	13022	9224	12605	8929	10081	7614
	2	Outer	34390	34114	10153	7192	9723	6887	7700	5837
MTP1A3	1	Inner	47575	47842	11963	8474	13319	9434	9971	7521
	1	Outer	34529	34390	9692	6865	9707	6879	7569	5729
	2	Inner	47842	47575	12950	9173	12080	8557	9905	7468
	2	Outer	34114	34390	9438	6685	9631	6822	7458	5641
MTP1N1	1	Inner	51256	51256	11533	8169	12372	8764	9682	7258
	1	Outer	28255	28652	7442	5271	9279	6573	6402	4848
	2	Inner	51256	51256	12022	8516	11255	7972	9476	7096
	2	Outer	28255	28652	9177	6500	8028	5687	6582	5000
MTP1N2	1	Inner	51256	51256	11806	8363	11828	8378	9604	7196
	1	Outer	29912	29060	6501	4605	7206	5104	5548	4158
	2	Inner	51256	51256	12327	8732	12075	8553	9854	7397
	2	Outer	29060	29060	6991	4952	7108	5035	5672	4262

Table 5(b) (Cont.).

Name	Aperture	Layer	k_{eff}^{top}	k_{eff}^{bot}	$k_{coil,dwn}^{top}$	$k_{coil,up}^{top}$	$k_{coil,dwn}^{bot}$	$k_{coil,up}^{bot}$	$k_{pack,dwn}$	$k_{pack,up}$
MTP1AJ	1	Inner/Left	425000	425000	5141	3635	5183	3709	5100	3640
	1	Inner/Right	425000	425000	6086	3739	4570	3627	5157	3651
	1	Outer/Left	386364	386364	3150	3131	3351	3110	3220	3095
	1	Outer/Right	386364	386364	3423	3089	3058	2977	3203	3008
	2	Inner/Left	397196	420792	5269	3632	5717	3520	5411	3544
	2	Inner/Right	420792	397196	5919	3672	5140	3522	5429	3595
	2	Outer/Left	354167	319549	3228	3110	3284	2989	3225	3021
	2	Outer/Right	319549	354167	3284	2989	3123	3027	3171	2981
MTP1EH	1	Inner	32967	32993	14178	10043	13943	9876	9857	7649
	1	Outer	29354	29324	6031	4272	6031	4272	5003	3729
	2	Inner	32916	32878	14061	9960	14532	10293	9964	7741
	2	Outer	29193	29302	5561	3939	5679	4023	4714	3504

Table 5(c). Spread sheet with collaring stresses (in MPa).

Name	Aperture	Layer	$\sigma_{m,p}$	$\sigma_{m,up}$	$\sigma_{m,dwn}$	σ_t	σ_r	σ_r^*
MTP1A1	1	Inner	100	n/a	80	136	39	54
	1	Outer	80	n/a	55	111	41	33
	2	Inner	100	n/a	80	129	33	49
	2	Outer	80	n/a	55	116	45	37
MTP1A2	1	Inner	100	n/a	80	161	40	59
	1	Outer	80	n/a	55	141	55	45
	2	Inner	100	n/a	80	156	40	59
	2	Outer	80	n/a	55	134	51	42
MTP1A3	1	Inner	100	n/a	80	174	49	70
	1	Outer	80	n/a	55	138	49	40
	2	Inner	100	n/a	80	178	54	75
	2	Outer	80	n/a	55	131	44	34
MTP1N1	1	Inner	125	n/a	80	162	45	64
	1	Outer	125	n/a	50	123	50	42
	2	Inner	125	n/a	80	155	41	60
	2	Outer	125	n/a	50	127	53	45
MTP1N2	1	Inner	125	n/a	80	168	51	70
	1	Outer	125	n/a	50	109	45	38
	2	Inner	125	n/a	80	155	43	61
	2	Outer	125	n/a	50	107	47	39

Table 5(c) (Cont.).

Name	Aperture	Layer	$\sigma_{m,p}$	$\sigma_{m,up}$	$\sigma_{m,dwn}$	σ_t	σ_r	σ_r^*
MTP1AJ	1	Inner/Left	n/a	80	65	132	62	68
	1	Inner/Right	n/a	80	65	123	55	64
	1	Outer/Left	n/a	65	55	96	54	52
	1	Outer/Right	n/a	65	55	93	54	51
	2	Inner/Left	n/a	80	65	125	53	63
	2	Inner/Right	n/a	80	65	127	55	65
	2	Outer/Left	n/a	65	55	99	58	55
	2	Outer/Right	n/a	65	55	93	54	51
MTP1EH	1	Inner	100	n/a	80	115	58(56)	66(65)
	1	Outer	100	n/a	50	72(78)	45(51)	43(49)
	2	Inner	100	n/a	80	116	58(56)	66(65)
	2	Outer	100	n/a	50	71(77)	46(51)	44(49)

Table 6. Estimated azimuthal pre-compressions after collaring completion on average over the straight sections of the coils of 10-m-long, 50-mm-twin-aperture, LHC dipole magnet prototypes (in MPa).

Magnet	Aperture 1		Aperture 2	
	Inner	Outer	Inner	Outer
MTP1A1	46.5±10	37±10	41±10	41±10
MTP1A2	49.5±10	50±10	49.5±10	43±10
MTP1A3	60±10	45±10	65±10	39±10
MTP1N1	54.5±10	46±10	50±10	49±10
MTP1N2	60.5±10	41.5±10	52±10	43±10
MTP1AJ	62±5	53±5	59±5	55±5
MTP1EH	65±10	46±10	65±10	47±10

Table 7. Comparison between estimated and measured vertical deflections on average over the straight sections of the collared-coil assemblies of the 10-m-long, 50-mm-twin-aperture, LHC dipole magnet prototypes (in mm).

Magnet	Aperture 1		Aperture 2	
	Est.	Meas.	Est.	Meas.
MTP1A1	0.44	0.58[a)]	0.43	0.59[b)]
MTP1A2	0.48	0.53[a)]	0.47	0.53[b)]
MTP1A3	0.47	n/a	0.47	n/a
MTP1N1	0.44	0.46[a)]	0.43	0.48[b)]
MTP1N2	0.44	0.48[a)]	0.41	0.48[b)]
MTP1AJ/Left	0.47	0.41[c)]	0.45	0.49[c)]
MTP1AJ/Right	0.44	0. 41[d)]	0.44	0.48[d)]
MTP1EH	0.30	0.36[e)]	0.28	0.33[e)]

[a)] Vertical dimension (B_1B_1') as defined in Fig. 11.
[a)] Vertical dimension (B_2B_2') as defined in Fig. 11.
[c)] Vertical dimension (C_3) as defined in Fig. 17.
[d)] Vertical dimension (C_4) as defined in Fig. 17.
[e)] Average of the vertical dimensions (H_3) and (H_4) defined in Fig. 19.

FIGURE CAPTIONS

Figure 1. Cross-sectional views of the cold masses of 10-m-long, 50-mm-twin-aperture LHC dipole magnet prototypes: (a) Ansaldo magnets MTP1A1, MTP1A2 and MTP1A3, (b) Noell magnets MTP1N1 and MTP1N2, (c) Alsthom/Jeumont magnet MTP1AJ, and (d) Elin/Holec magnet MTP1EH

Figure 2. Measurement of azimuthal coil size and Young's modulus at Noell GmbH.

Figure 3. Examples of stress-strain curves measured on one side of an inner coil assembly package manufactured by Jeumont Industrie. The various curves correspond to measurements at various positions along the coil length.

Figure 4. Summary of azimuthal size deviations measured as a function of axial position on the various coils used in LHC/Ansaldo prototypes MTP1A2 and MTP1A3: (a) inner coils and (b) outer coils. The measurements are averaged over the two coil sides and were taken at 80 MPa while unloading for the inner coils and at 55 MPa while unloading for the outer coils. The values reported here correspond to deviations with respect to masters having the nominal dimensions.

Figure 5. 10-m-long press used at Ansaldo S.p.A for curing and collaring.

Figure 6. Summary of azimuthal size deviations measured as a function of axial position on the various inner coils used in LHC/Noell prototypes: (a) inner coils of MTP1N1 and (b) inner coils of MTP1N2. The measurements are averaged over the two coil sides and were taken at 80 MPa while unloading. The values reported here correspond to deviations with respect to a master having the nominal dimension.

Figure 7. Summary of azimuthal size deviations measured as a function of axial position on the various outer coils used in LHC/Noell prototypes: (a) outer coils of MTP1N1 and (b) outer coils of MTP1N2. The measurements are averaged over the two coil sides and were taken at 50 MPa while unloading. The values reported here correspond to deviations with respect to a master having the nominal dimension.

Figure 8. Summary plot of one-step collaring peak stresses estimated as a function of axial position for magnet MTP1A2.

Figure 9. Summary plot of residual azimuthal pre-compressions after collaring estimated as a function of axial position for magnet MTP1A2.

Figure 10. Summary plot of residual azimuthal pre-compressions after collaring estimated as a function of axial position for magnet MTP1AJ.

Figure 11. Equipment developed at FNAL to measure the deflections of the collared-coil assemblies of the LHC Interaction Region quadrupole magnets [12].

Figure 12. Definitions of the reference surfaces used to measure selected outer dimensions of the collared-coil assemblies of the LHC/Ansaldo and LHC/Noell dipole magnet prototypes.

Figure 13. Summary plot of vertical dimensions (B_1B_1') and (B_2B_2') as a function of axial position measured on both sides of the collared-coil assembly of magnet MTP1A1. The nominal undeflected value is 176 mm.

Figure 14. Summary plots of vertical dimensions (B_1B_1') and (B_2B_2') measured as a function of axial position on both sides of the collared-coil assembly of magnet MTP1A2: (a) at room temperature after collaring completion and (b) at room temperature after a thermal cycle to 77 K. The nominal undeflected value is 176 mm.

Figure 15. Summary plot of elastic elongations computed as a funcion of axial postion along the two pole axes of the collared-coil assembly of magnet MTP1A2. A 50–μm correction is added to the computed elongations to take into account the fact that the tie rods implemented in this collared-coil assembly are not of nominal diameters.

Figure 16. Summary plot of dipole field strength as a function of axial position measured at 1.9 K and 12.8 kA in the two apertures of the three 10-m-long, 50-mm-twin-aperture LHC/Ansaldo dipole magnet prototypes.

Figure 17. Summary plots of vertical dimensions (B_1B_1'), (B_2B_2'), (C_1C_1') and (C_2C_2') measured as a function of axial position on both sides and in the central parts of the collared-coil assemblies of LHC/Noell dipole magnet prototypes: (a) data for magnet MTP1N1 and (b) data for magnet MTP1N2. The nominal undeflected values are 176 mm.

Figure 18. Definitions of the reference surfaces used to measure selected outer dimensions of the collared-coil assemblies of the Alsthom/Jeumont prototype.

Figure 19. Summary plots of vertical dimensions (C_3) and (C_4) measured as a function of axial position on both sides of the collared-coil assemblies of the Alsthom/Jeumont prototype MTP1AJ: (a) after first collaring and (b) after second collaring. The nominal undeflected values are 186 mm

Figure 20. Definitions of the reference surfaces used to measure selected outer dimensions of the collared-coil assemblies of the Elin/Holec prototype.

Figure 21. Summary plots of vertical dimensions (H_3) and (H_4) measured as a function of axial position on both sides of the collared-coil assemblies of the Elin/Holec prototype MTP1EH. The nominal undeflected values are 175 mm.

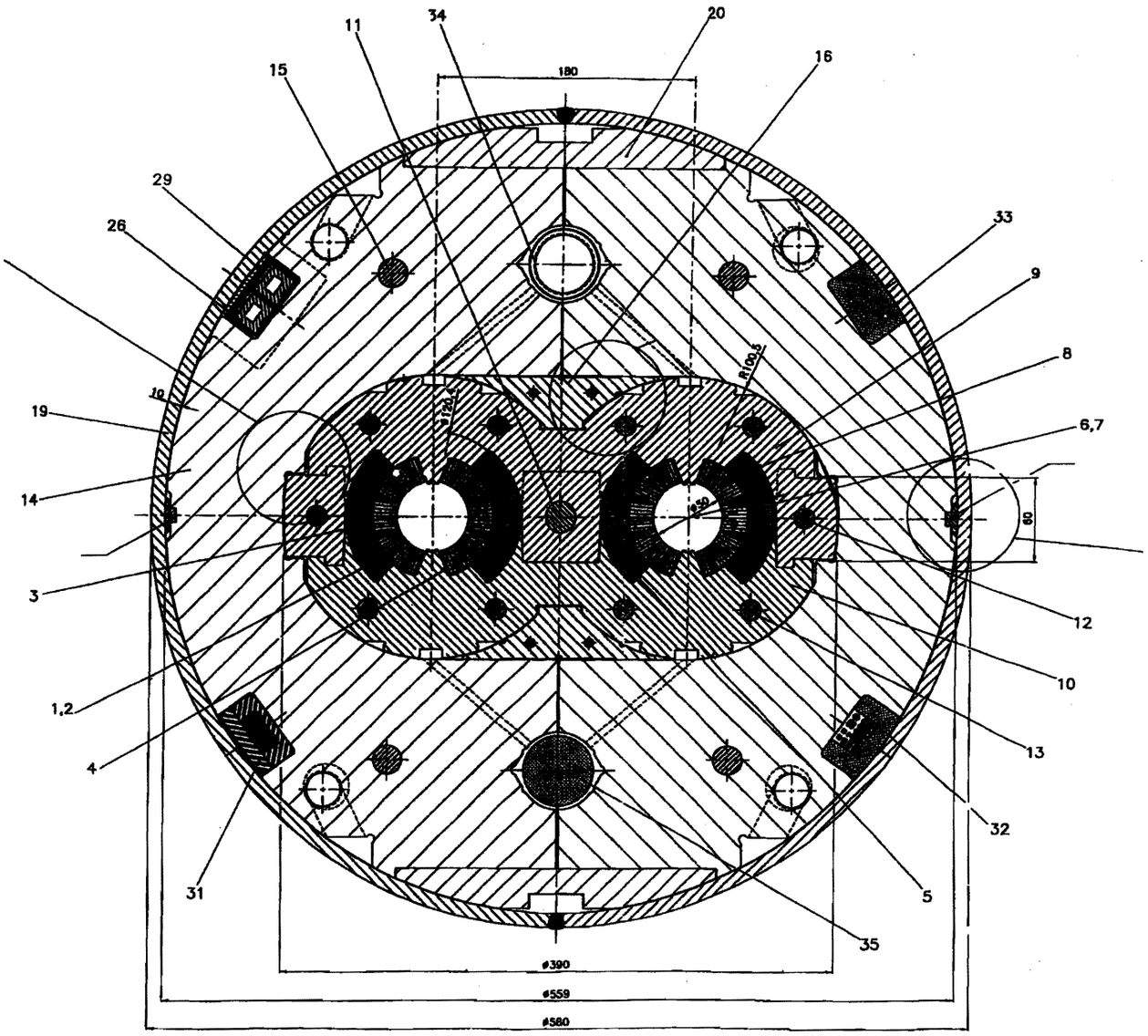

Figure 1(a). Cross-sectional view of the cold masses of 10-m-Long, 50-mm-twin-aperture LHC dipole magnet prototypes MTP1A1, MTP1A2 and MTP1A3.

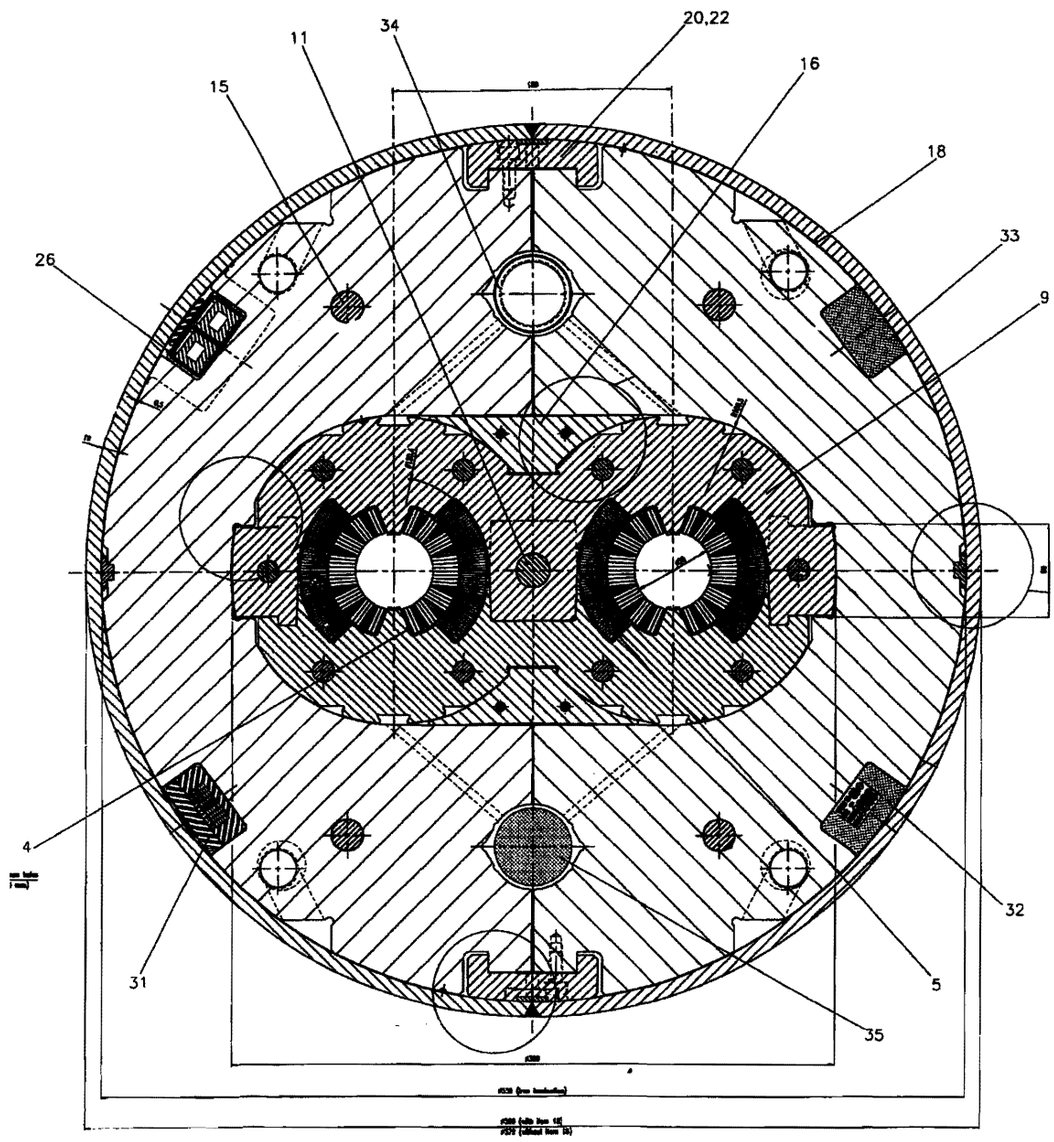

Figure 1(b). Cross-sectional view of the cold masses of 10-m-Long, 50-mm-twin-aperture LHC dipole magnet prototypes MTP1N1 and MTP1N2.

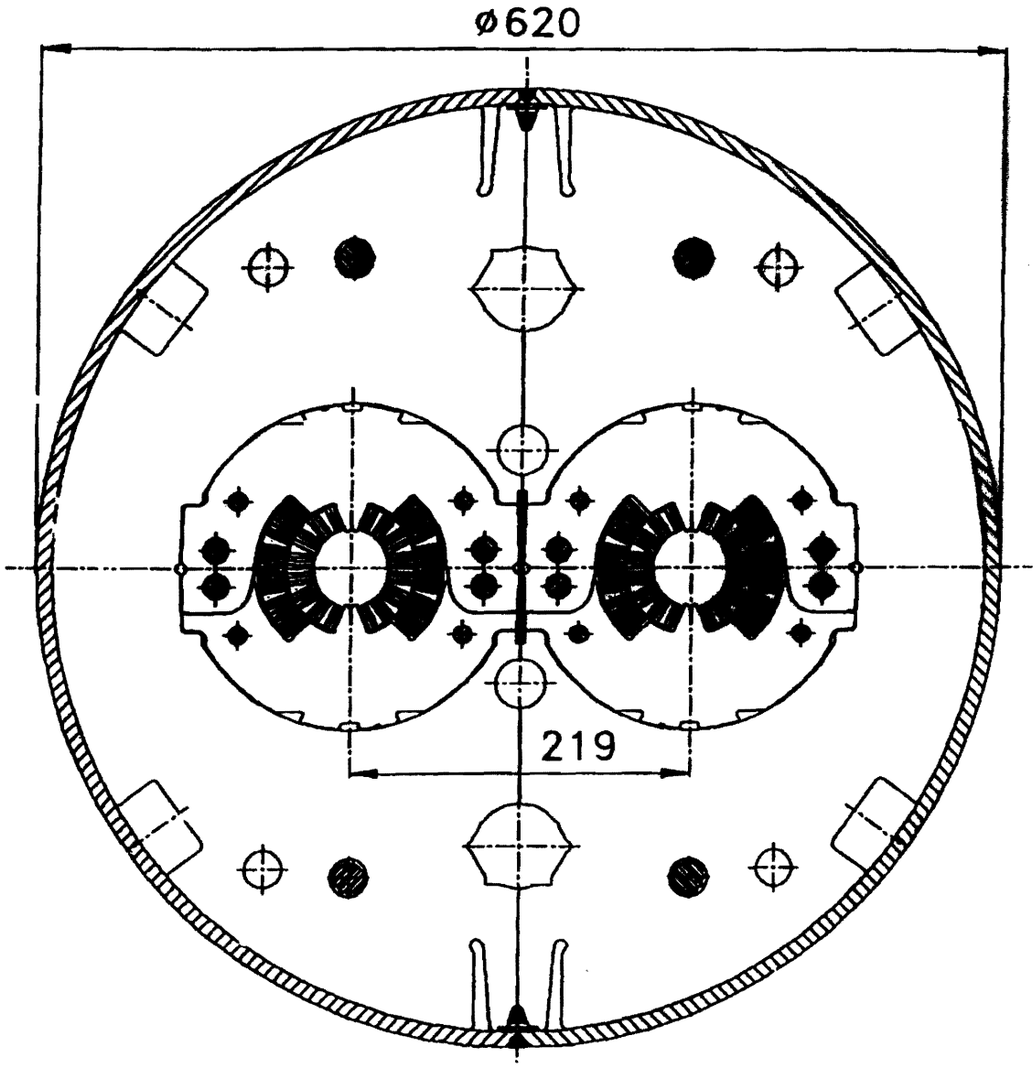

Figure 1(c). Cross-sectional view of the cold mass of 10-m-Long, 50-mm-twin-aperture LHC dipole magnet prototype MTP1AJ.

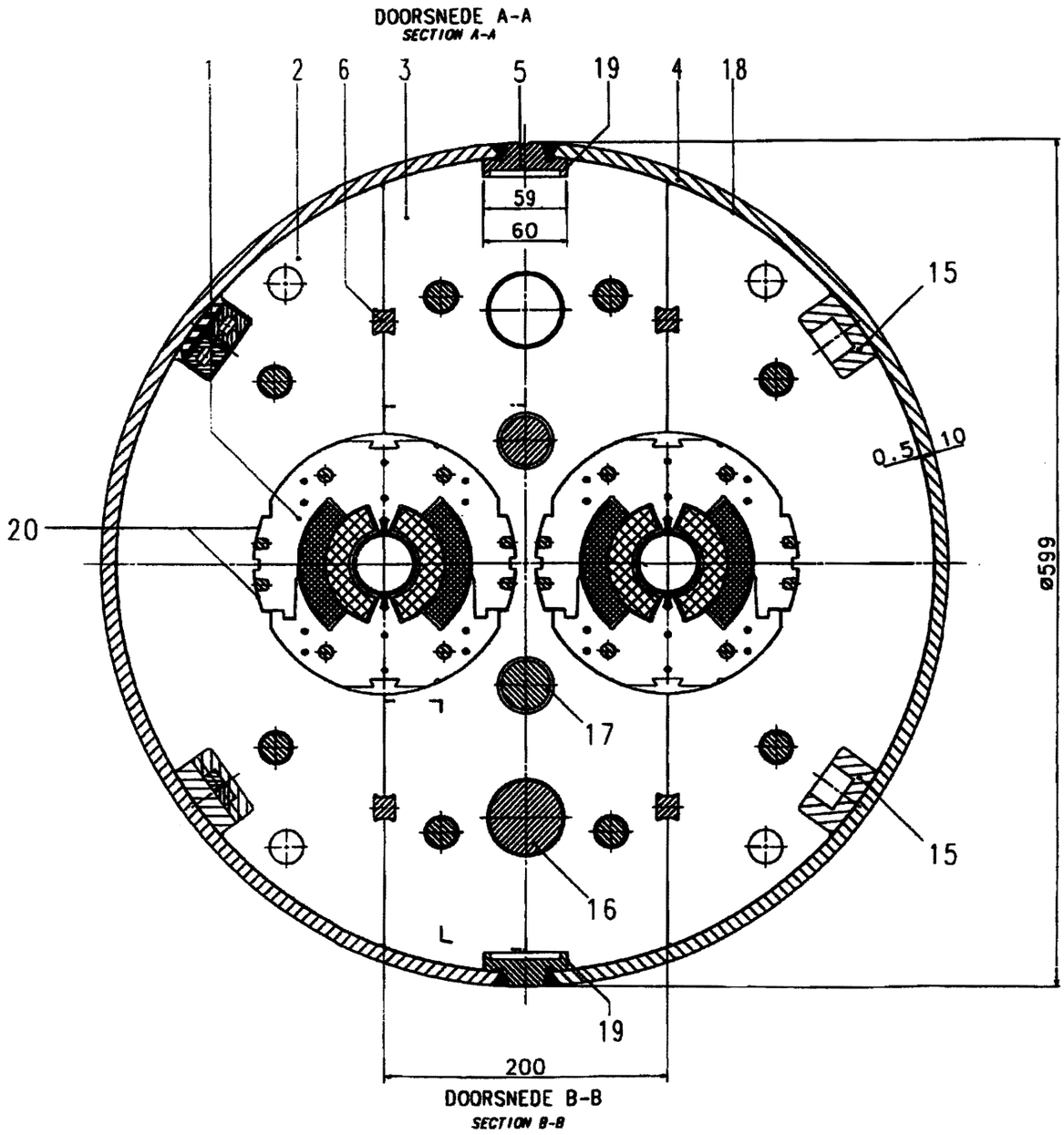

Figure 1(d). Cross-sectional view of the cold mass of 10-m-Long, 50-mm-twin-aperture LHC dipole magnet prototype MTP1EH.

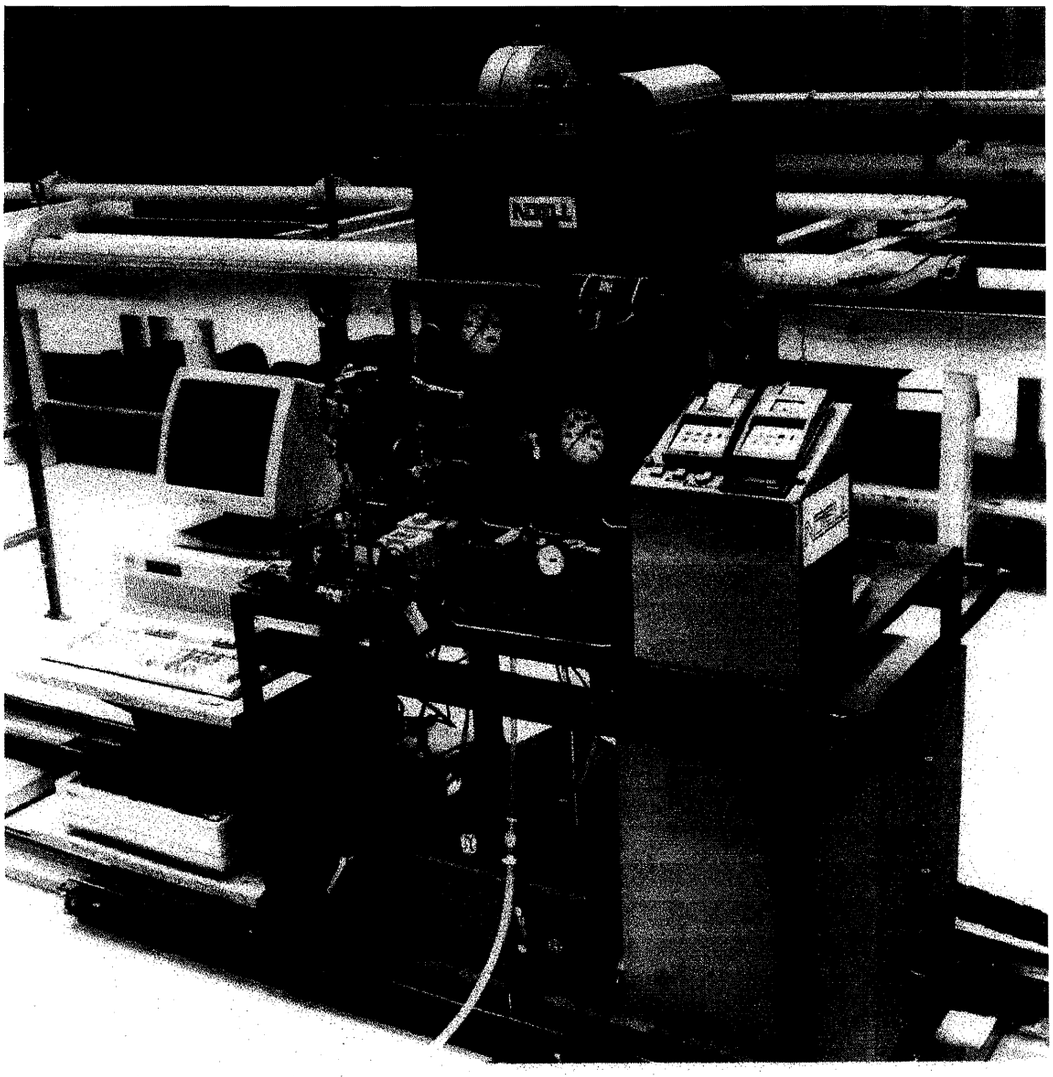

Figure 2. Measurement of azimuthal coil size and Young's modulus at Noell GmbH.

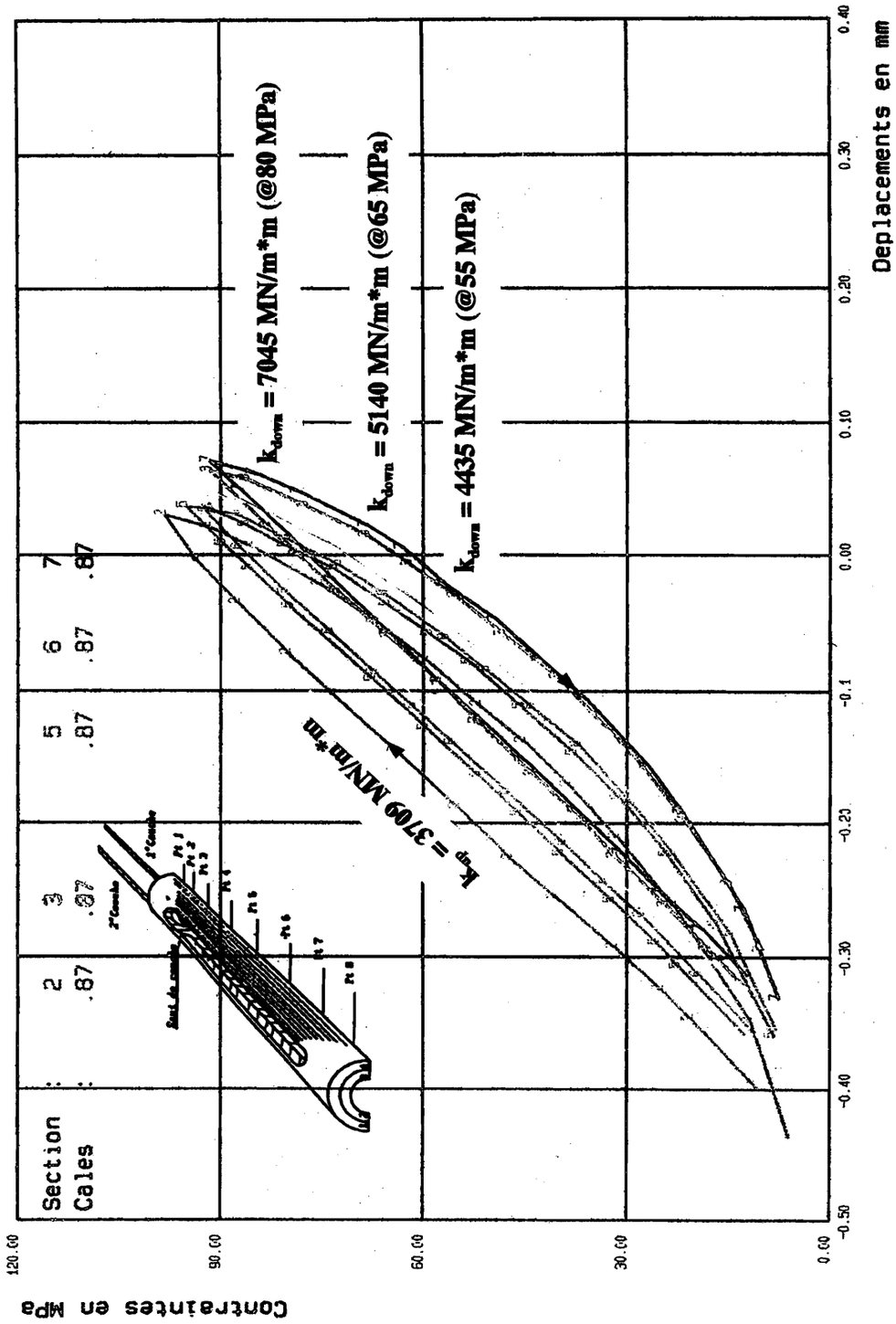

Figure 3. Examples of stress-strain curves measured on one side of an inner coil assembly package manufactured by Jeumont Industrie. The various curves correspond to measurements at various positions along the coil length.

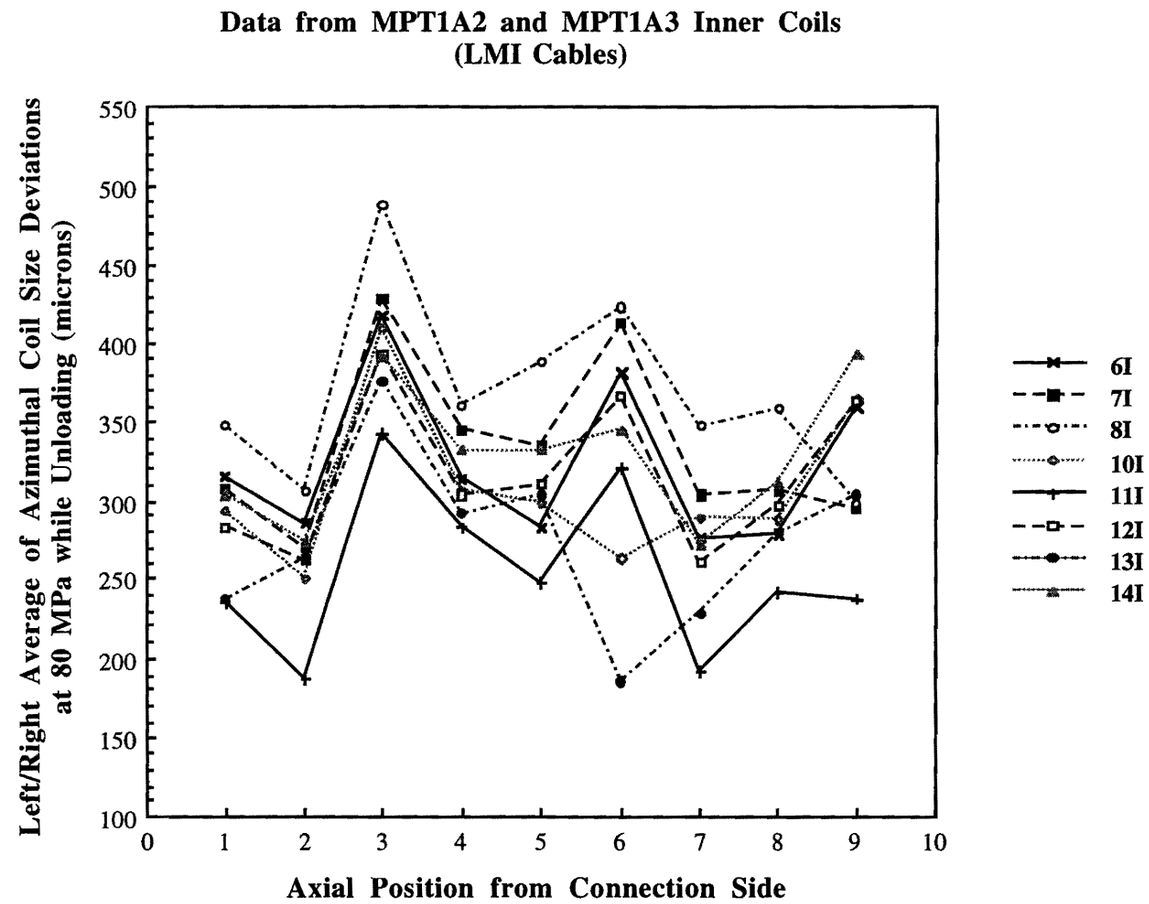

Figure 4(a). Summary of azimuthal size deviations measured as a function of axial position on the various inner coils used in LHC/Ansaldo prototypes MTP1A2 and MTP1A3.

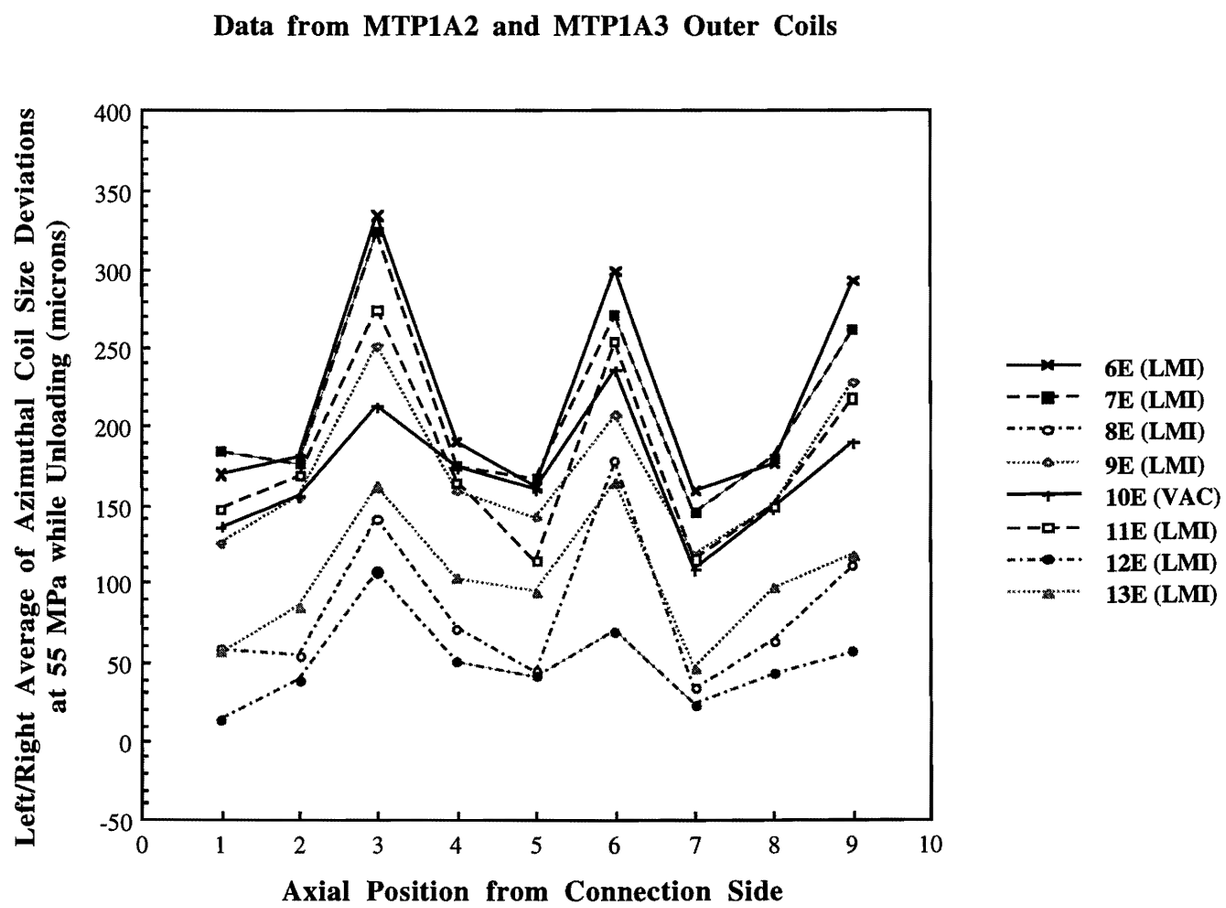

Figure 4(b). Summary of azimuthal size deviations measured as a function of axial position on the various outer coils used in LHC/Ansaldo prototypes MTP1A2 and MTP1A3.

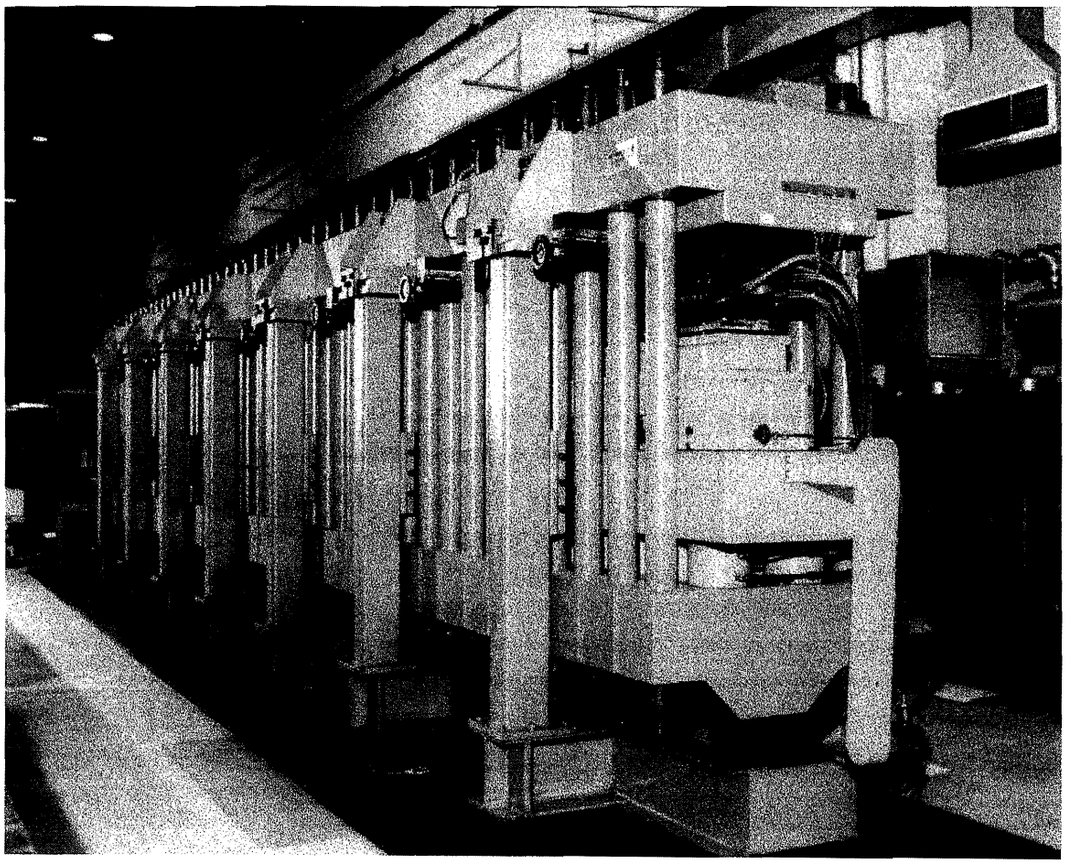

Figure 5. 10-m-long press used at Ansaldo S.p.A for curing and collaring.

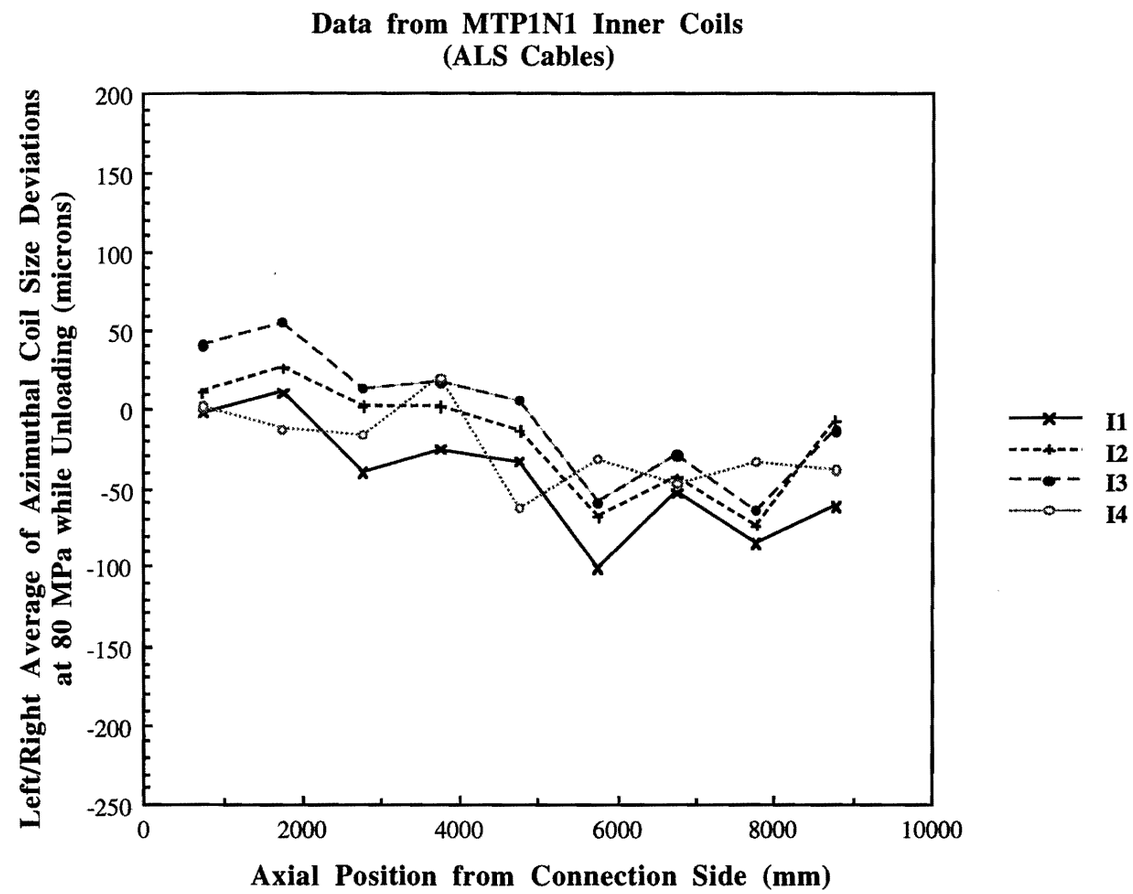

Figure 6(a). Summary of azimuthal size deviations measured as a function of axial position on the various inner coils used in LHC/Noell prototype MTP1N1.

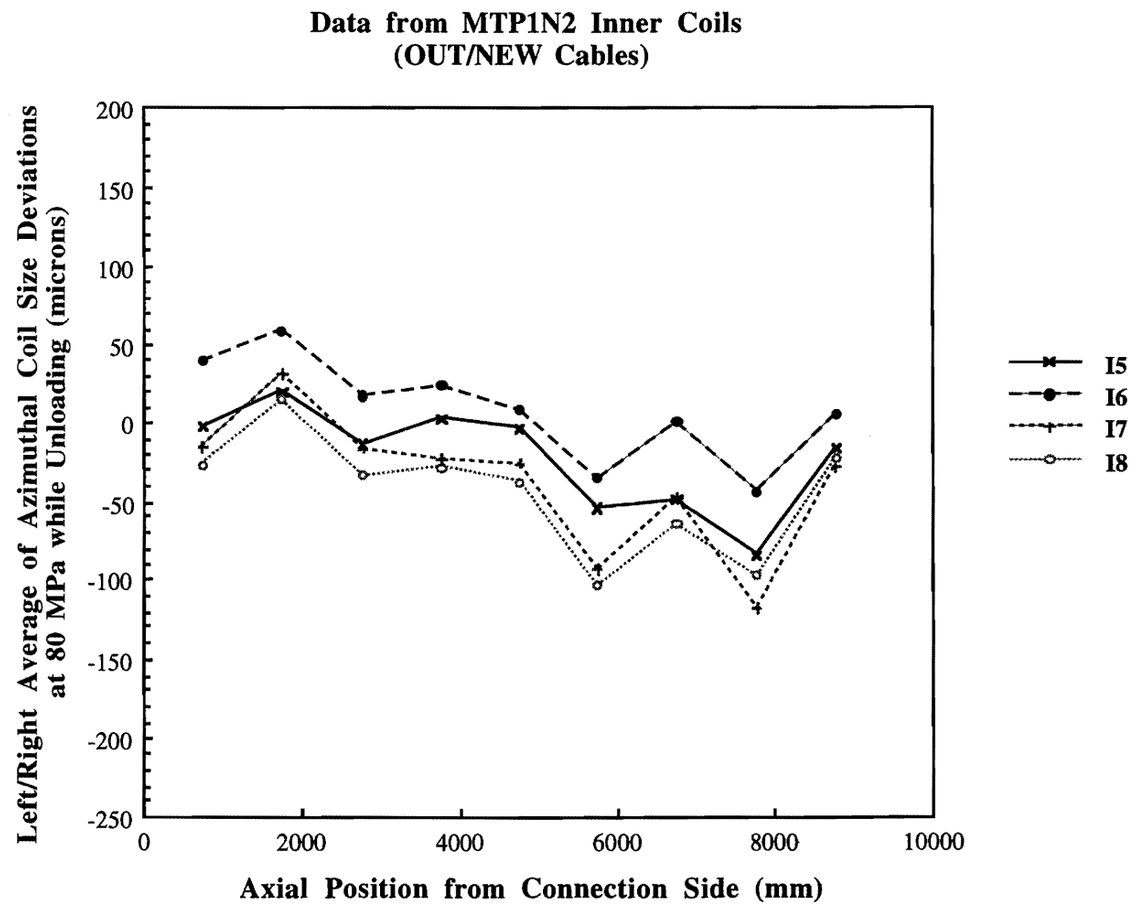

Figure 6(b). Summary of azimuthal size deviations measured as a function of axial position on the various inner coils used in LHC/Noell prototype MTP1N2.

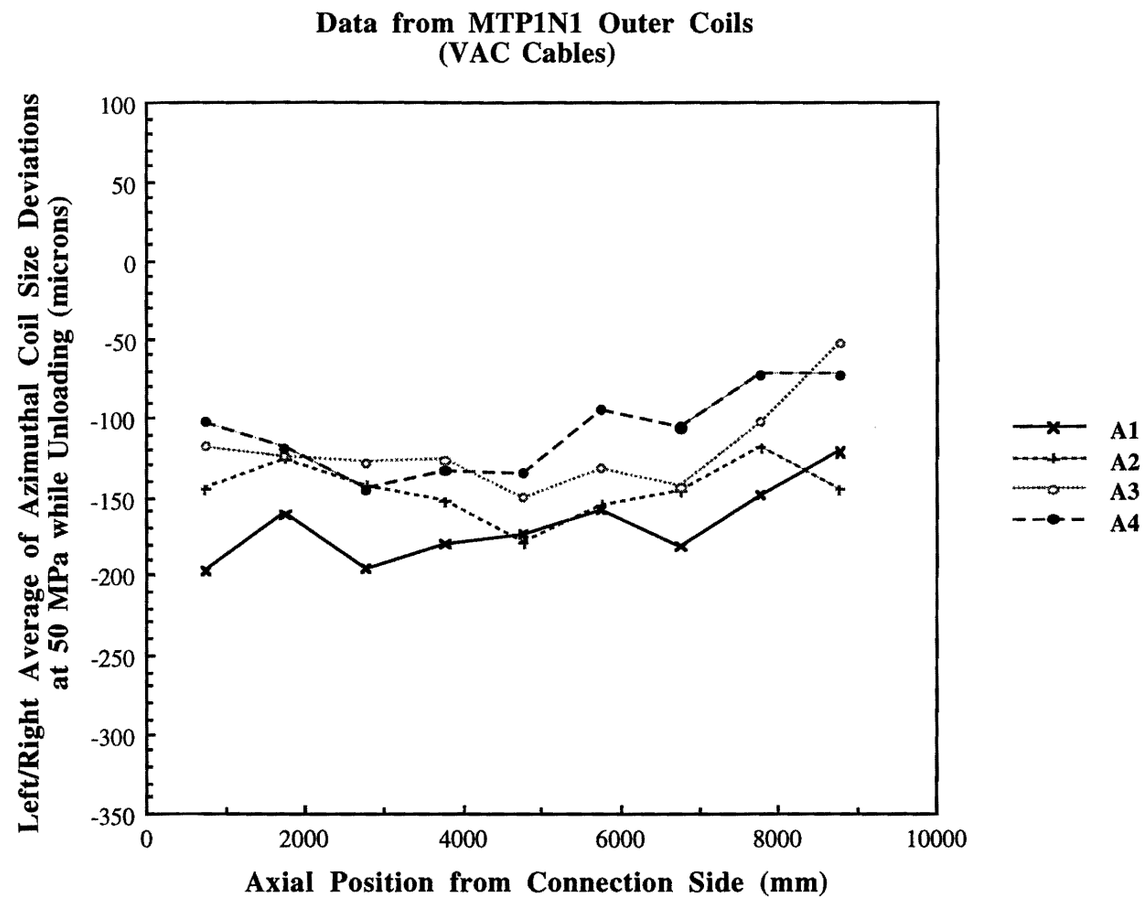

Figure 7(a). Summary of azimuthal size deviations measured as a function of axial position on the various outer coils used in LHC/Noell prototype MTP1N1.

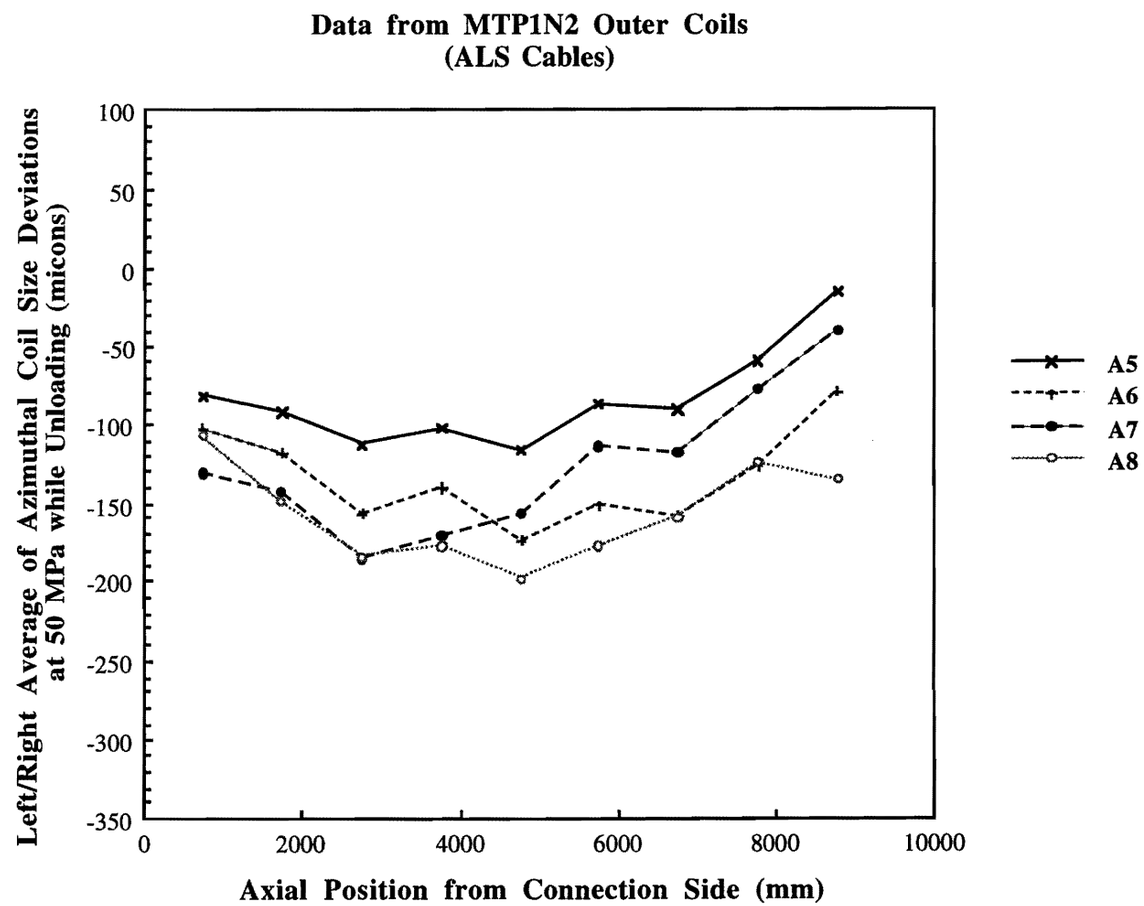

Figure 7(a). Summary of azimuthal size deviations measured as a function of axial position on the various outer coils used in LHC/Noell prototypes MTP1N2.

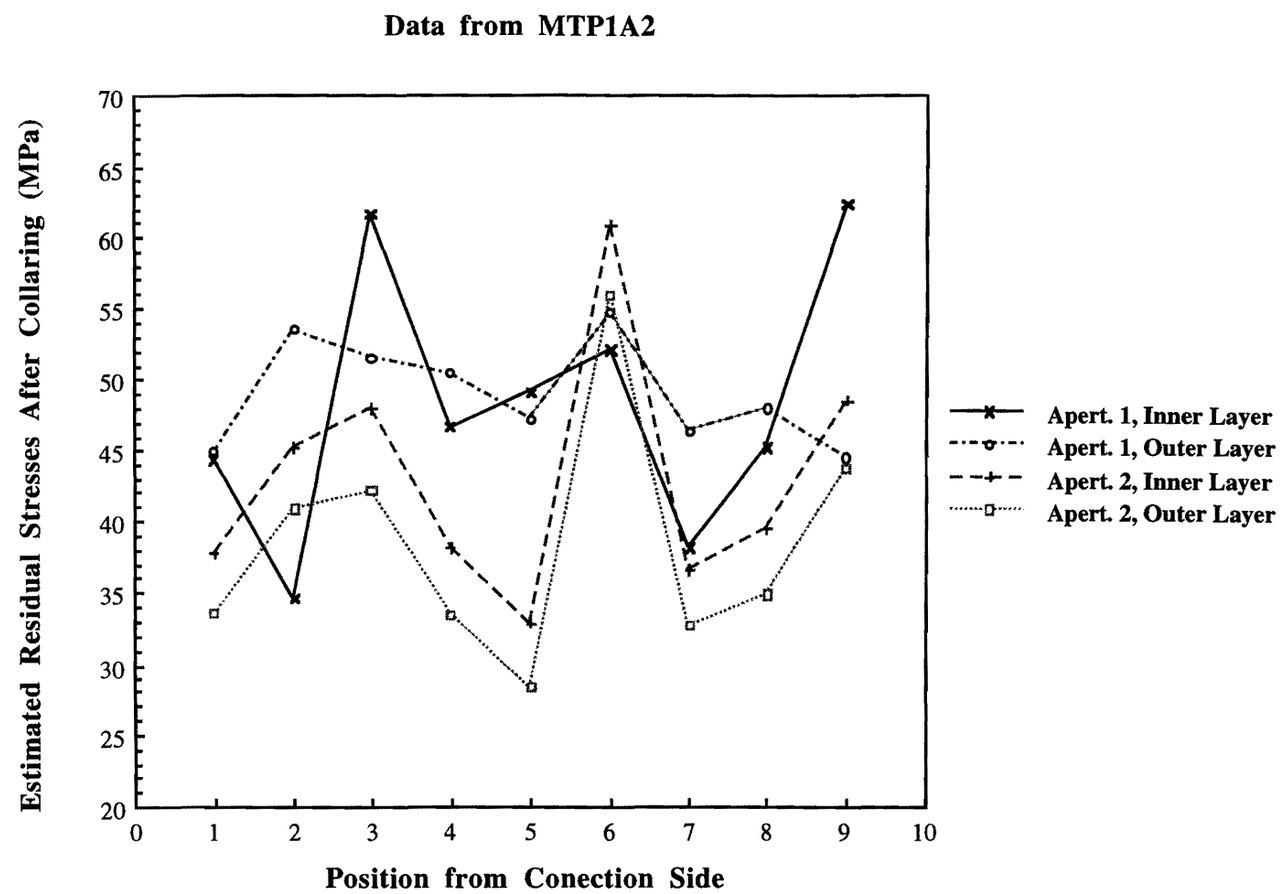

Figure 8. Summary plot of estimated azimuthal pre-compressions as a function of axial position for LHC/Ansaldo prototype MTP1A2.

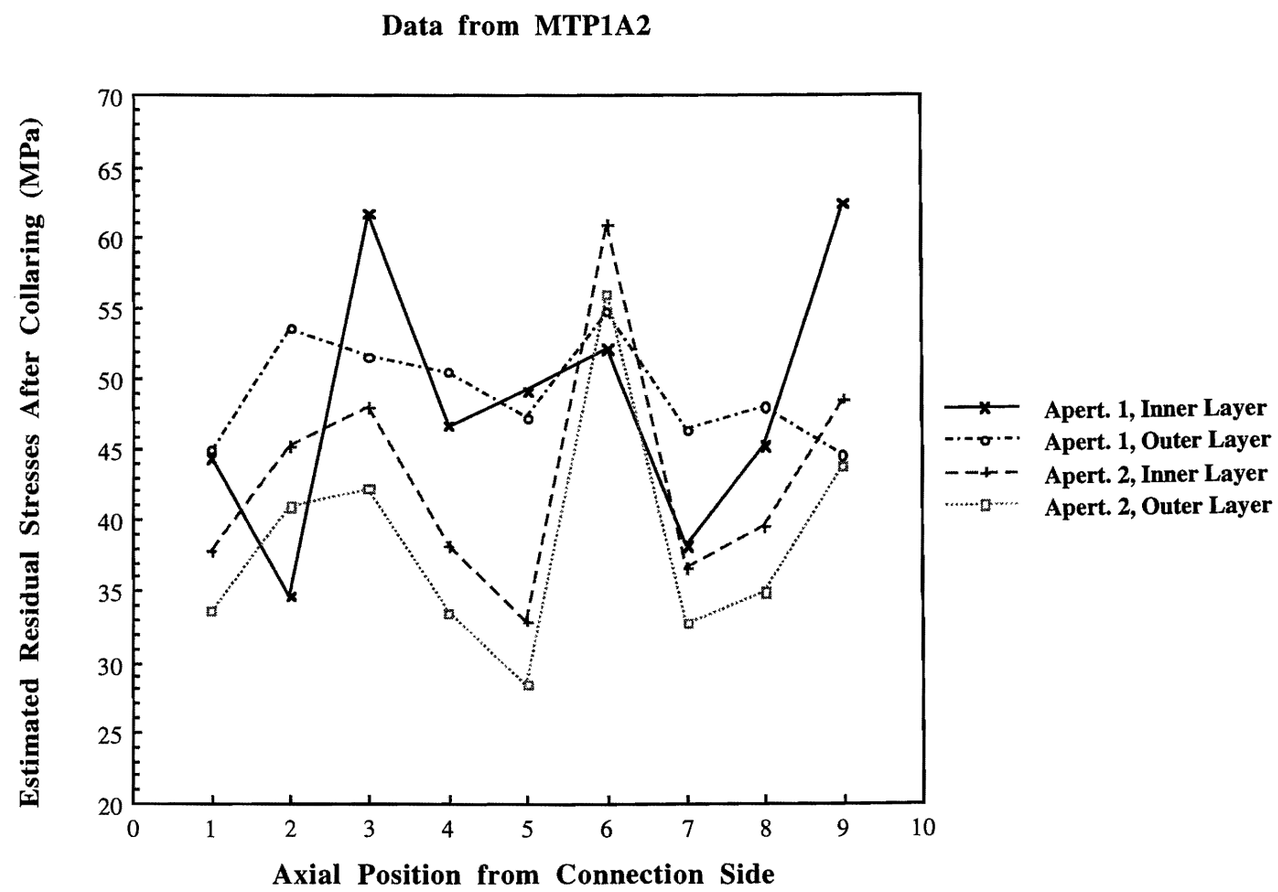

Figure 9. Summary plot of resual azimuthal pre-compressions after collaring estimated as a function of axial position for LHC/Ansaldo prototype MTP1A2.

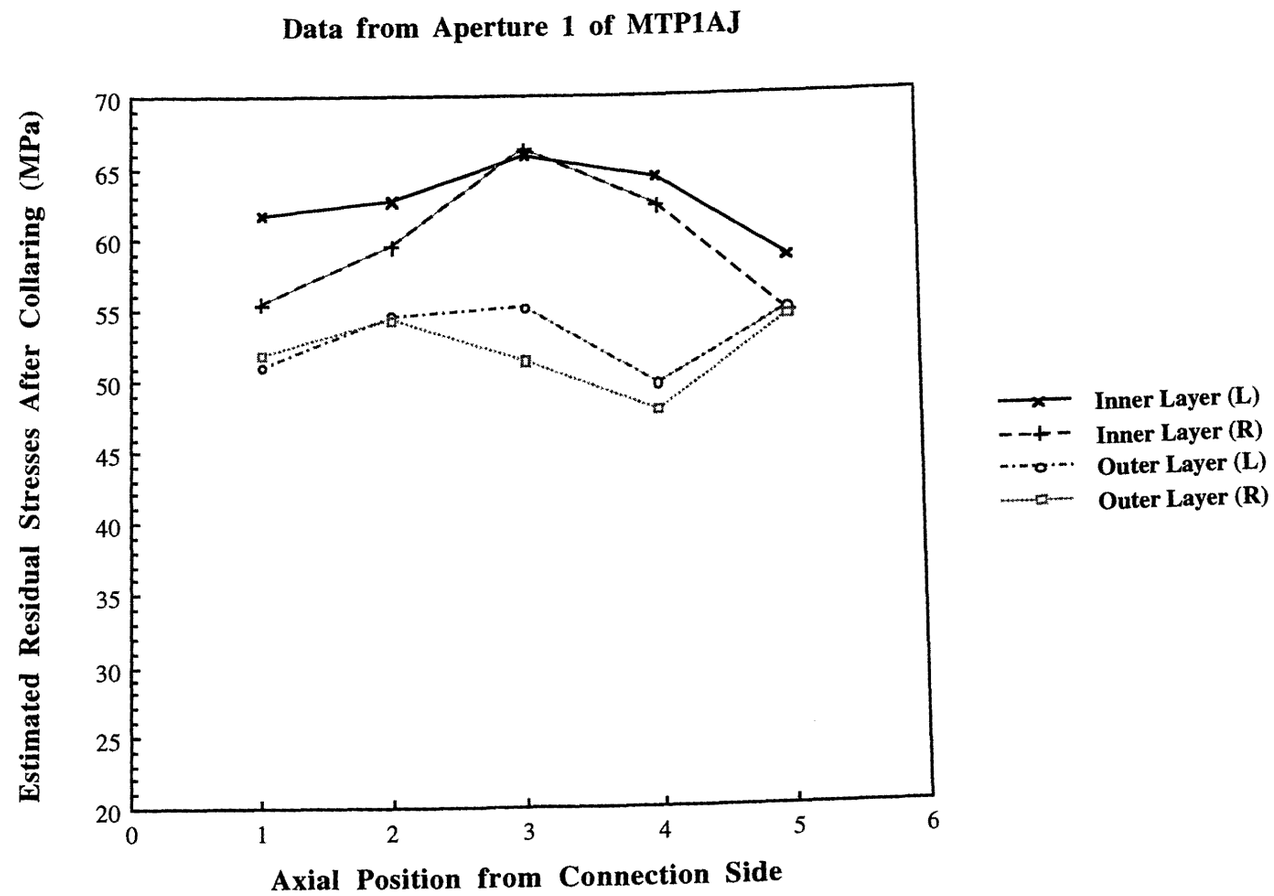

Figure 10. Summary plot of residual azimuthal pre-compressions after collaring estimated as a function of axial position for Aperture 1 of Alstom/Jeumont prototype MTP1AJ.

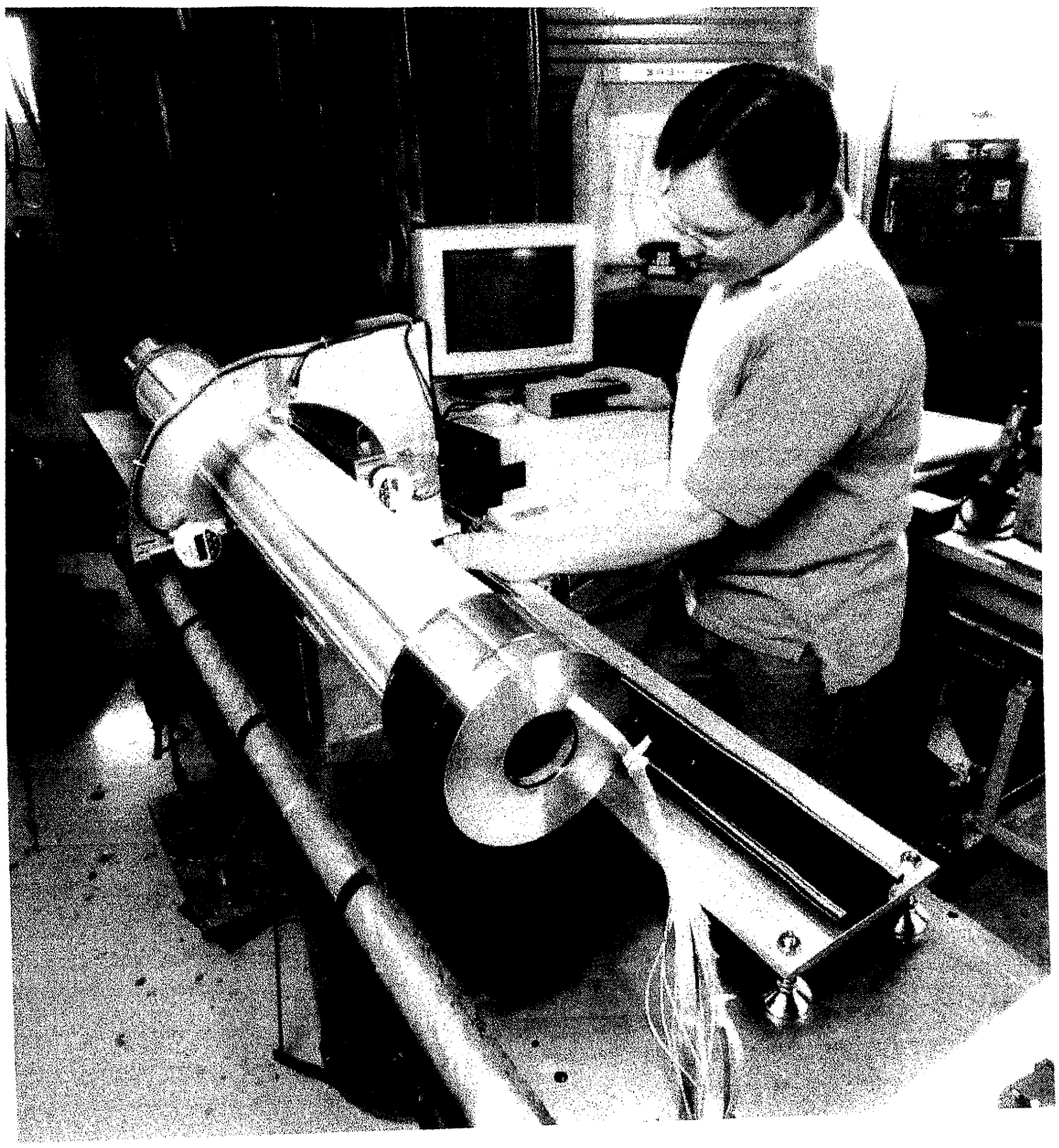

Figure 11. Equipment developed at FNAL to measure the deflections of the collared-coil assemblies of the LHC Interaction Region quadrupole magnets [12].

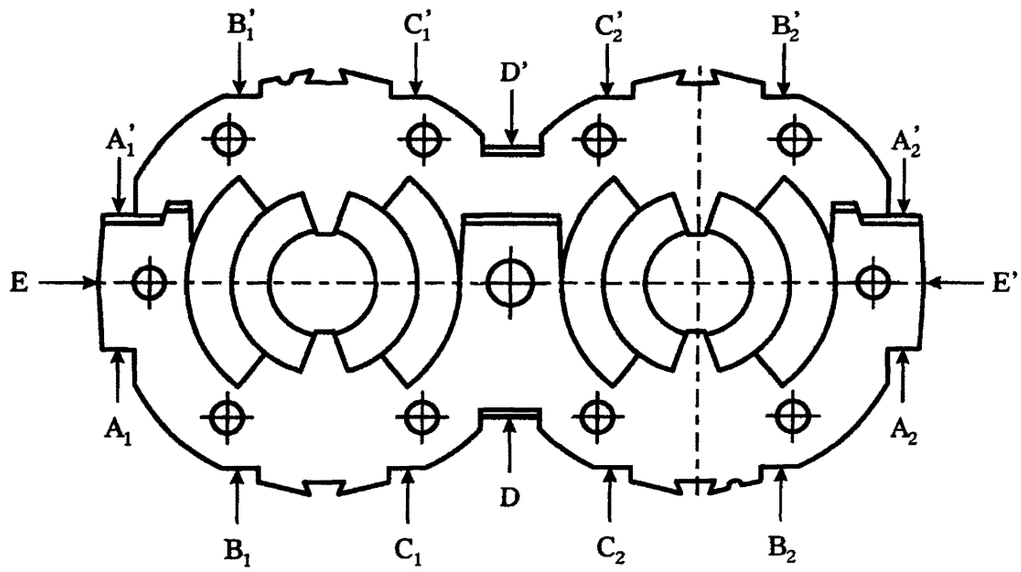

Figure 12. Definitions of the reference surfaces used to measure selected outer dimensions of the collared-coil assemblies of the LHC/Ansaldo and LHC/Noell prototypes.

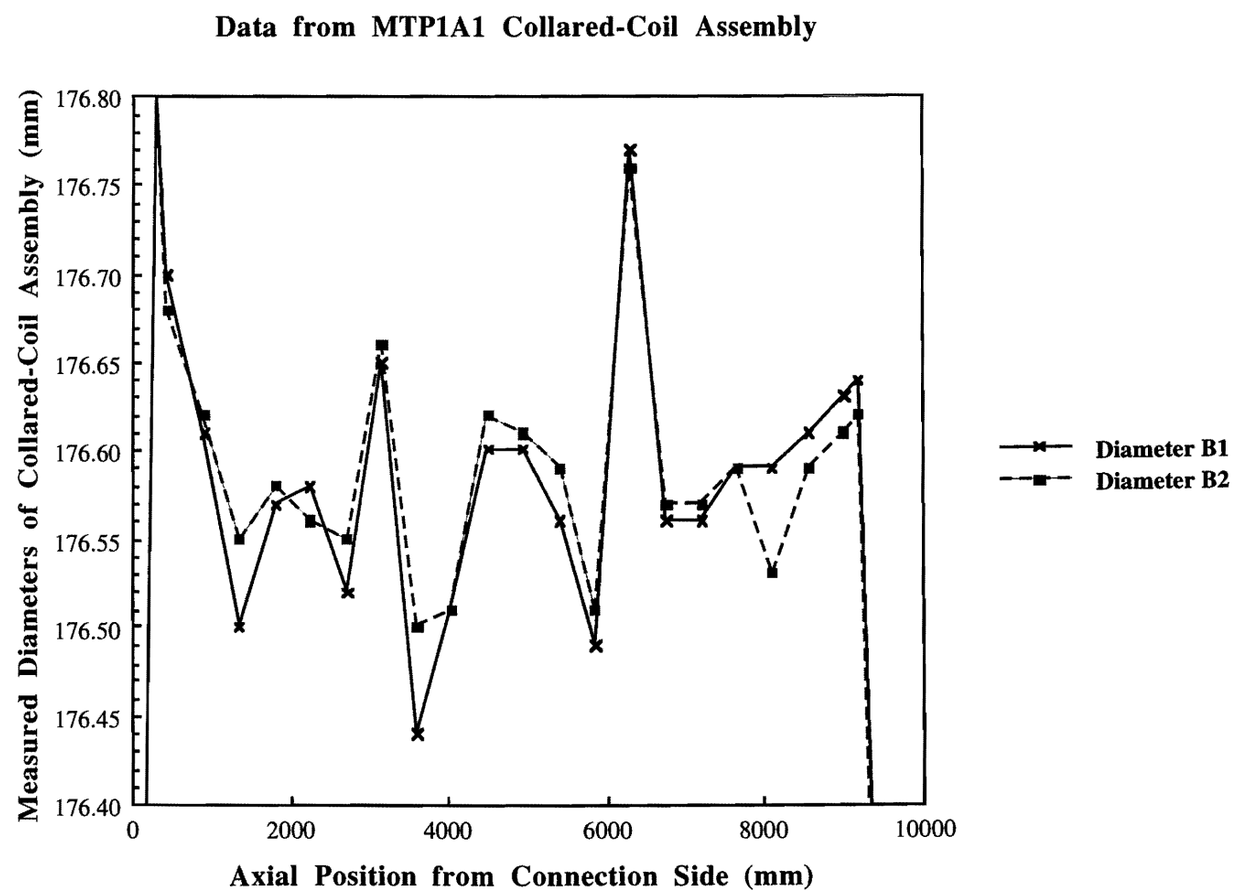

Figure 13. Summary plot of vertical dimensions (B_1B_1') and (B_2B_2') as a function of axial position measured on both sides of the collared-coil assembly of magnet MTP1A1. The nominal undeflected value is 176 mm.

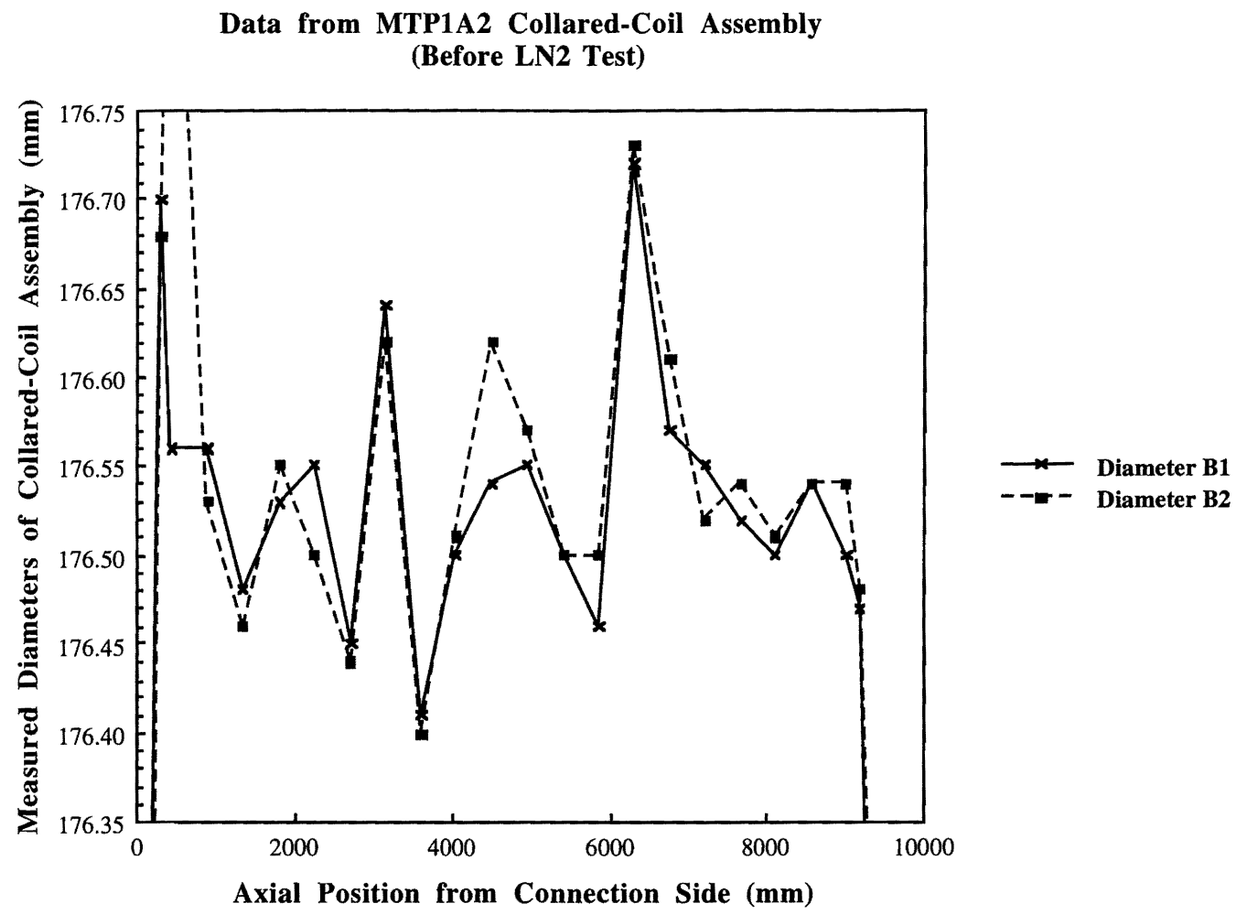

Figure 14(a). Summary plots of vertical dimensions (B_1B_1') and (B_2B_2') measured as a function of axial position on both sides of the collared-coil assembly of magnet MTP1A2 after collaring completion. The nominal undeflected value is 176 mm.

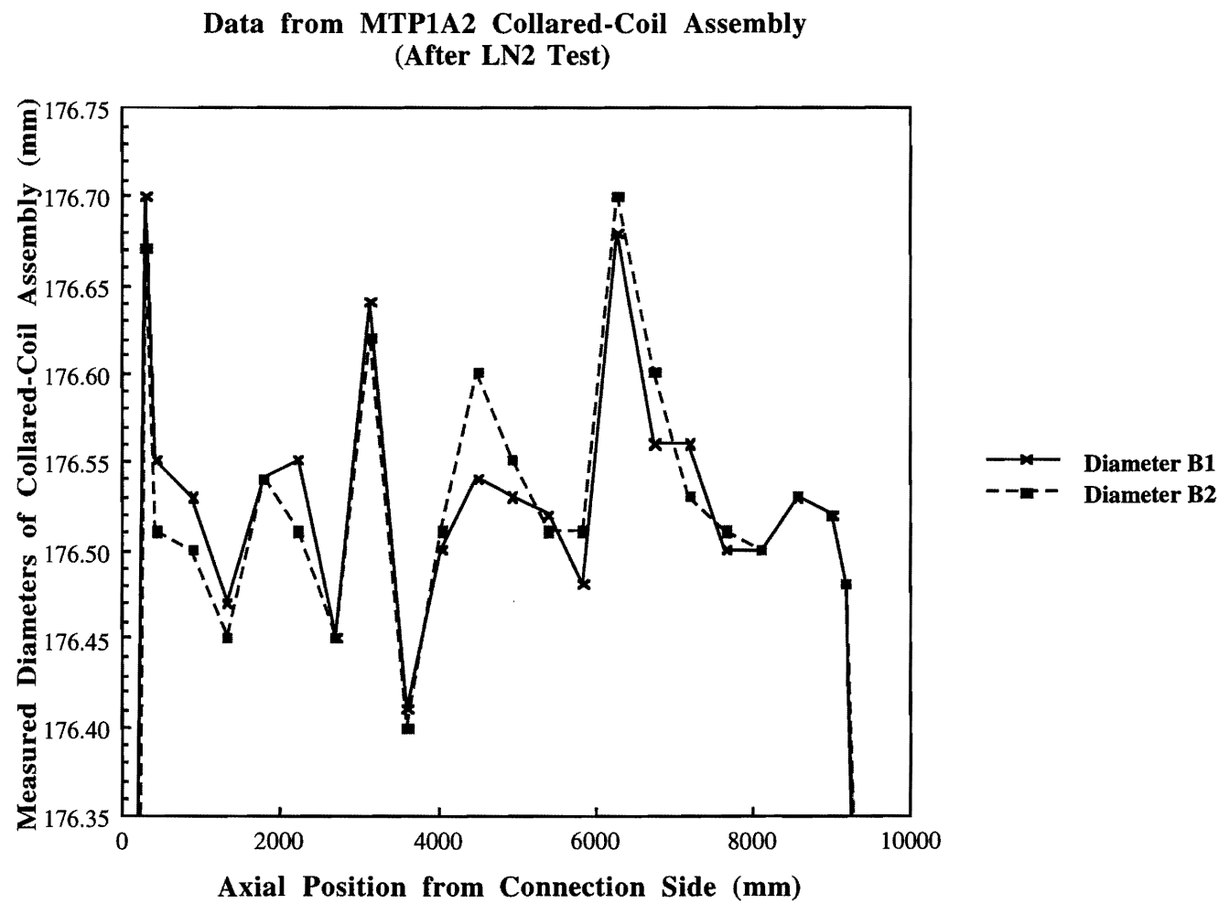

Figure 14(b). Summary plots of vertical dimensions (B_1B_1') and (B_2B_2') measured as a function of axial position on both sides of the collared-coil assembly of magnet MTP1A2 after a thermal cycle to 77 K. The nominal undeflected value is 176 mm.

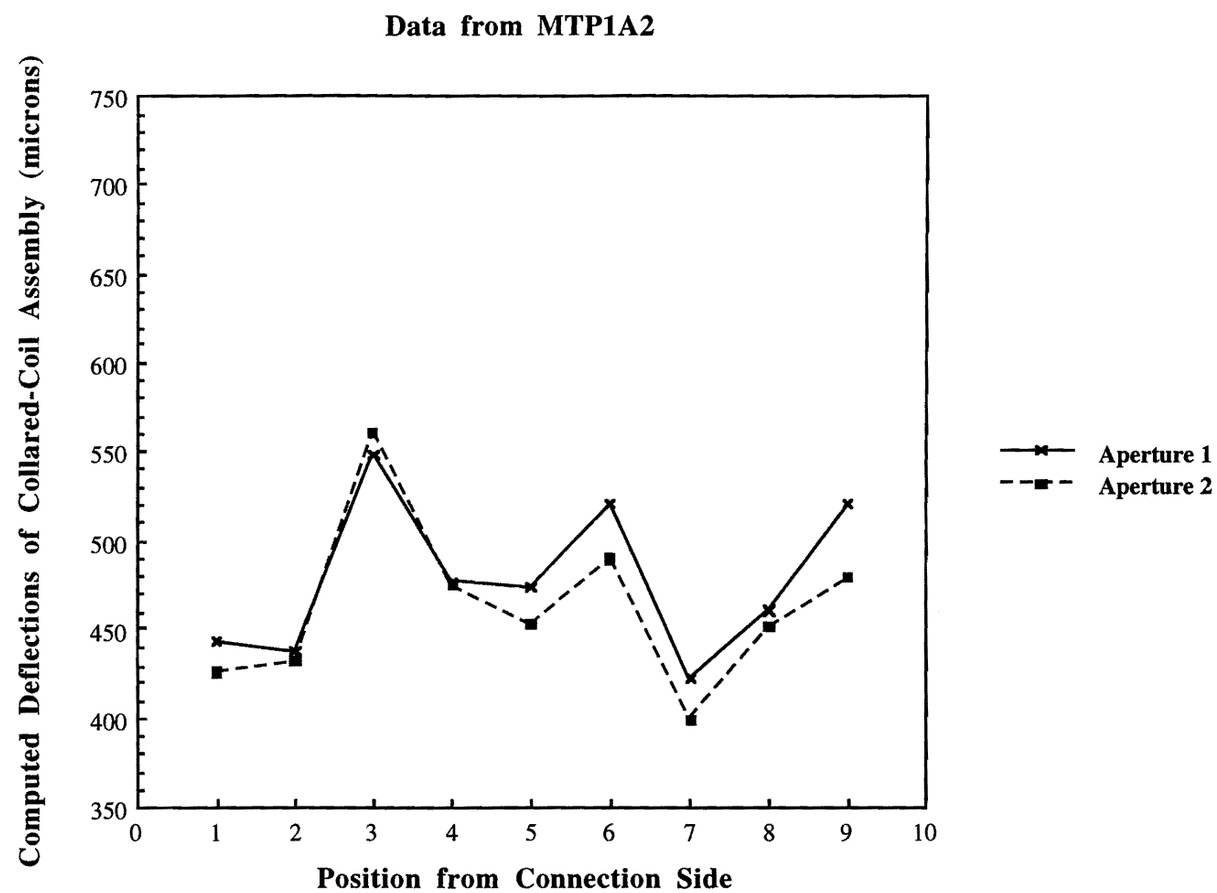

Figure 15. Summary plot of elastic elongations computed as a function of axial position along the two pole axes of the collared-coil assembly of magnet MTP1A2. A 50-μm correction is added to take into account the fact that the tie rods are not nominal.

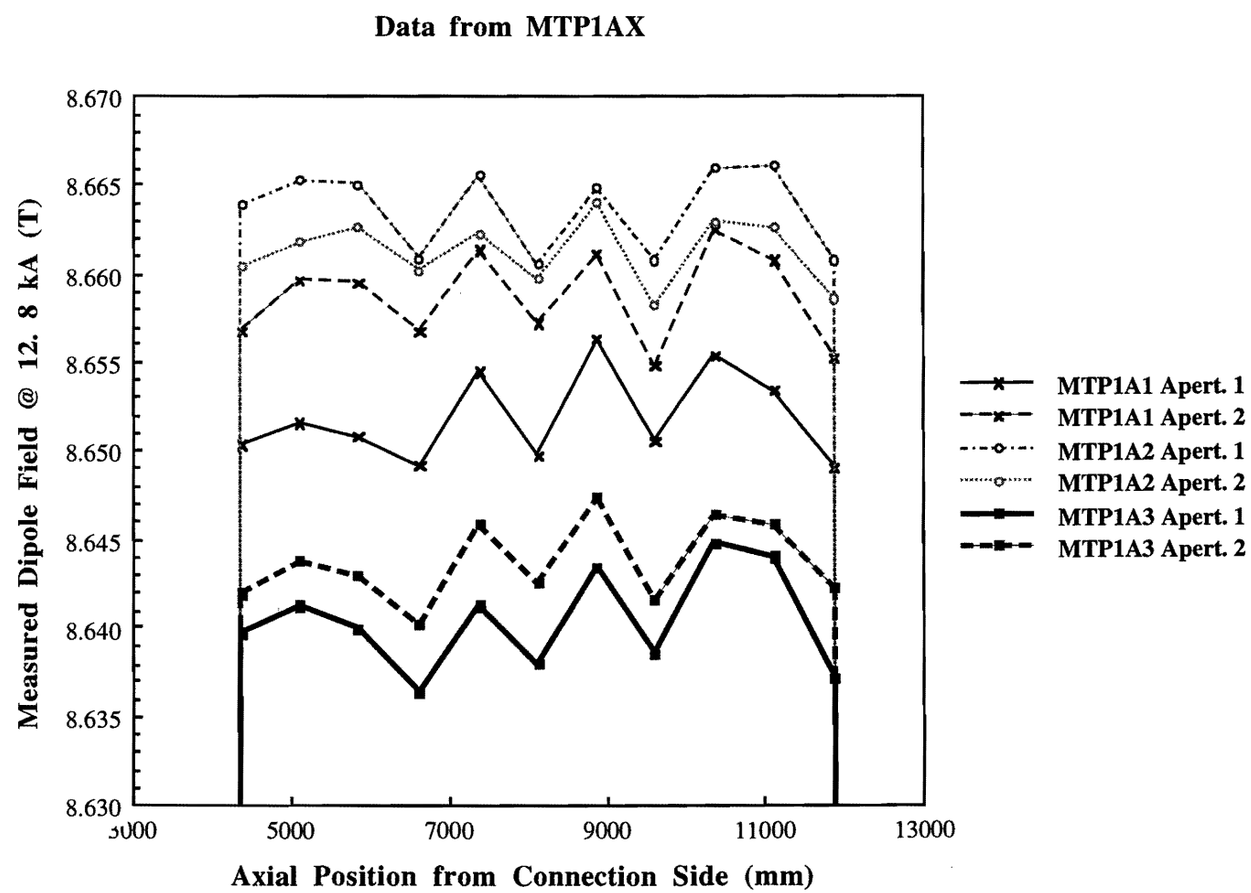

Figure 16. Summary plot of dipole field strength as a function of axial position measured at 1.9 K and 12.8 kA in the two apertures of the three 10-m-long, 50-mm-twin aperture LHC/Ansaldo dipole magnet prototypes.

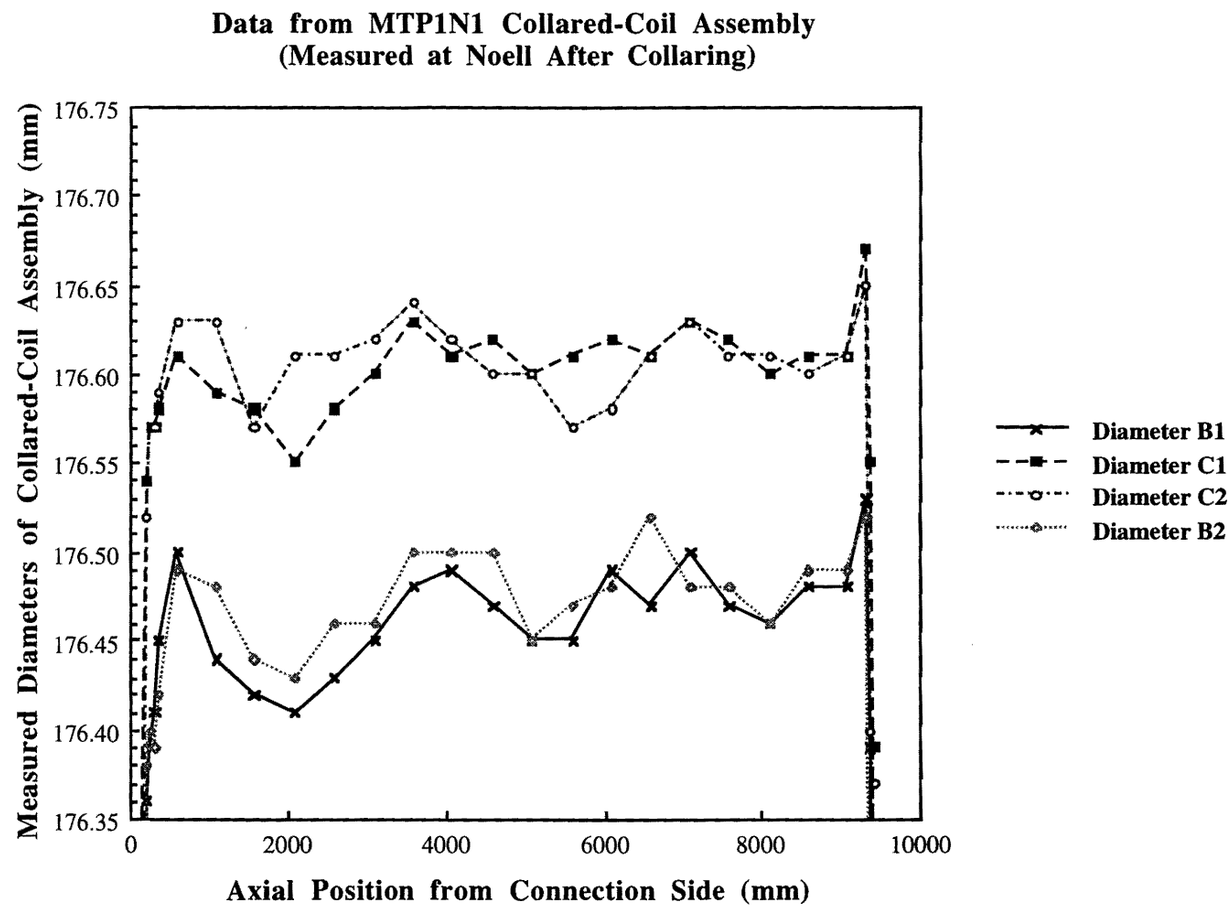

Figure 17(a). Summary plots of vertical dimensions (B_1B_1'), (B_2B_2'), (C_1C_1') and (C_2C_2') measured as a function of axial position on the collared-coil assembly of LHC/Noell dipole magnet prototype MTP1N1. The nominal undeflected values are 176 mm.

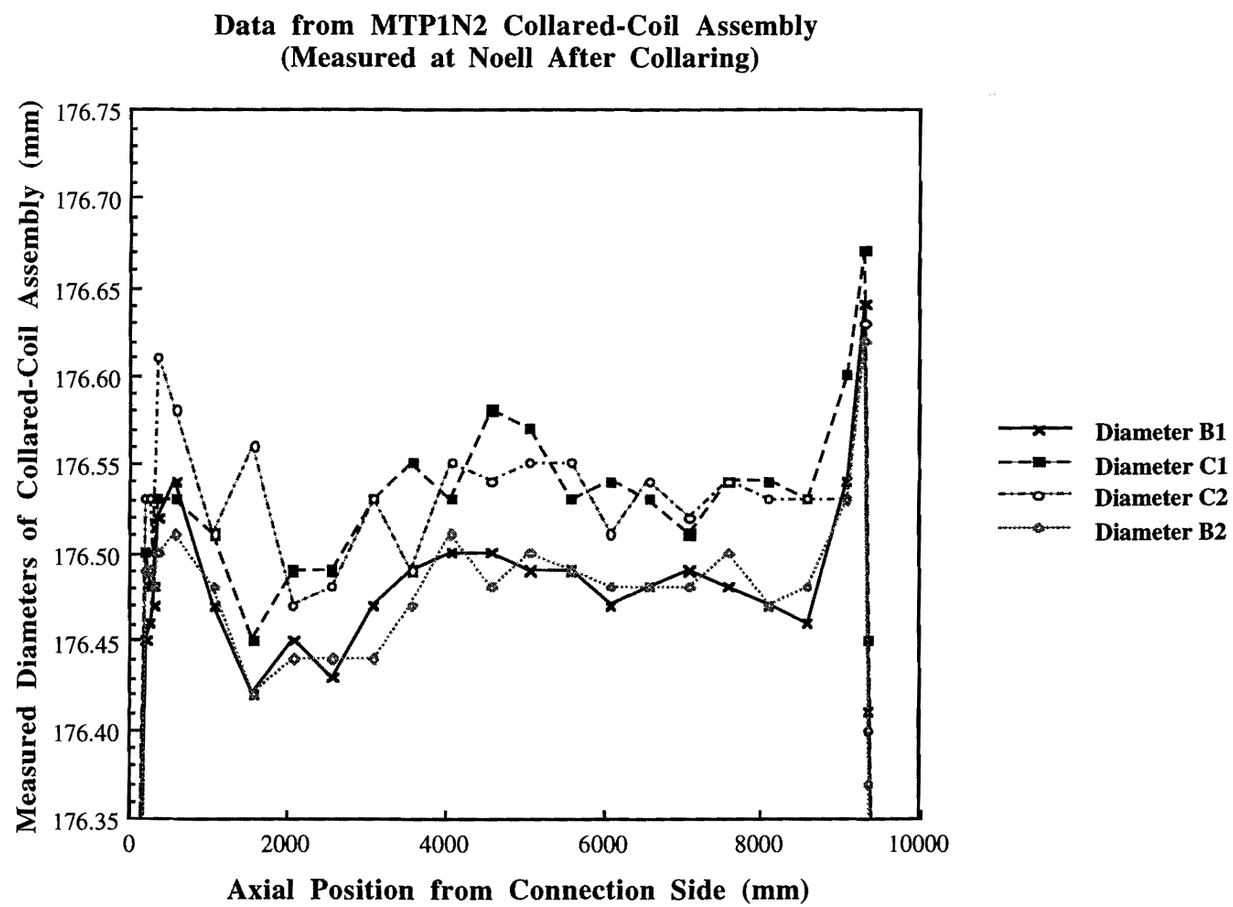

Figure 17(b). Summary plots of vertical dimensions (B_1B_1'), (B_2B_2'), (C_1C_1') and (C_2C_2') measured as a function of axial position on the collared-coil assembly of LHC/Noell dipole magnet prototype MTP1N2. The nominal undeflected values are 176 mm.

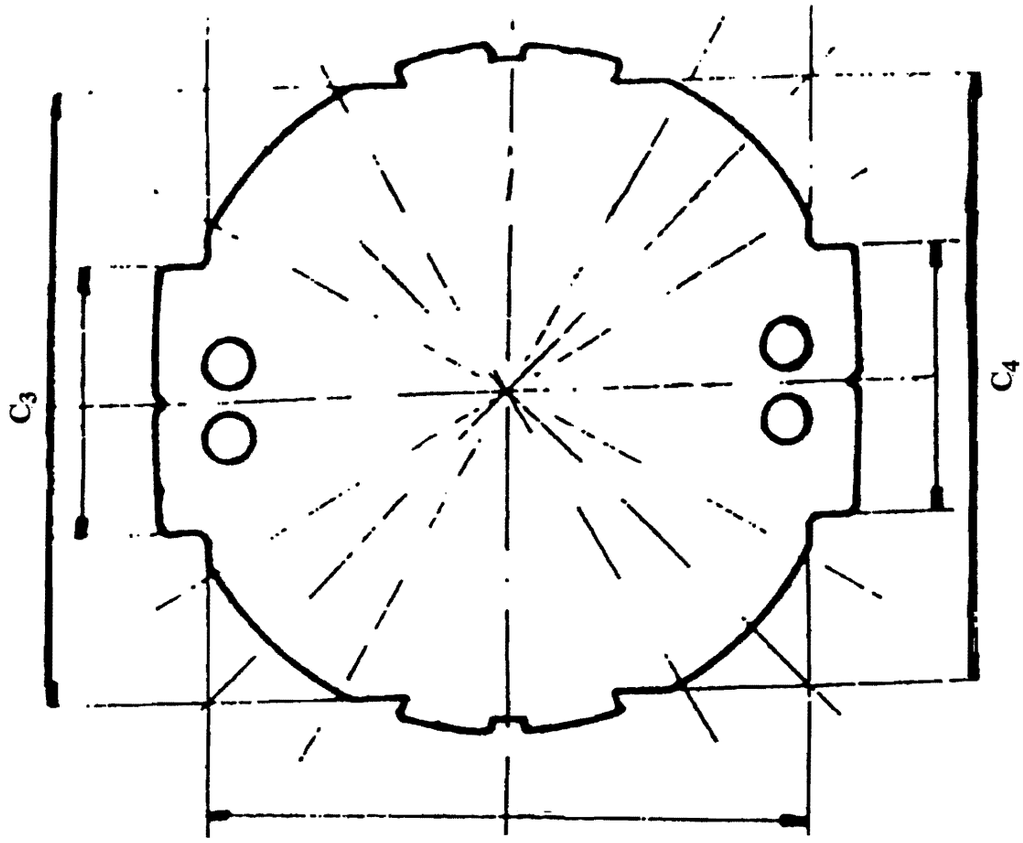

Figure 18. Definitions of the reference surfaces used to measure selected outer dimensions of the collared-coil assemblies of the Alsthom/Jeumont prototype.

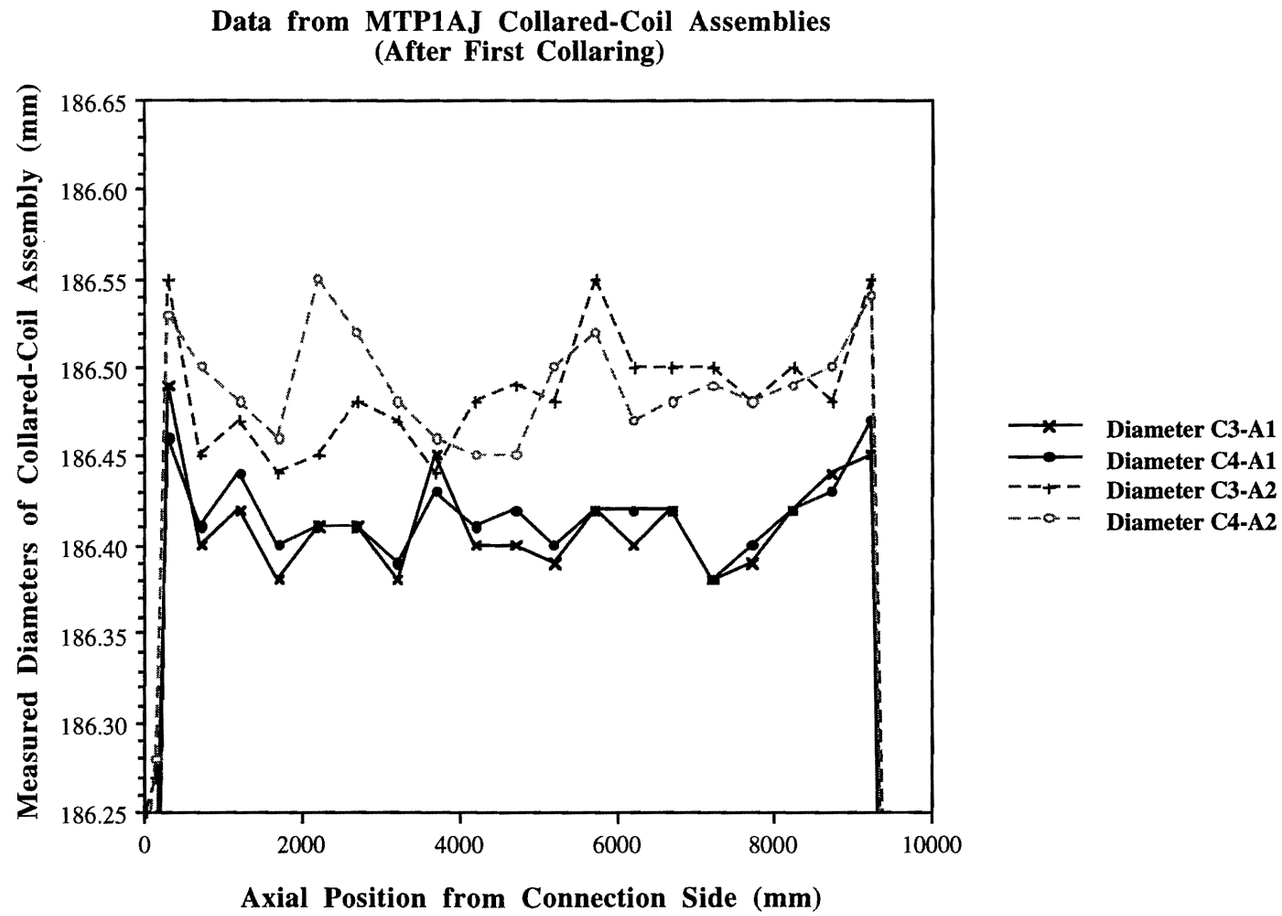

Figure 19(a). Summary plots of vertical dimensions (C_3) and (C_4) measured as a function of axial position after the first collaring of the Alsthom/Jeumont prototype MTP1AJ. The nominal undeflected values are 186 mm.

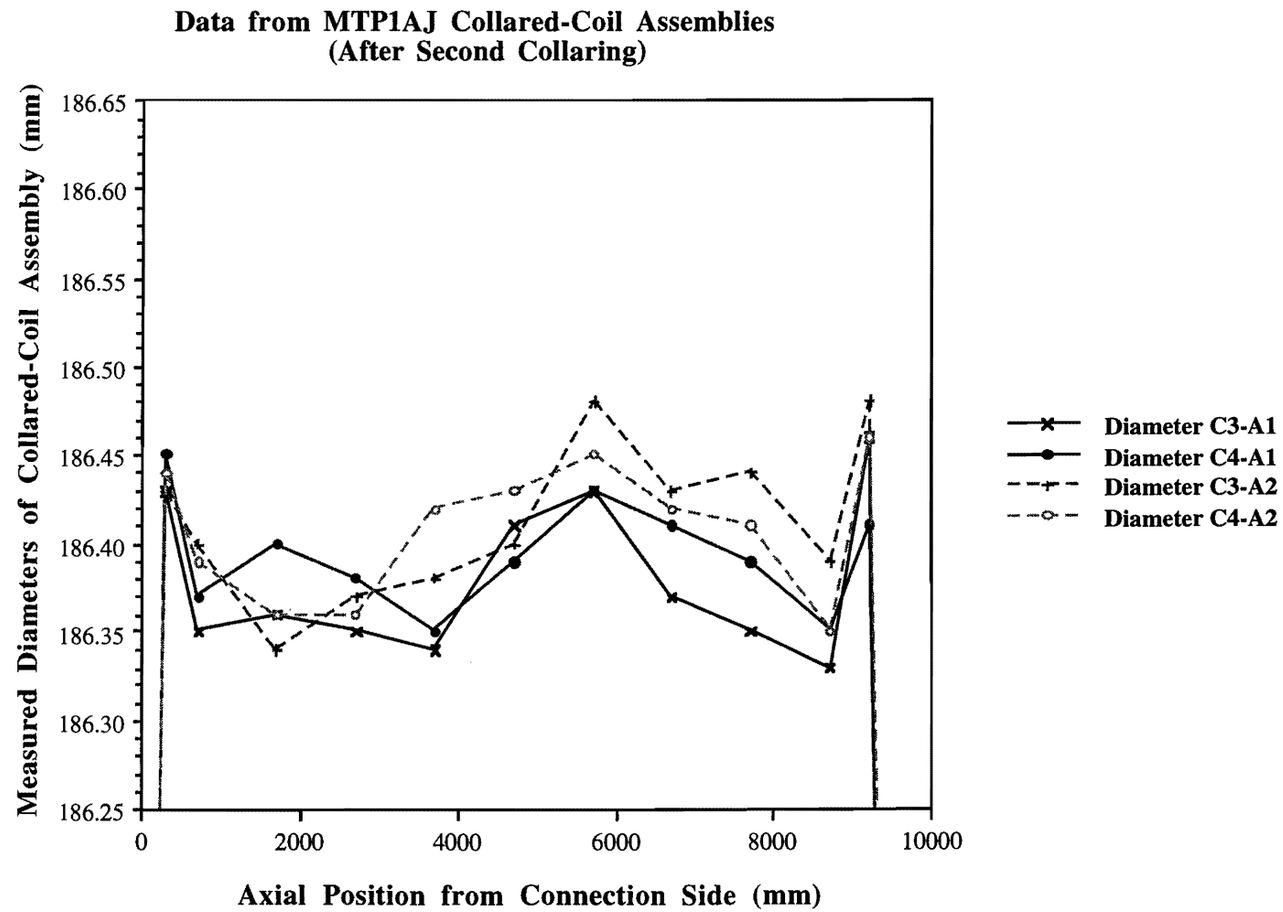

Figure 19(b). Summary plots of vertical dimensions (C_3) and (C_4) measured as a function of axial position after the second collaring of the Alsthom/Jeumont prototype MTP1AJ. The nominal undeflected values are 186 mm.

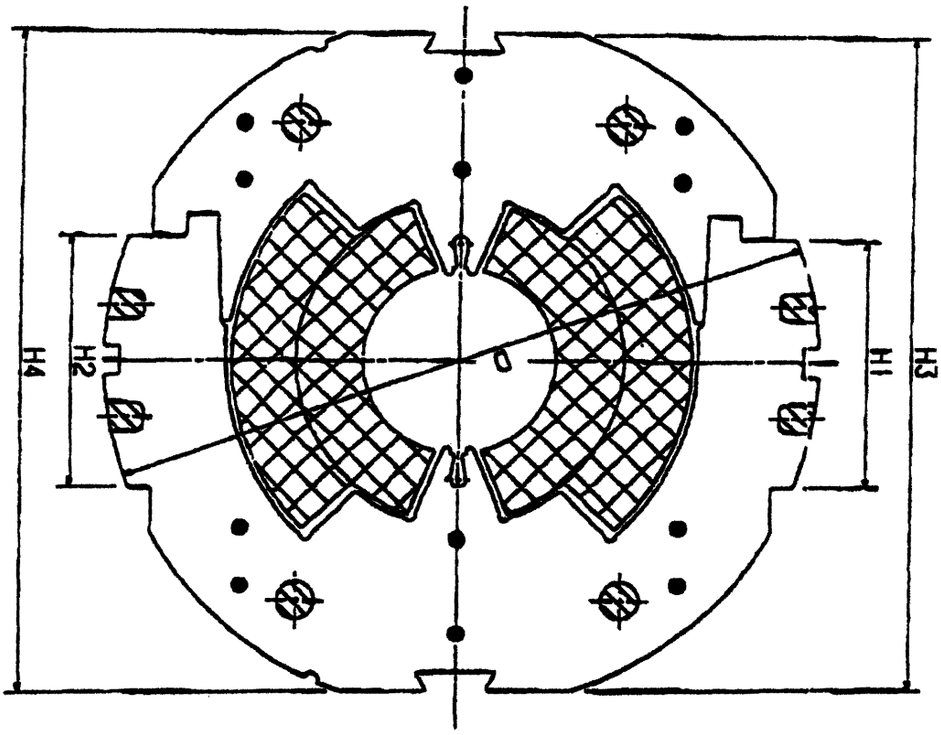

Figure 20. Definitions of the reference surfaces used to measure selected outer dimensions of the collared-coil assemblies of the Elin/Holec prototype.

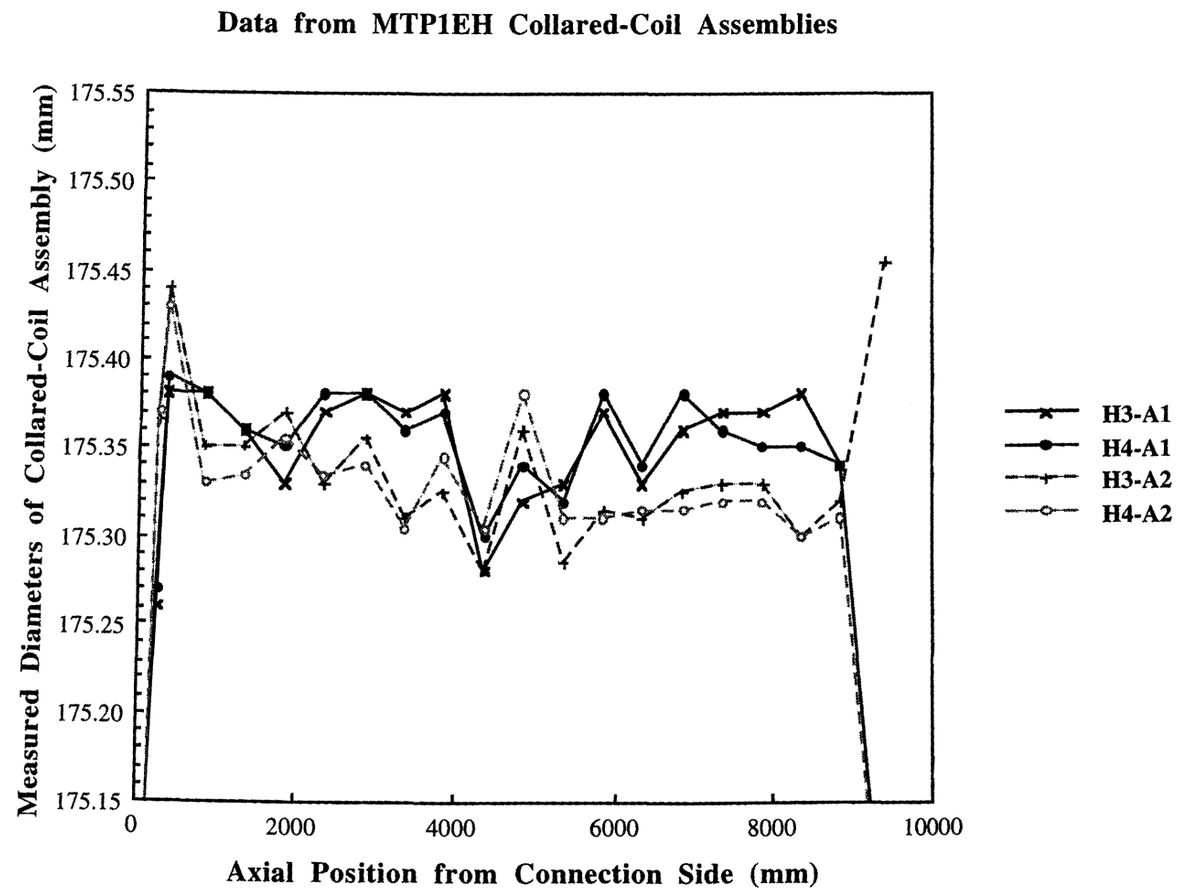

Figure 21. Summary plots of vertical dimensions (H_3) and (H_4) measured as a function of axial position on both sides of the collared-coil assemblies of the Elin/Holec prototype MTP1EH. The nominal undeflected values are 175 mm.